



universität
wien

Diplomarbeit

Titel der Arbeit

fMRI Artifact Correction
in EEG and EMG Data

Verfasser

Johann Glaser

Angestrebter akademischer Grad

Magister der Naturwissenschaften (Mag. rer. nat.)

Wien, 2012

Studienkennzahl: 298

Studienrichtung: Psychologie

Betreuer: Univ.-Prof. Dr. Claus Lamm und

Acknowledgment

I want to thank Prof. Claus Lamm and Florian Fischmeister, University Vienna, who supervised this diploma thesis. Florian advised me in the field of EEG and fMRI data processing. He gave countless good hints and stimulated creative ideas.

I also want to thank my parents who enabled me to freely decide what to study and always supported me to reach my goals. The University Vienna provided a good and fundamental education. The Institute of Computer Technology at the Vienna University of Technology was a very flexible employer so I could schedule courses and pursue my study without an interruption.

Special thanks go to the authors of EEGLAB with all its plugins, especially the FMRIB plugin. It provided the environment and the starting point for my work.

Kudos go to the worldwide open source community which develops numerous highly professional tools. The tools I used most during my diploma thesis are: \LaTeX , \BibTeX , \TikZ , GNU Make, GVim, lots of other powerful GNU tools (sed, grep, ...), Linux, the GNOME desktop and many others. Thanks go to their authors, maintainers, documenters, translators and all others who are involved to provide these programs.

Contents

1	Introduction	1
1.1	Multi-modal Imaging	2
1.1.1	Applications	3
1.1.2	Electromyography	4
1.2	Challenges	5
1.2.1	MR-Safety Aspects	5
1.2.2	Interference	6
1.3	Goal	6
2	Background	9
2.1	Methods	10
2.1.1	Magnetic Resonance Imaging (MRI)	11
2.1.2	Functional MRI (fMRI)	12
2.1.3	Electroencephalography (EEG)	13
2.1.4	Electromyography (EMG)	14
2.1.5	Combined EEG/EMG with fMRI	15
2.2	Artifacts	16
2.2.1	Electromagnetic Induction	17
2.2.2	Gradient Artifact Signal	18
2.2.3	Ballisto-Cardiographic Artifacts (BCG)	23
2.3	Artifact Correction Algorithms	24
2.3.1	Average Artifact Subtraction	25
2.3.2	fMRI Artifact Slice Template Removal (FASTR)	27
2.3.3	Realignment Parameter Informed Algorithm	28

2.3.4	Retrospective Synchronization Algorithm (Resync)	29
2.3.5	fMRI Artifact Reduction for Motion (FARM)	30
2.3.6	Frequency Domain Template Removal	31
2.4	Performance Indicators	33
2.4.1	Amplitude	33
2.4.2	RMS Ratios	34
2.4.3	Signal to Noise Ratio	35
2.4.4	Analysis in Frequency Domain	37
2.4.5	Qualitative	40
3	FACET — A New Correction Toolbox	43
3.1	Starting Point	44
3.1.1	EEGLAB, FMRIB Plugin	44
3.1.2	FARM Algorithm	44
3.2	Software Engineering	45
3.2.1	Reverse Engineering	46
3.2.2	Software Re-Engineering	47
3.2.3	Goals	47
3.2.4	Generalization	48
3.3	Object-Oriented Design	49
3.3.1	Object-Oriented Design Paradigm	49
3.3.2	Software Design	50
3.3.3	Algorithm Setup	52
3.3.4	Application Example	53
3.4	Data Analysis and Preparation	55
3.4.1	Analyze EEG Dataset and Setup	55
3.4.2	Get Trigger Latencies	57
3.4.3	Automatically Correct Missing Triggers	57
3.4.4	Manually Correct Missing Triggers	57
3.4.5	Convert Volume to Slice Triggers	57
3.4.6	Test Data and Setup	58
3.5	Pre-Filter	58
3.5.1	Slow Fluctuations	59
3.5.2	High-Pass Filter Implementations	59
3.5.3	Low-Pass Pre-Filter	60
3.6	Sub-Sample Alignment	61
3.6.1	Problem	61
3.6.2	Time-Shift with Sub-Sample Resolution	61
3.6.3	Interpolation Error	62
3.7	Volume Artifact	63

3.7.1	Problem	63
3.7.2	Correction	64
3.8	Averaging Matrix	65
3.8.1	Generalization	65
3.8.2	Implementation	67
3.9	Low-Pass Filter	68
3.10	Algorithm Sequence	69
3.10.1	Customization of Sequence	69
3.10.2	Example	70
3.11	Evaluation Framework	72
3.11.1	Software Design	72
3.11.2	Data Preparation	74
3.11.3	Performance Indicators	74
3.11.4	Usage Examples	76
4	Evaluation of EEGfMRI	79
4.1	Data	81
4.1.1	FMRIB Dataset	81
4.1.2	Pilot Dataset	82
4.2	Comparison Without Post-Processing	83
4.3	Pre-Processing and Template Generation Improvements	88
4.4	Incremental Activation of Post-Processing Steps	95
4.5	Comparison with Post-Processing	100
4.6	Pilot Dataset	105
4.6.1	Comparison Without Post-Processing	105
4.6.2	Pre-Processing and Template Generation Improvements	109
4.6.3	Incremental Activation of Post-Processing Steps	115
4.6.4	Comparison with Post-Processing	119
4.7	Discussion	124
5	Summary	127
5.1	Artifact Correction and Evaluation Toolbox	128
5.2	Future Work	129
	References	131
	Abstract	137

Zusammenfassung	139
Curriculum Vitae	141
Lebenslauf	143

1

Introduction

CONCURRENT acquisition of electroencephalogram (EEG) and functional magnetic resonance imaging (fMRI) is used since the late 1990ies. This allows to combine the strengths of both methods and to complete the fragmentary information provided by either one of them.

These advantages also come with drawbacks like mutual artifacts. The gradient artifact due to rapidly changing magnetic fields induces voltage in the EEG signal which exceed the original signal by several orders of magnitude. Subtle movements of the subject also cause artifact voltages, which well exceed the EEG signal. Although the drawbacks are tackled with broadly based methods, the results are not perfect. Recently, not only EEG but also electromyograph (EMG) signals are considered. While the acquisition equipment is similar, the signals are different and therefore pose new problems. Eventually, the remaining challenge is the motion of the subject.

This work compares existing methods to correct the EEG and EMG signals and provides improvements to tackle these problems. The main outcome is a universal toolbox, which provides methods for the removal of fMRI gradient artifacts from EEG and EMG signals.

1.1 Multi-modal Imaging

Both methods, EEG and fMRI, are used to investigate the working of the human brain. By the combination of these methods, the information on brain activity is provided in two modalities. With the assumption that the signals “relate to the same event” and are “produced by the same neural generators” (Rosenkranz & Lemieux, 2010, p. 2), the methods provide complementary information.

Originally, the combined acquisition of EEG and fMRI was used to localize the sources of interictal epileptic neural activity by correlating the EEG signal with the hemodynamic change observed by fMRI. From this initial clinical exertion, the method has now gained numerous applications in neuroscience (Rosenkranz & Lemieux, 2010).

While fMRI is a non-invasive imaging technique covering the whole brain with a high spatial resolution, it has a low temporal resolution. The relation between the vascular fMRI signal and the neural activity is expressed by the BOLD (blood oxygenation level dependent) response. This response function is primarily unknown due to the influence of ongoing brain states and activity (Ritter & Villringer, 2006; Minati, 2006).

On the other hand, EEG monitors brain states and activities and additionally has a high temporal resolution. Its disadvantage is the low spatial resolution and the fact, that the source can not be localized unambiguously (so called inverse problem) (Ritter & Villringer, 2006; Minati, 2006).

Combining both methods allows to integrate the high temporal resolution of EEG and the high spatial resolution of fMRI. By multi-modal data fusion the inverse problem is solved (Rosenkranz & Lemieux, 2010).

According to Ritter and Villringer (2006), three combinations of EEG and fMRI are employed:

Conjoint acquisition records EEG and fMRI in separate sessions.

Interleaved acquisition is performed with the subject located inside of the fMRI scanner, but EEG and fMRI acquisition are performed at different times.

Concurrent/continuous acquisition means, that fMRI and EEG are recorded at the same time.

While conjoint acquisition does not pose any mutual influence of EEG and fMRI, it is not assured that the observed activities are related. The same

disadvantage holds for interleaved acquisition, but due to the identical environment, the differences of cognitive processes are lower. However, the EEG and fMRI recording equipment might influence each other. For concurrent acquisition this problem is evidently given and is covered extensively in this work. Concurrent acquisition is the only variant which allows true multi-modal observation of brain processes (Ritter & Villringer, 2006; Menon & Crottaz-Herbette, 2005).

1.1.1 Applications of Multi-modal Imaging

For the investigation of spontaneous brain activity, the concurrent acquisition of EEG and fMRI is mandatory. In cognitive and systems neuroscience the coherence in this neural activity and the hemodynamic response is observed to study the idle state (also called the cognitive default mode) of the brain (Rosenkranz & Lemieux, 2010; Ritter & Villringer, 2006). For example the driver and the spatial distribution of the classical human alpha-rhythm were investigated. Studies reported by Ritter and Villringer (2006) showed reduced metabolism which is an indicator of inhibited cortical areas. The origin is highly likely the thalamus, but the results are still ambiguous due to interfering rhythms from global state changes.

These global state changes, which even occur during rest, are reflected in BOLD signal fluctuations. To account for the additional variance in the BOLD signal, the state changes are observed with EEG and included as factors in the statistical data analysis (Ritter & Villringer, 2006).

This approach is further extended to investigate evoked activity (Ritter & Villringer, 2006). The EEG signal recorded during repeated presentation of stimuli is post-processed to acquire event related potentials (ERP). Features of the ERP are correlated to BOLD activity to “identify corresponding brain regions [...] at a timescale close to that of the EEG” (Rosenkranz & Lemieux, 2010, p. 3)

Ritter and Villringer (2006) report works which correlate the time course of EEG signal power in spectral bands electrode-wise with the BOLD signal measured with fMRI voxel by voxel. Tightly synchronized inter-neurons showing gamma oscillations in the EEG signal are associated with an inhibition as observed in the BOLD response, which at a macroscopic level means that changes in spectral power are associated with BOLD changes (Rosenkranz & Lemieux, 2010).

Combined EEG and fMRI was also used to study the “relation between cognition/behavior and neuronal synchrony” (Ritter & Villringer, 2006, p. 833). Numerous studies found relations between EEG frequency contents and cognitive functions. The authors generally state, that “it would be of interest to create spatiotemporally resolved whole-brain maps of coherent neuronal non-event-related activity for different behavior and cognitive states” (Ritter & Villringer, 2006, p. 834).

Besides the utilization of combined EEG and fMRI in research, the method is also applied in clinical settings. For the treatment of epilepsy, the epileptic foci are localized prior to the cortical resection (Ritter & Villringer, 2006; Rosenkranz & Lemieux, 2010). On the other hand, association of interictal epileptic electric activity with the hemodynamic response is not yet fully understood (Ritter & Villringer, 2006) and intensively investigated (Rosenkranz & Lemieux, 2010). Electrical source imaging (ESI) is used to map the scalp EEG data to the three-dimensional locations in the brain to find the focus of interictal epileptiform discharges and distinguish them from areas of propagation (Michel et al., 2004; Rosenkranz & Lemieux, 2010).

Ritter and Villringer (2006) summarize future utilization of the combined acquisition of EEG and fMRI to better understand the high variability of brain responses and the dynamic coupling as well as to investigate the “age-related changes in brain physiology” (Ritter & Villringer, 2006, p.834).

1.1.2 Other Modalities: Electromyography (EMG)

In the previous sections possibilities for the combined acquisition of the two modalities fMRI and EEG were outlined. Adding a third modality, namely electromyography (EMG), adds information on muscle activity like movements and strain (Fridlund & Cacioppo, 1986; Ritter & Villringer, 2006).

The recording equipment for EMG is very similar to that already in place for EEG and can often be used for both purposes. The concurrent recording of EEG and EMG during fMRI acquisition was shown in 1.5 T and 3 T MR scanners (Ritter & Villringer, 2006). Exemplary applications are the observation of hand muscle activity (blocked hand) which showed no artifacts in the MR image. Further more, maps of the sensorimotor system were assembled using concurrent fMRI, EEG and EMG (Ritter & Villringer, 2006). For example, van der Meer, Tijssen, Bour, van Rootselaar, and Nederveen (2010) observed the EMG activity on the neck, hand, and arm muscles during fMRI acquisition.

1.2 Challenges

Although the combined acquisition of EEG and fMRI is in use for more than ten years, it still poses challenges. The main aspect is the safety of the subject inside the MR scanner. The EEG leads act as antennas which pick up the RF excitation signal. This can lead to heating of the electrodes up to nearly 50°C, although the mostly employed fMRI sequence EPI only leads to an increase of less than 1°C.

On the other hand, the mutual interference of both methods impair the acquired data. The influence of the EEG equipment to the MR image quality is negligible when appropriate materials are chosen. However, the EEG signal is considerably deteriorated by electromagnetic induction due to minimal subject movements and especially due to the rapidly changing gradient magnetic fields.

1.2.1 MR-Safety Aspects

Besides the safety precautions for standalone-MR (Mühlenweg, Schaefer, & Trattnig, 2007) there are additional issues of the combination with EEG. The EEG electrode wires build resonant antennas which pick up the RF excitation signal. This leads to heating and possibly burning of the subject's tissue (Meriläinen, 2002). Measurements of the temperature increase of EEG electrodes in a 3 T scanner performed on a phantom and a sheep head found a maximum temperature increase of 12.3°C for the FSE sequence. This was extrapolated to a steady state of 13.5°C. For skin with a base temperature of 36°C this results in a temperature of 49.5°C which causes burning and pain.

The temperature increase strongly depends on the specific absorption rate (SAR) of the MR sequence (FSE: 2.8 W/kg, EPI: 0.077 W/kg). The maximum temperature increase measured with the EPI sequence, generally utilized for fMRI, was only 0.85°C (Meriläinen, 2002). Unfortunately the study did no systematic search for the spatial spot of the maximum temperature increase, so the measured value is a lower bound. Yet it suggests that at least with a 3 T scanner no extreme temperature rise must be considered (Nöth, Laufs, Stoermer, & Deichmann, 2011).

1.2.2 Mutual Interference between EEG and fMRI

The combination of EEG and fMRI introduces mutual interference. These artifacts impair the acquired signal of both methods. The EEG equipment attached to the subject affect the magnetic field due to its different magnetic susceptibility. This deteriorates the magnetic field homogeneity and thus the image quality (Rosenkranz & Lemieux, 2010). Thus, appropriate selection of materials to avoid ferromagnetic metals and to choose electrode gels and insulators with low magnetic susceptibility is required. Furthermore, the EEG amplifier must withstand the high magnetic field and the fast gradient fields (Ritter & Villringer, 2006).

While the interference of EEG equipment to fMRI acquisition is negligible (at least up to 3 T), the artifacts introduced into the EEG signal are considerable. The underlying physical effect is *electromagnetic induction*; a change of the magnetic field induces voltages in the EEG leads (Ritter & Villringer, 2006).

Small movements of the subject change the position of the EEG leads and thus the portion of the static main B_0 magnetic field they enclose. Due to the high magnetic field, these artifacts are present as soon as the subject is positioned inside the scanner bore, even without MR acquisition (Ritter & Villringer, 2006). These small movements caused e.g. by the pulsating blood flow through the scalp cause the ballistocardiographic artifact (BCG) of more than $200\ \mu\text{V}$ (Allen, Polizzi, Krakow, Fish, & Lemieux, 1998).

The acquisition of MR images requires fast establishment of gradient magnetic fields for spatial resolution. These changing magnetic fields cause much higher induction voltages in the EEG leads. Figure 1.1 shows a comparison of a pure EEG signal with these gradient artifacts.

To reduce the induced voltages, the electrode wires need to be laid out with a minimum area of loops and special MR sequences with slowly changing gradient fields are applied (Ritter & Villringer, 2006).

1.3 Goal of this Work

Despite the effort to reduce the gradient artifacts induced in the electrode leads, they still exceed the EEG signal by three to five orders of magnitude. These are corrected with mathematical algorithms which basically utilize their highly regular pattern. Multiple consecutive artifacts are averaged and subtracted from the measured signal (Allen, Josephs, & Turner, 2000).

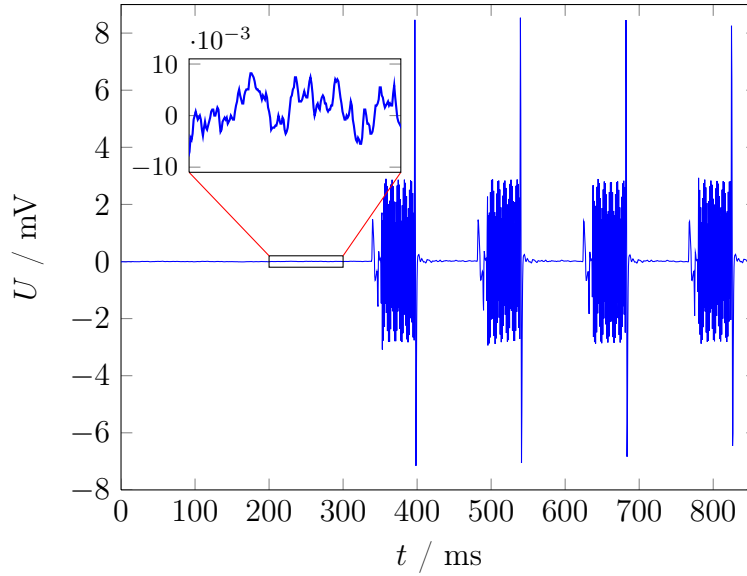


Figure 1.1: Exemplary section of the FMRI dataset (see Sec. 4.1.1) around the onset of fMRI acquisition. The amplitude of the pure EEG signal before the fMRI acquisition is below $\pm 10 \mu\text{V}$ (see inset). The acquisition starts at 338 ms and causes gradient artifacts with an amplitude of $\approx \pm 8 \text{ mV}$.

These algorithms work fine as long as the subject does not move. However, the acquisition of muscle activity with EMG is accompanied with (little) movements of the electrodes. These change the artifact signal pattern and thus pose problems to the existing algorithms.

The goal of this work is to evaluate existing correction algorithms and introduce improvements to cope with the challenges caused by subject movements.

The final outcome is to answer, whether it is possible to overcome current limitations of EEG/EMG measurements during fMRI acquisition. Additionally a proposal in the sense of “best practice” is given, which correction algorithm to select and how to adjust its parameters to obtain optimum results.

2

Background

THIS thesis is based on prior scientific work, as outlined in this chapter. Magnetic resonance imaging (MRI) is the underlying technique for non-invasively acquiring structural information of the human brain. The so called BOLD effect allows to exert this technique for functional inspection of brain activity (fMRI). Another functional method is electroencephalography (EEG), which measures electrical signals at the scalp surface and correlates it to stimuli and cognitive processes. EEG is often combined with electromyography (EMG) to measure muscle activity, e.g. of facial motion. Finally, the combination of fMRI and EEG/EMG allows to complement the strengths of both methods and to cover the individual weaknesses.

However, mutual interferences of fMRI and EEG/EMG poses challenges to the combined application. While the fMRI image quality is nearly unaffected by the EEG recording, the EEG signals are severely impaired. Electromagnetic induction, caused by the rapidly changing MRI gradient fields, results in interference several magnitudes larger than the EEG signal itself. The same holds for artifacts caused by minor movements resulting from the cardiac pulse.

Multiple mathematical algorithms exist to remove the artifact. A very simple implementation zeroes the EEG signal during fMRI acquisition, but this is only possible for MR sequences with short acquisition and long breaks. Most other algorithms utilize the high regularity of the gradient artifact and average multiple periods, which are then subtracted. The differences between the algorithms are mainly in the pre-processing before and the post-processing after the average template subtraction. Another differentiation can be found in the method of template generation. A few algorithms exist which perform the correction in frequency domain.

All these correction algorithms obtain imperfect results. To assess the quality of artifact removal, multiple performance indicators are employed. The simplest criteria is the signal amplitude, but also the root-mean-square (RMS) and the signal-to-noise ratio (SNR) are common. In frequency domain, the periodic gradient artifact signal shows a fundamental and harmonics, which are also used to assess the attenuation. Finally, qualitative measures are employed, which on one hand are less reproducible, but are highly representative for the further usage of the EEG signal.

2.1 Methods

Scientists and physicians were interested in the structures of the human brain for a long time (Minati, 2006). Advances in technology allow to perform these examinations in-vivo with non-invasive methods. The most frequently utilized neuro-imaging techniques are computed tomography (CT) and magnetic resonance imaging (MRI). Both methods reveal morphological information of the brain (Minati, 2006).

Besides these morphological insight, techniques were developed which allow a functional analysis of the brain. MRI can easily be extended to functional MRI (fMRI). A totally different physical approach is utilized by positron emission tomography (PET). While these methods are inherent imaging techniques, the electrical brain activity is directly recorded only with electroencephalography (EEG). A related technology utilizes the magnetic field produced by the electric activity, namely magnetoencephalography (MEG) (Minati, 2006).

EEG source localization techniques try to locate the generators of measured features (Pascual-Marqui, Michel, & Lehmann, 1994; Pascual-Marqui,

1999; Baillet et al., 2001; Michel et al., 2004) which extend EEG to a (low-resolution) functional imaging technique.

The electrical activity of muscles is often recorded as an auxiliary measure to EEG (electromyograph, EMG). The recording of eye movement aids in EEG-post-processing to remove related artifacts (Fridlund & Cacioppo, 1986; Blumenthal et al., 2005). Besides this usage, EMG is also widely applied as standalone method.

Although the mentioned functional imaging methods EEG and fMRI provide useful information on their own, the combination allows deeper insights and provides higher quality data. These multi-modal acquisition techniques complement each other to remedy each others shortcomings (Menon & Crottaz-Herbette, 2005; Ritter & Villringer, 2006; Rosenkranz & Lemieux, 2010). Alas, this comes at the price of mutual artifacts as will be discussed in Sec. 2.2.

2.1.1 Magnetic Resonance Imaging (MRI)

Magnetic resonance imaging is a non-invasive imaging technique used in medical science to visualize tissue inside the body. It allows a comparable high spatial resolution (Minati, 2006).

The underlying physical principle utilizes the magnetic spin of the protons in atomic nuclei. These are aligned along a strong base magnetic field B_0 . An RF field is used to deflect their rotation which leads to a precession around the main axis. After this excitation, the relaxation occurs with a material dependent time constant. This results in a contrast, i.e. the image intensity (Weishaupt, Köchli, & Marincek, 2003; Huettel, Song, & McCarthy, 2009).

The excitation has to be performed with a frequency which matches the nucleus resonance frequency (Larmor frequency). This linearly depends on the magnetic flux density B . This fact is utilized for spatial coding to limit excitation to certain regions of the body. During readout it is used to identify the origin of the received signals by their frequency. The static base magnetic field B_0 is homogeneous throughout the MR scanner. To setup a spatially varying magnetic field, additional gradient fields are activated (Weishaupt et al., 2003; Huettel et al., 2009).

An MRI acquisition consists of one or more RF excitations, gradient activations and readouts. The precise temporal composition is called “sequence”. Many different variations are employed which allow to emphasize different

materials and physical effects. Since all sequences have their individual strengths and weaknesses, the selection depends on the desired exploration.

With this methodology, the structures of the human body, especially of the brain, can be visualized with high spatial resolution. Advanced methods and according sequences exist to visualize the flow of blood (angiography), to visualize diffusion of liquid or to visualize the oxygenation level of blood (Minati, 2006). With the latter mechanism, a functional imaging approach is realized.

2.1.2 Functional MRI (fMRI)

With functional methods, the activity of the brain is studied. These are used to find the places of ongoing neural activity. Strictly speaking, there is no inactive state in brain, therefore an increase and decrease of activity is recorded. Functional MRI (fMRI) is able to identify the regions with high spatial but low temporal resolution (Minati, 2006; Huettel et al., 2009).

The indicator of brain activity is the neural blood supply. Increased brain activity results in raised metabolism and oxygen consumption which requires higher blood supply. The regulation results in an excess supply which leads to less desoxygenated venous blood, i.e., the blood after the consumers is more oxygenated (Huettel et al., 2009; Ritter & Villringer, 2006).

The utilized physical effect is the dependence of the susceptibility of blood on its oxygenation level. Oxygenated blood is diamagnetic while desoxygenated is paramagnetic, which is a direct result of the molecular setup in the hemoglobin. This varying susceptibility results in MR intensity contrasts (blood oxygenation level dependence, BOLD effect, Ogawa, Lee, Kay, & Tank, 1990; Ogawa et al., 1993) which are used as an indicator of brain activity (Ritter & Villringer, 2006).

The time course of the blood oxygenation in venous blood is delayed 3–8 seconds according to the hemodynamic response (Moser et al., 2010). This depends on many factors (including the region of the brain) and can only be estimated mathematically (Huettel et al., 2009). An additional problem is that no inference on neural activity is possible because the blood supply is “not regulated on the scale of individual neurons” (Ritter & Villringer, 2006, p. 825).

The fMRI analysis results in a sequence of voxel data of the whole brain. An increase (decrease) of the intensity value is interpreted as increase (decrease) in blood oxygenation and therefore as spots of neural activity (inhibition)

(Huettel et al., 2009). This shows low-frequency noise resulting from permanent and very slow large-scale fluctuations of blood supply, which origin is poorly understood. On the other hand, event-related changes in blood supply are investigated in more detail and build the basis for most fMRI studies (Menon & Crottaz-Herbette, 2005). Although the hemodynamic response is relatively slow, the whole brain volume must be scanned with a period of a few seconds. This requires very fast MR sequences like echo planar imaging (EPI) (Huettel et al., 2009).

2.1.3 Electroencephalography (EEG)

With fMRI the brain activity is measured according to a secondary effect (blood oxygenation). Electroencephalography (EEG) directly measures the activity as electrical signals at the scalp surface. This non-invasive technique uses multiple electrodes placed at standard positions (10-20-system, see Bauer, 1984) connected to sensitive amplifiers. The amplitude is in the range of only a few tens of micro-volts (μV) (Bear, Connors, & Paradiso, 2007; Ritter & Villringer, 2006) with a maximum of $75 \mu\text{V}$ (Menon & Crottaz-Herbette, 2005).

The “voltages [are] generated by the currents that flow during synaptic excitation of the dendrites of many pyramidal neurons in the cerebral cortex” (Bear et al., 2007, p. 587). “These currents induce voltage changes (in the μV range) that are smaller than action potentials but that last longer and extend over a larger area of neural tissue.” (Menon & Crottaz-Herbette, 2005, p. 293). Only neural activity close to the scalp surface, i.e. the neo-cortex, can be recorded. The electrical activity of synchronized neurons sums up to a measurable signal (Bear et al., 2007; Ritter & Villringer, 2006; Menon & Crottaz-Herbette, 2005). This synchronization results in rhythmic activity easily visible at EEG recordings. The frequency of these rhythms is divided into frequency bands (Bauer, 1984).

The electrical signal of the neurons has to pass the meninges and the skull which reduces its amplitude by a factor of 2 to more than 60 and “spatially smears the signals” (Ritter & Villringer, 2006, p. 824). Due to the low-pass property of cell membranes, only frequencies up to approximately 50 Hz are conducted to the electrodes (Ritter & Villringer, 2006; Rosenkranz & Lemieux, 2010).

Due to the “spatial smearing” cited above, the EEG signal measured at the electrodes is the sum of multiple sources, weighted by geometric and conductive properties of the head. This means that the sources are “projected”

to the skull surface. To identify the sources, the so called inverse problem has to be solved, because for every actually measured signal pattern, “an infinite number of possible locations and magnitudes” (Ritter & Villringer, 2006, p. 825) of sources exist (Ritter & Villringer, 2006). Numerous algorithms and approaches exist which try to identify the sources of the measured electrical activity (see e.g. Pascual-Marqui et al., 1994; Pascual-Marqui, 1999; Baillet et al., 2001; Michel et al., 2004).

Besides recording the spontaneous EEG signal, many scientific experiments correlate the EEG signal as emerged after a stimulus. These recordings are called event related potentials (ERP). The signal is immersed by the random fluctuations of brain activity, so the signal-to-noise ratio (SNR) is below 1.0 (Menon & Crottaz-Herbette, 2005). To get a reasonable signal, many (hundred to thousand according to Bauer, 1984; 30–100 according to Menon & Crottaz-Herbette, 2005) recordings are averaged time locked to the stimulus onset. The “positive- [and] negative-going fluctuation[s] that can be visually identified in the ERP waveform” (Menon & Crottaz-Herbette, 2005, p. 294) are given names depending on their ordinal position or latency after stimulus onset (e.g., “P1”, “N400”). These components are used for further investigations.

A special class of ERPs are slow cortical potentials (SCP) which last up to 10–20 s after the event. The frequencies are far below 1 Hz and thus forbid the usage of high-pass filters in EEG recording and processing (so called DC-EEG) (Moser et al., 2010).

2.1.4 Electromyography (EMG)

Electromyography (EMG) is used to measure the strain and movement of muscles. “The EMG signal is a quasi-random train of motor unit action potentials discharged by the contraction of striate muscle tissue.” The signal ranges “from fractions of a μV to several hundred μV ” (Fridlund & Cacioppo, 1986, p. 568) in a frequency range from several Hz to 2 kHz (ibid.).

The signal is picked up directly in the muscle with fine-wire or needle electrodes. It can also be measured non-invasively with surface electrodes attached to the skin above the muscles. A “paired electrode placement parallel to the course of the muscle fiber usually maximizes selectivity” (Fridlund & Cacioppo, 1986, p. 570).

EMG is often combined with EEG to monitor eye-blinks and eye movements (electrooculogram, EOG) (e.g. Iannetti et al., 2005). But it is also used

on it own, e.g., to study startle eye-blinks ([Blumenthal et al., 2005](#)) or arm movements ([van der Meer et al., 2010](#)).

2.1.5 Combined EEG/EMG with fMRI

The combined acquisition of EEG and fMRI allows to observe different indicators of the same activity at the same time. The “neural activity generating EEG potentials or MEG fields increases glucose and oxygen demands”, that are the “basis for a spatial correspondence between fMRI responses and HEEG/MEG source activity” ([Babiloni et al., 2004](#), p. 1472). With multi-modal integration, “a more complete picture” and “deeper insights” ([Rosenkranz & Lemieux, 2010](#), p. 2) to the activity of the brain are gained. Combined EEG and fMRI allow an “improved understanding of the spatiotemporal dynamics of brain activity” ([Mulert et al., 2004](#), p. 1).

While EEG offers high temporal but low spatial resolution, fMRI offers high spatial resolution with low temporal resolution. The combination of both methods allows to compensate the individual drawbacks ([Menon & Crottaz-Herbette, 2005](#); [Ritter & Villringer, 2006](#); [Rosenkranz & Lemieux, 2010](#); [Babiloni et al., 2004](#)).

It is important to note, that sources exist, which are only visible by one modality. For example, there are many incoherently firing neurons of which only 1 % are synchronous. This leads to a 30 times larger EEG signal but only a small metabolic difference and therefore a small fMRI signal ([Babiloni et al., 2004](#)). [Ritter and Villringer \(2006\)](#) classifies this into three cases

- fMRI signal without EEG correlate (deep, tangential, self-canceling),
- EEG signal without fMRI correlate (few synchronous neurons),
- opposite EEG and fMRI signals (synchrony, spatial scales).

Despite these problems, experiments with voltage-sensitive dye and with invasive electrical recordings concurrently with fMRI show that a good relation between sources of EEG and fMRI exists ([Babiloni et al., 2004](#)). The “fMRI signal is better correlated with the local field potential than with multiunit and single-neuron activity” ([Menon & Crottaz-Herbette, 2005](#), p. 296), which was also shown in humans ([Moser et al., 2010](#)). Since the EEG reflects local field potential it is save to assume that it has the same neural sources as fMRI ([Menon & Crottaz-Herbette, 2005](#)).

Several methods to combine the EEG and fMRI data (data fusion, multi-modal integration) are proposed. For single-trial EEG, the EEG signal is used as a covariate for the general linear model setup voxel by voxel of the

fMRI data. Averaged EEG (ERP) also allows to correlate the fMRI activation and the amplitude of ERP components. Additionally, the source localization of ERP waveforms can be constrained by the spatial information of fMRI activation (Menon & Crottaz-Herbette, 2005).

Inverse methods to locate the source of EEG activity show good precision under given conditions (Baillet et al., 2001; Michel et al., 2004). Mulert et al. (2004) performed source localization with the sole EEG data and found a mean Euclidean distance of the source of the P300-signal and the BOLD signal of 16 mm. Although this shows good concordance too, only minor disturbances in the EEG data can severely distort the source localization and lead to uncertainty and ambiguity (Ritter & Villringer, 2006). Therefore Ritter and Villringer (2006) suggest to use “fMRI data as a partial constraint” (p. 830) for source localization. This requires a mathematical model (mapping) of the cortex current dipole sources to the scalp potential distribution (modeling of forward problem) (Babiloni et al., 2004).

Although the concurrent data acquisition permits extended insights into brain activity, the acquisition equipment causes mutual interference. The artifacts in MRI images and fMRI data induced by the EEG recording are minimal or even don’t exist (Menon & Crottaz-Herbette, 2005). The influence of the MRI scanner to the EEG data on the other hand can be quite large. These artifacts will be detailed in the following section.

Several studies corrected the artifacts or used a blocked design to avoid artifacts for the significant sections of the EEG data. Only small differences to EEG recorded outside of the scanner were found (Menon & Crottaz-Herbette, 2005). Mulert et al. (2004) found a slightly reduced amplitude of the N1 and P1 components, which also were observed a little earlier. The P300 component didn’t change in size. Bregadze and Lavric (2006) also compared the P3 component and didn’t find differences. According to Moser et al. (2010) the SCP amplitudes are slightly smaller and their locations are comparable to recordings outside the scanner. Therefore they conclude that it is feasible to acquire DC-EEG in high magnetic fields (3 T).

2.2 MR Artifacts in the EEG Data

The rapidly changing magnetic fields of the MRI acquisition (see Sec. 2.1.1) induce an electric voltage in the conductors of the EEG/EMG/ECG electrodes. These artifacts superimpose the biological signals. Their amplitude

is several orders of magnitude larger than EEG signals and thus completely overlay them. Before the artifact signal itself is analyzed, the physical principles of its origin are investigated.

2.2.1 Electromagnetic Induction

Given is a surface \mathcal{A} as shown in Fig. 2.1 (Precht, 2006, p. 151, Fig. 9.1). Its perimeter, denoted as $\partial\mathcal{A}$, is the conductor of the electric circuit. A magnetic flux $\Phi(\mathcal{A})$ is flowing through this surface. According to the *law of induction*, the voltage along the perimeter, i.e., in the electric circuit, $U(\partial\mathcal{A})$, equals the decrease rate of the magnetic flux through the area (Precht, 2008, p. 109, eq. (20.1)).

$$U(\partial\mathcal{A}) = -\dot{\Phi}(\mathcal{A}) \quad (2.1)$$

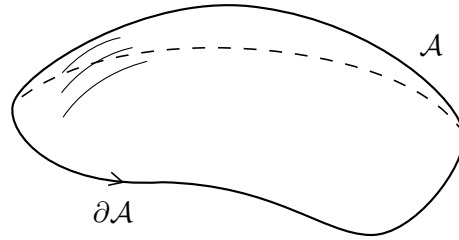


Figure 2.1: Exemplary area \mathcal{A} with perimeter $\partial\mathcal{A}$.

To calculate the total magnetic flux $\Phi(\mathcal{A})$ through \mathcal{A} , the surface is split into small pieces A_k . The total flux is the sum of the flux components through the small pieces. Each piece is assumed flat with the normal vector \vec{e}_{nk} and local magnetic flux density \vec{B}_k . The magnetic flux Φ_k through A_k is given by the product the area A_k with the normal projection of the magnetic flux density $B_{nk} = \vec{B}_k \cdot \vec{e}_{nk}$: $\Phi_k = A_k B_{nk}$. When further reducing the size of the pieces the sum converges to an integral and results in the compact formula (Precht, 2008, p. 16f, eq. (16.2))

$$\Phi(\mathcal{A}) = \int_{\mathcal{A}} B_n \cdot dA. \quad (2.2)$$

From eq. (2.2) two additive causes for a variation of the flux and thus of an induced voltage according to eq. (2.1) are possible:

- The magnetic flux density \vec{B} varies while the area \mathcal{A} stays constant. This case applies to a changing magnetic field through a stationary conductor.
- The area \mathcal{A} changes its form or position within a constant magnetic field. This case is referred to as moving conductor.

Both effects apply in concurrent fMRI and EEG measurements: The gradient coils constantly vary the magnetic flux density for spacial coding. Additionally small movements of the subject result in changes of the area spanned by the EEG electrode cables.

2.2.2 Gradient Artifact Signal

The EEG electrode leads and the tissue of the head (as a volume conductor, [Yan, Mullinger, Brookes, & Bowtell, 2009](#)) build a conductive loop. In this loop artifact voltages are induced as explained in the previous section. The main contribution is caused by the varying magnetic field for the gradient fields during fMRI acquisition. An exemplary artifact signal as recorded by the EEG amplifier after the 800 Hz anti-aliasing low-pass filter for the FMRI dataset (see Sec. 4.1.1) is shown in Fig. 2.2. The signal is caused by the acquisition of a single slice.

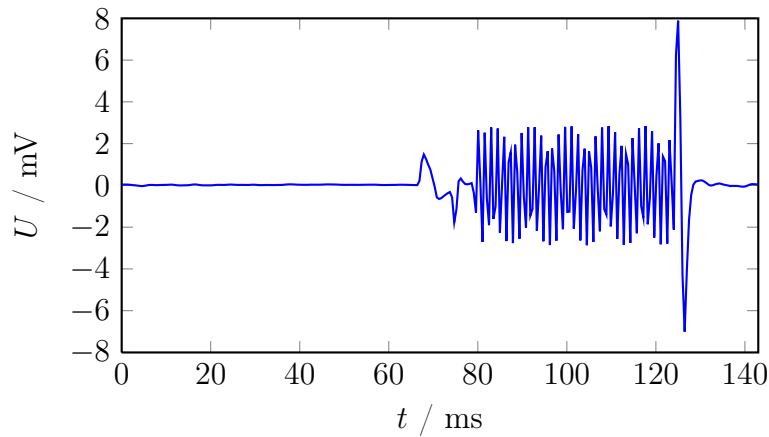


Figure 2.2: Exemplary artifact signal of a single fMRI slice acquisition measured with the Fp1 electrode from the FMRI dataset (see Sec. 4.1.1).

The spatial arrangement of the electrode leads and the position of the electrodes themselves build the area spanned by the loop. Its shape and its

position relative to the magnetic field determine the amount and spatial distribution of the “captured” magnetic flux. Together with its temporal variation as defined by the MRI sequence, these factors define the exact artifact signal. Therefore the artifact signal highly varies with the EEG electrode position (Yan et al., 2009). In Fig. 2.3 the artifact of all channels (i.e. EEG, EMG and ECG electrodes) of the FMRI dataset (see Sec. 4.1.1) are shown.

This high spatial variability was investigated by Yan et al. (2009). The maximum amplitude at any point of the scalp was determined in three ways. The voltage was calculated with analytical expressions assuming an ideal path of the electrode leads. Secondly, the digitized path of the electrode leads was used for a numerical simulation of the voltages. Finally, the voltages were measured during a combined EEG and fMRI acquisition with a specially crafted MR sequence.

With all three methods a high spatial variability was found. The values determined by both mathematical methods showed good correspondence to the measurements. The analytical expressions were used to show that, due to effects of the spherical wire paths, shifting and rotating the head results in a nonlinear increase or decrease of the artifact voltages. This information was used to minimize the artifact amplitude by optimizing the position inside the bore.

The mathematical methods could be used to precisely model the artifact signal and its variation due to the subject’s movement. Unfortunately the signal strongly depends on the exact wire paths and the materials, especially the tissue of the subject’s head. Hence, it is far too complex to accurately model it. However, these methods give a good opportunity to find general rules how to reduce the artifact amplitude without sacrificing the quality of the fMRI image and the EEG signal by the proper design of the wiring patterns of EEG caps, placement of the subject in the bore, and so on. However, the measured artifact signal will not be modeled with an accuracy of μV .

Gradient Artifact Dimensions

The raw artifact amplitude strongly depends on the change rate of the magnetic gradient field (which itself depends on the utilized fMRI sequence), the EEG electrode wire paths (loop area, orientation in the magnetic field), the EEG channel and the position of the head in the scanner (Yan et al., 2009).

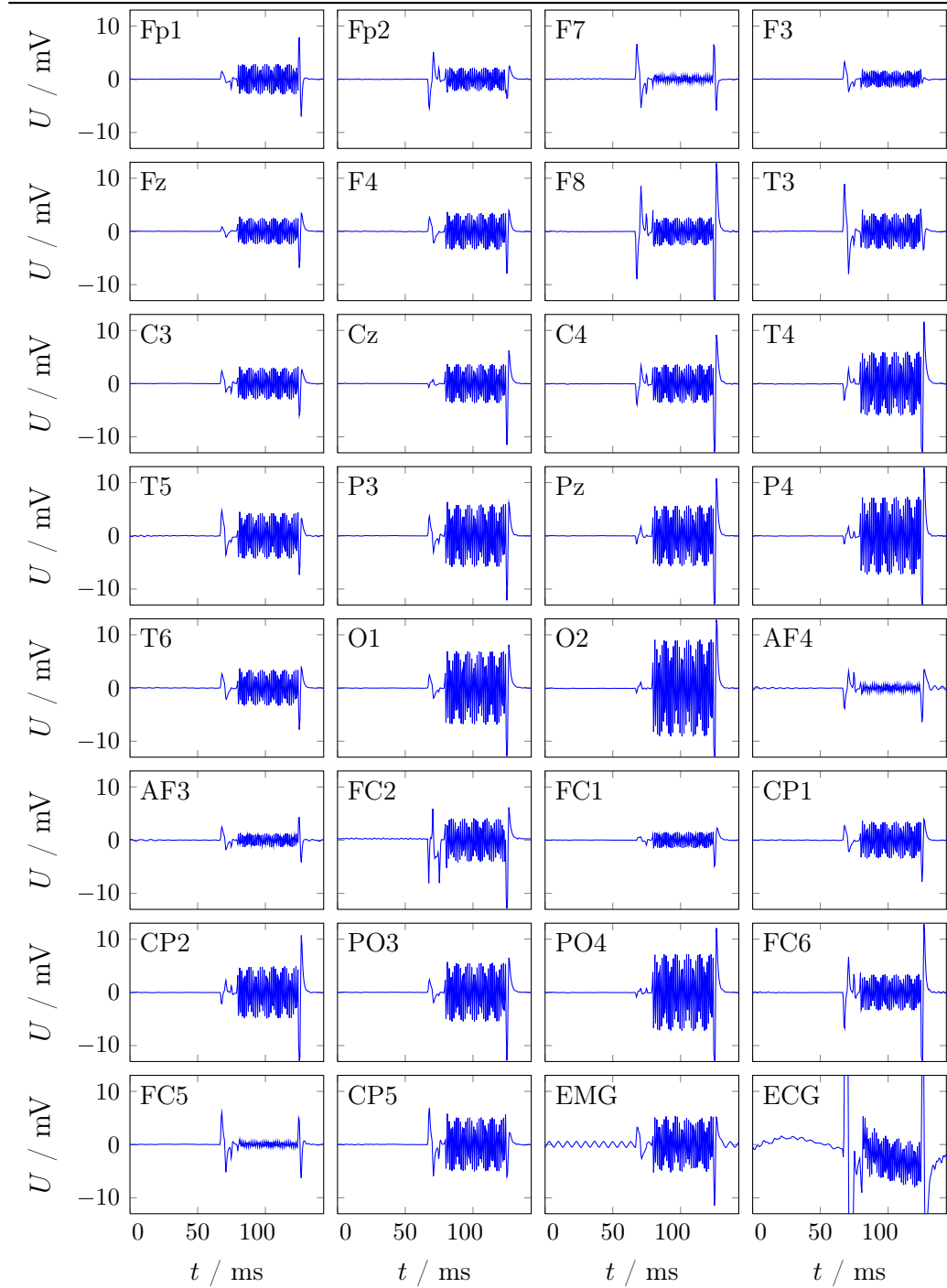


Figure 2.3: Artifact signal shape of all 32 channels of the FMRI dataset clearly showing the strong spatial variability.

The *measured* amplitude additionally depends on the analog input filter of the EEG amplifier¹ and its input voltage range. Table 2.1 summarizes amplitudes as reported by the given publications as well as of the data sets used in this work.

Allen et al. (2000) assumed a gradient slew rate of $125 \text{ T/m}\cdot\text{s}$ (resulting in a change rate of 25 T/s at 0.2 m distance from the isocenter) and a loop area of 100 cm^2 to calculate the raw artifact amplitude of $500 \text{ mV}_{\text{pp}}$. With a loop antenna they measured $25 \text{ mV}_{\text{pp}}$ using a low-pass filter with a 3 dB cut-off frequency of 70 Hz (2nd order Bessel), which reduced the fast artifact components. Measurements of a human revealed EEG artifacts from $0.6 \text{ mV}_{\text{pp}}$ to $17.3 \text{ mV}_{\text{pp}}$ and $16.3 \text{ mV}_{\text{pp}}$ for the ECG channel. After digitally down-sampling and low-pass filtering with $f_c = 50 \text{ Hz}$, the artifacts were $114 \mu\text{V}_{\text{pp}}$ to $2980 \mu\text{V}_{\text{pp}}$ with a median of $571 \mu\text{V}_{\text{pp}}$. Since these amplitudes are still much larger than biological signals, (Allen et al., 2000) conclude that a low-pass is not enough to remove the artifacts.

For their simulation, Schlegelmilch, Schellhorn, and Markert (2004) used an artifact with an amplitude of $15 \text{ mV}_{\text{pp}}$ as input for the presented correction algorithm. The measurements show an amplitude of $20 \text{ mV}_{\text{pp}}$.

Niazy, Beckmann, Iannetti, Brady, and Smith (2005) found a gradient artifact of $17 \text{ mV}_{\text{pp}}$ using a 600 Hz , 1st order low-pass.

From the many calculated and measured amplitudes given by Yan et al. (2009), only those actually measured are shown here. The measurements were performed with a well-defined gradient either in z or in x direction with a slew rate of $2 \text{ T/m}\cdot\text{s}$. To reflect a more typical slew rate of $100 \text{ T/m}\cdot\text{s}$, the values in Tab. 2.1 are scaled by a factor of 50.

A small artifact of $2.5 \text{ mV}_{\text{pp}}$ is shown by Mandelkow, Brandeis, and Boesiger (2010) using a 250 Hz low pass while van der Meer et al. (2010) show $22 \text{ mV}_{\text{pp}}$ with a similar filter.

From the FMRI dataset as used in this work (see Sec. 4.1.1) the data show amplitudes of $5.86 \text{ mV}_{\text{pp}}$ to $25.6 \text{ mV}_{\text{pp}}$. The pilot dataset has much larger artifacts ($117.1 \text{ mV}_{\text{pp}}$ to $642.4 \text{ mV}_{\text{pp}}$) with only a slightly wider low-pass (800 Hz instead of 600 Hz).

¹which is usually designed with a cut-off frequency below half of the sampling rate to avoid aliasing (Oppenheim, Willsky, & Nawab, 1997)

Table 2.1: Comparison of artifact dimensions (o:1: 1st order, o:2: 2nd order).

Reference	min.	Range max.	median	B	Low-pass
Allen et al. (2000) calculated measured largest ECG artifact EEG artifact digital low-pass 50 Hz		500.0 mV _{pp} 25.0 mV _{pp} 16.3 mV _{pp} 17.3 mV _{pp} 2.980 mV _{pp}		2 T 2 T 2 T 2 T 2 T	70 Hz o:2 70 Hz o:2 70 Hz o:2 70 Hz o:2 70 Hz o:2
	0.6 mV _{pp} 0.114 mV _{pp}		4.0 mV _{pp} 0.571 mV _{pp}		
Schlegelmilch et al. (2004) simulated measurements		15.0 mV _{pp} 20.0 mV _{pp} 17.0 mV _{pp}		1.5 T 1.5 T 3 T	1200 Hz o:2 1200 Hz o:2 600 Hz o:1
Niazy et al. (2005)					
Yan et al. (2009) phantom, z -gradient phantom, x -gradient human head, z -gradient human head, x -gradient		5.0 mV _{pp} 50.55 mV _{pp} 24.8 mV _{pp} 39.3 mV _{pp}		3 T 3 T 3 T 3 T	1000 Hz o:5 1000 Hz o:5 1000 Hz o:5 1000 Hz o:5
		2.5 mV _{pp}		3 T	250 Hz
Mandelkow et al. (2010)					
van der Meer et al. (2010)		22.0 mV _{pp}		3 T	250 Hz o:2
FMRIB dataset (Sec. 4.1.1)	5.86 mV _{pp}	25.6 mV _{pp}	17.9 mV _{pp}	3 T	600 Hz o:1
Pilot dataset (Sec. 4.1.2)	117.1 mV _{pp}	642.4 mV _{pp}	408.8 mV _{pp}	3 T	800 Hz

2.2.3 Ballisto-Cardiographic Artifacts (BCG)

The source of the gradient artifacts is the varied magnetic flux during active fMRI acquisition generated by the gradient coils. The second source of an induced voltage is the movement of the conductor in the static magnetic field (see Sec. 2.2.1). Even if the subject remains immobile, his pulsatile pulse flow induces a *pulse artifact* (Allen et al., 1998).

Figure 2.4 shows an exemplary signal recorded inside of a 1.5 T scanner before the fMRI acquisition. The pulse artifact has a “large amplitude peak followed by a complex waveform persisting throughout the interpulse period” (Allen et al., 1998, p. 230). It is recorded from almost all EEG electrodes and normally has amplitudes from $10\ \mu\text{V}$ to $150\ \mu\text{V}$ with a large inter-individual variability. Therefore it considerably perturbs the EEG acquisition.

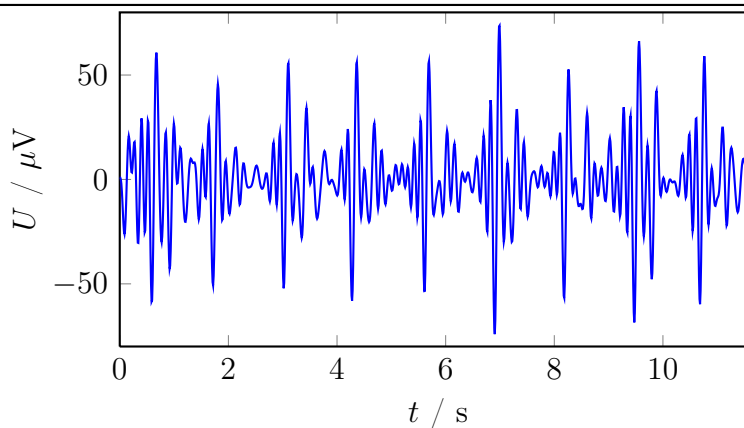


Figure 2.4: Exemplary ballisto-cardiographic artifact measured with the F7 electrode after filtering with a bandpass from 2 to 10 Hz from the FMRI dataset (see Sec. 4.1.1) well before fMRI acquisition onset.

Two sources are responsible for the pulse artifact. First, the small pulse-related body movements of the head and the expansion and contraction of scalp arteries lead to variation of the EEG electrode wire positions and therefore to an induced voltage in these conductors (Allen et al., 1998) proportional to B_0 (Debener, Mullinger, Niazy, & Bowtell, 2008). Secondly, as the blood itself is a conductive fluid, its flow generates the blood flow effect. When blood in a vessel flows perpendicular to the B_0 field, a voltage perpendicular to the flow and B_0 is induced. Its amplitude is proportional to B_0 , its velocity v and the orientation of the vessel relative to B_0 and reversely proportional to the distance to the EEG electrode (Kolin, 1952).

Debener et al. (2008) found large spatial variation of the BCG and suggests the removal channel by channel, e.g. utilizing the ICA. Niazy et al. (2005) calculated a PCA for the BCG artifact occurrences and used the first 3 PCs as template to be subtracted.

The methods to reduce pulse artifacts from EEG data are widely spread, therefore the BCG artifact is not further considered in this work.

2.3 Artifact Correction Algorithms

As summarized in Tab. 2.1, the amplitude of the gradient artifact exceeds the amplitude of EEG and EMG signals by several orders of magnitudes. The removal is therefore a non-trivial task. Filtering with low pass is not enough, because frequency components of the artifact overlap with the frequencies of interest for EEG and EMG signals (Allen et al., 2000).

Several algorithms to remove the artifacts were proposed. Goldman, Stern, Engel, and Cohen (2000) used an fMRI sequence with a slice acquisition duration of 90 ms followed by 580 ms without gradient activity. In the EEG data post-processing the periods of slice acquisition were zeroed, leaving a usable portion of the signal of 87 %. This high fraction was usable for their study, but a zeroed signal is not acceptable for other studies.

Within every channel, the artifact signal shape is a periodic function for the acquisition of every fMRI slice and/or volume (see Fig. 2.5). Many algorithms utilize this fact to calculate an artifact template (e.g. by averaging all slice artifacts) and subtract (Allen et al., 2000).

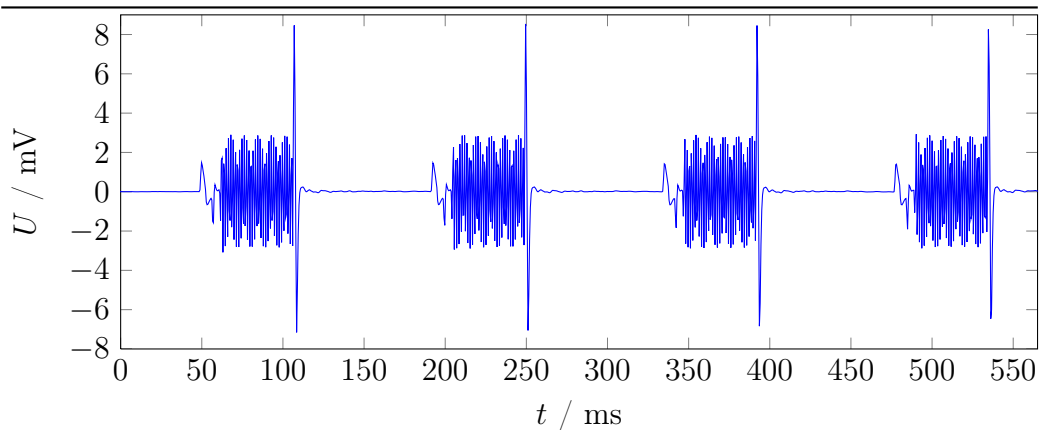


Figure 2.5: Exemplary section of the FMRI dataset (see Sec. 4.1.1) with four consecutive fMRI slice acquisition periods measured with the Fp1 electrode. It is clearly visible that the shape of the slices are very similar.

This template subtraction paradigm still leaves residual artifact signals which are larger than the biological signals (Allen et al., 2000). Therefore the calculation of the template is optimized and several pre-processing and post-processing steps are added by many authors. Figure 2.6 shows a generalized scheme for this group of algorithms (see also Sec. 3.2.4).

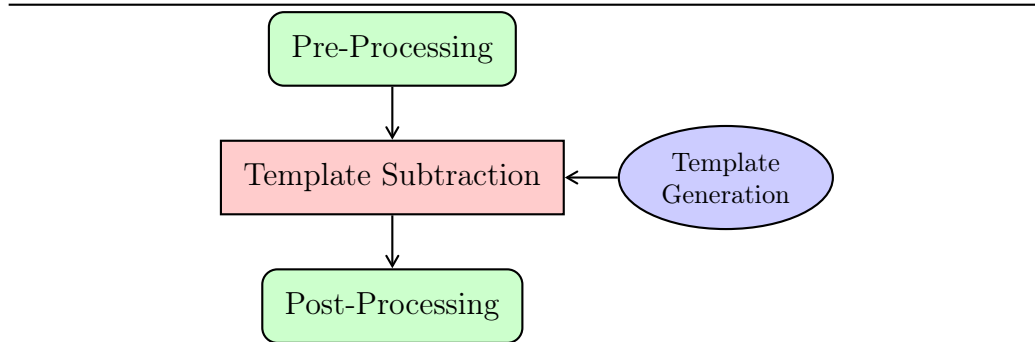


Figure 2.6: General approach of the artifact correction algorithms.

Within the next sections the following algorithms will be described in detail including their advantages and disadvantages:

- Sub-sample grouping (Bénar et al., 2003)
- Interpolation–template–alignment–subtraction (ITAS) (Ritter, Becker, Graefe, & Villringer, 2007)
- Image artifact reduction (Allen et al., 2000)
- fMRI artifact slice template removal (FASTR) (Niazy et al., 2005)
- Realignment parameter informed algorithm (Moosmann et al., 2009)
- Retrospective synchronization algorithm (Mandelkow et al., 2010)
- fMRI artifact reduction for motion (FARM) (van der Meer et al., 2010)

The processing of these algorithms is performed in time domain. Additionally the following algorithms will be outlined, which perform correction in frequency domain:

- Median power spectrum subtraction (Sijbers et al., 1999)
- Comb filter (Hoffmann et al., 2000)
- Frequency-domain filters (Hoffmann et al., 2000)

2.3.1 Average Artifact Subtraction

A simple implementation of the template subtraction paradigm calculates a single template by averaging all epochs. Several factors diminish the success

of this approach. The following sections present these factors as well as proposed solutions by published algorithms.

Sub-Sample Grouping

The begin of an fMRI volume and/or slice acquisition is not synchronized with the EEG sampling. For example, at a sampling rate of 1 kSps, i.e. a sampling period of 1 ms, the start of one slice can be 0.1 ms before an EEG sampling, the next slice could start at 0.3 ms after the EEG sampling.

[Bénar et al. \(2003\)](#) divided the EEG sampling interval into ten partitions. Every epoch (EPI volume) was assigned to one of these ten bins, depending on the exact start of the MR acquisition relative to the EEG sampling. Finally, individual templates for every bin were calculated and subtracted.

This approach reduces the problem arising from unsynchronized fMRI and EEG acquisition. The problem is not corrected perfectly, because only ten bins were used, which still left remaining uncertainties. Since the template was built from epochs all over the long exploration, the authors reported problems with movements of the subject.

Interpolation-Template-Alignment-Subtraction (ITAS)

The problem of a missing synchronization between the fMRI acquisition and the EEG sampling was also considered by [Ritter et al. \(2007\)](#). Contrary to calculating separate templates for every individual sub-sample offset, they aligned every epoch to maximize its cross-correlation with a reference epoch. This alignment was performed with an up-sampled data and then down-sampled again.

The template was calculated by averaging all epochs, but using a weighted sum which attenuated epochs with higher distance. This reduces the impact of changes of the artifact waveform. Similar to [Bénar et al. \(2003\)](#), the interpolation was performed in discrete steps which leaves uncertainties.

Block-wise processing

If the data shows a small drift or if the subject has moved during the acquisition, the calculated template will not fit well for any epoch. This results in a high residual artifact.

To avoid this problem, the template generation and subtraction is performed block-wise by [Allen et al. \(2000\)](#). The template was calculated by averaging n consecutive epochs and then subtracted from them. This was repeated with every next n epochs.

To further reduce the impact of atypical epoch signals, the averaging didn't necessarily include all n epochs. After the first five epochs were averaged, the remaining epochs were added iteratively, but only if their cross-correlation to the current average exceeded 0.975.

For an fMRI EPI sequence which had short gaps between the acquisition of every volume, the whole volume was used as an epoch, of which $n = 25$ were averaged per block. Additionally, for two subjects a continuous fMRI sequence without gaps between volumes was acquired. This allowed to choose the slices as epoch and a block length of $n = 100$.

The resulting signal was filtered with a high order low-pass with $f_c = 80$ Hz and down-sampled to 200 Sps. The EEG signal still contained residual artifacts with approximately 30–50 μ V. Therefore a post-processing step with adaptive noise cancellation ([Widrow et al., 1975](#)) was applied to the data. To generate the reference signal, pulses at the epoch timing instances were filtered with the same low-pass as the EEG signal ([Allen et al., 2000](#)).

The use of short periods (blocks) for the template generation as well as the exclusion of atypical epochs greatly reduces the impact of subject movement. The problem of missing synchronization was tackled by recording the slice time with a higher resolution of 10 μ s than the EEG sampling period of 200 μ s (5 kSps). The EEG was up-sampled using a sinc-interpolation ([Oppenheim et al., 1997](#), p. 523) before template calculation, similar to [Ritter et al. \(2007\)](#). This reduced the sampling problem but the block-wise processing still does not provide a satisfying solution for movement artifacts. The first five epochs in each block have an outstanding impact on the template, because all further epochs are excluded if not similar enough.

2.3.2 FMRI Artifact Slice Template Removal (FASTR)

The FMRI artifact slice template removal (FASTR) algorithm was introduced by [Niazy et al. \(2005\)](#) and [Iannetti et al. \(2005\)](#). Similar to [Allen et al. \(2000\)](#), it uses triggers from the MR scanner which indicate the slice timing. The difference is that here the triggers have the same temporal resolution as the EEG sampling.

As the title indicates, the algorithm calculates templates for every slice of the EPI sequence. To tackle the problem of unsynchronized acquisition, the EEG data is up-sampled by a factor of 10. While [Ritter et al. \(2007\)](#) performs a time-shift of the data and then down-sample it again, here the trigger indices are adjusted within the refined time resolution and further processing is performed before down-sampling.

After applying a 1 Hz high-pass filter to reduce baseline effects of slow drifts, the artifact template is calculated as a local moving average of a configurable number of slice segments before and after the current one. Only every second slice is used so that the EEG signal is uncorrelated between slices. This template is multiplied by a factor to minimize its squares to the segment.

The next stage is the first post-processing step (compare Fig. 2.6). The principal component analysis (PCA) is used to calculate a set of basis functions for the residuals. Those components describing the most variance (called optimal basis set (OBS) by [Niazy et al., 2005](#)), are again scaled to minimize the squared error and added to the artifact template signal from the previous stage which is then subtracted from the EEG signal.

In the next step, this estimated error signal and the EEG signal with the artifact templates subtracted are down-sampled and filtered by a 70 Hz low-pass. Similar to [Allen et al. \(2000\)](#), as a second post-processing step, adaptive noise cancelling (ANC) is used with the reference being the estimated error signal.

The algorithm tackles the problem of unsynchronized sampling and fMRI clocks, but only with a limited quantization equal to the up-sampling factor. This still leaves considerable residual artifacts. Calculating the slice templates using a moving average (instead of block-wise, like [Allen et al., 2000](#)) assigns identical influence to every epoch and adopts to slow changes of the artifact signal. However, sudden movements of the subject poison the template of all surrounding epochs. The new post-processing step using a principal component analysis greatly removes residual artifacts.

2.3.3 Realignment Parameter Informed Algorithm

The previous algorithm uses a moving average to calculate the artifact template. This solves the problem of slow drifts of the artifact shape ([Moosmann et al., 2009](#)). Still problematic is the case, when an abrupt change of the artifact signal occurs. While a movement of the subject of 1.5 mm is reported

for 30 % of all recordings, a displacement of 1 mm already impairs the result of Allen et al. (2000) (Moosmann et al., 2009).

The calculated artifact template is an average of the shape before and of the shape after the abrupt change. The two regions “pollute” the template and lead to suboptimal results. Therefore, the data before and after the abrupt change “should not be used together to form one template” (Moosmann et al., 2009, p. 1146).

Moosmann et al. (2009) use the fMRI realignment parameters calculated from the image data, which specifies the head displacement and rotation from one volume acquisition to the next. If the movement exceeds a certain threshold, the EEG data during this interval is not used for the calculation of the artifact template. Furthermore, these points define barriers for the sliding average algorithm.

The algorithm reduces the impact of subject movements to the EEG signal, but requires data from the fMRI pre-processing.

2.3.4 Retrospective Synchronization Algorithm (Resync)

The problem of unsynchronized clocks of the EEG recording system and the MR scanner was tackled by several procedures already covered above. Mandelkow et al. (2010) introduce the retrospective synchronization of the EEG data to the MR scanner clock. The de-synchronization factor D

$$D = \frac{\text{round}(\text{TR} \cdot F_S)}{\text{TR} \cdot F_S}$$

(TR: MR repetition time, F_S : EEG sampling rate) expresses the factor by which the EEG sampling frequency is off an integer multiple of the MR repetition time and is near one $D \approx 1$.

Instead of calculating the value from the (unknown) TR and F_S , it is estimated from the EEG data by maximizing the cross correlation of a time-shifted version of the artifact. The resynchronized signal is calculated with an inverse Fourier transform with the interpolation factor D . Contrary to the previously mentioned algorithms, all calculations are performed in frequency domain and thus avoid up-sampling of the data.

This algorithm introduces new methods to tackle unsynchronized EEG and fMRI acquisition. On the other hand, no special measures are taken to avoid problems with subject movement.

2.3.5 fMRI Artifact Reduction for Motion (FARM)

All algorithms presented so far work well with EEG but experience difficulties with motion. The inherent motion involved with measuring EMG leads to induced voltage during the movement as well as an altered shape of the artifact signal due to the different layout of the conductive loop (compare Sec. 2.2.1).

A correction algorithm specifically for EMG data was presented by [van der Meer et al. \(2010\)](#). It is largely based on the algorithm by [Niazy et al. \(2005\)](#) (see Sec. 2.3.2) and adds several improvements and adoptions to be applicable for EMG data. In the pre-processing step (compare Fig. 2.6) a 30 Hz high-pass is added, since the frequency range of EMG data is from 30 Hz to 250 Hz.

One major improvement is to consider fMRI sequences which include a short gap between every volume acquisition. At this points, the volume artifact is present, which also extends into the slice artifacts before and after the gap. It is replaced by synthesized data which is calculated from slice artifacts more than one slice away. Additionally, the slice timing as well as the duration for the gap are estimated. Contrary to [Niazy et al. \(2005\)](#), the slice markers are not quantized with the (up-sampled) sampling frequency but calculated with a sub-sample resolution, similar to [Ritter et al. \(2007\)](#).

The template generation is improved by using a larger sliding window of 50 slices, but choosing a set of 12 artifacts with the highest correlation to the current artifact. In the post processing step, the data is filtered with a 250 Hz low-pass to conserve the frequencies of interest for EMG ([Niazy et al. \(2005\)](#) uses a 70 Hz low-pass). The final ANC applied by [Niazy et al. \(2005\)](#) is not used by [van der Meer et al. \(2010\)](#).

By choosing the epochs with the best fit to the current epoch, a well suited template is generated. It most probably does not contain epochs with subject movement or with an altered shape of the artifact due to changed position of the electrode leads. The synchronization problem is solved by shifting the epoch temporally with a sub-sample resolution. However, the algorithm is strongly tailored to EMG data and removes frequency components below 30 Hz. In this range important EEG information is present.

2.3.6 Frequency Domain Template Removal

While the algorithms outlined up to this point perform the signal processing in time domain, the following approaches work in frequency domain. The repetitive application of the gradient fields leads to a periodic artifact signal. In frequency domain this corresponds to a discrete frequency and its harmonics (Oppenheim et al., 1997). Hoffmann et al. (2000) systematically investigated the sources of multiple frequency components originating from by fMRI acquisition. These come from the periods of the volume, the slice, and the readout gradient fields.

Median Power Spectrum Subtraction. Sijbers et al. (1999) divided the EEG data into sections with a length of TR (for slow imaging sequences) and a length of multiple TRs for fast imaging sequences (resulting in a length of 150 to 300 ms). The latter was necessary because the artifacts lasted longer, i.e. decayed slower, than TR and therefore superimposed with the following artifacts.

For each section the power spectrum was calculated and averaged using a sliding window median filter of 15 sections for slow and 31 sections for fast imaging sequences. This template was scaled to minimize the mean squared error to the current interval and subtracted. Finally an inverse Fourier transform was performed to calculate the cleaned EEG signal.

This algorithm was evaluated for the standard imaging MR sequences Spin Echo (SE), Gradient Echo (GE) and Diffusion Weighted (DW) but not for EPI. The subject was an anesthetized rat, so no movement related problems are expected. The experiment was performed with a 7 T scanner with a 80 mm bore.

The acquisition of the EEG and the artifact was performed in two separate sessions. The EEG was recorded with the anesthetized rat but without MR acquisition, while the artifacts were recorded using a dead rat. The input for the artifact reduction algorithm was the sum of the EEG and the artifact signal. This allowed to compare the corrected signal with the true uncorrupted signal.

As performance indicator the authors introduced the signal-to-artifact ratio which is defined as the standard deviation of the pure EEG signal divided by the standard deviation of the residual or full artifact. Note that although the definition resembles the SNR (see Sec. 2.4.3), it relates signal RMS values instead of the signal power values.

The recorded artifact was very small with an RMS of only 29 % to 71 % of the EEG signal RMS. After the application of the correction algorithm, the residual artifact was 7 % to 18 %, respectively (Sijbers et al., 1999).

As the authors report, the correction algorithm is based on the power spectrum. This removes the phase information in frequency domain and thus leads to signal distortion in time domain. Due to the small dimensions of a rat's head, only small wire loops and therefore small gradient artifact voltages were observed. The authors did not show the performance of the algorithm for larger artifact voltages.

Comb Filter. The algorithm of Sijbers et al. (1999) does not depend on the previously mentioned periodicity of the MR artifacts, because it calculates a frequency domain template for the whole spectrum. Contrastingly, Hoffmann et al. (2000) used a comb filter with narrow notches at the slice frequency and its harmonics as well as one volume frequency above and below them. This was implemented in time domain with FIR filters (Oppenheim et al., 1997). Although no quantitative evaluation, the corrected signal allowed the identification of epileptic spike waves. The applied comb filters have a finite stop band attenuation. Due to the high amplitude of the gradient artifact signal, considerable residual artifacts are expected.

Frequency Domain Filter. For a greater reduction of the artifact amplitude, the filtering can be performed in frequency domain by setting the amplitude to 0.0 at the according frequency bins (Hoffmann et al., 2000).

The implementation was split into two parts. Firstly, an averaged and smoothed spectrum of an unaffected EEG was calculated. Secondly, every amplitude of the corrupted EEG signal, which exceeded the value of the unaffected EEG by more than 50 %, was set to zero. This approach again does not rely on the knowledge of the MR sequence repetition times.

Bénar et al. (2003), who also used this approach, reported severe ringing at block boundaries, due to the ideal filter characteristic (Oppenheim et al., 1997).

2.4 Performance Indicators

To assess the quality of results after the application of a correction algorithm, multiple criteria were employed. In this section, these are summarized and grouped by their underlying physical or numerical property.

The following performance indicators are investigated:

- Amplitude
 - Median Imaging Artifact
- RMS
 - RMS Corrected to Unimpaired
 - RMS Uncorrected to Corrected
- SNR
 - Pseudo-SNR
 - Exact SNR from Correlation
- Frequency Domain
 - Median Residual Activity.
 - Power Density at Slice Frequency
 - Spectrograms
 - Residual Normalized Error Power
 - Average Spectrum
 - Surrogate Biosignal Preservation
- Qualitative
 - Epileptiform Spike-waves
 - α -Rhythm
 - BCG Artifact
 - ECG Quality
 - Principal Component Analysis

2.4.1 Amplitude

The simplest physical property is the sole signal amplitude, summarized with the median.

Median Imaging Artifact. [Allen et al. \(2000\)](#) calculate the median imaging artifact for the raw EEG data, two intermediate steps, and the final cor-

rected data. Therefore “[...] the mean of 10 measurements, made at equally spaced intervals [...], was calculated for each channel.” This mean value was calculated for every channel, subject and recording, from which finally the median value was taken. Although the publication does not specify what is meant by “measurement”, it is assumed that it specifies the range (i.e. peak to peak value) of the EEG data within an interval of a length slightly over the fMRI slice time.

The final comparison showed a “500-fold reduction” of the signal amplitude from $4.0 \text{ mV}_{\text{pp}}$ with the artifacts to $8.0 \mu\text{V}_{\text{pp}}$ with the artifacts removed. Although the reduction shows the efficacy of the correction algorithm, it does not show whether the resulting signal amplitude is comparable to a non-corrupted EEG signal.

2.4.2 RMS Ratios

The Root-Mean-Square value (RMS) is the quadratic mean of a signal and is defined for a continuous time signal $x(t)$ and discrete time signal x_i by

$$x_{\text{RMS}} = \sqrt{\frac{1}{T} \int_0^T x^2(t) dt} = \sqrt{\frac{1}{n} \sum_{i=1}^n x_i^2}, \quad (2.3)$$

respectively. It is the square-root of the signal *power* because the signal values are squared. Apart from the signal mean (i.e. the DC value) it is identical to the (biased) standard deviation of the signal (Glover & Grant, 2004).

RMS Corrected to Unimpaired. One “evaluation metric” of Moosmann et al. (2009) is the standard deviation of the corrected signal, compared to the standard deviation of the physiological EEG signal during artifact free periods. This performance indicator represents the fraction of the corrected to the pure signal. If the ratio is greater than 1, residual artifacts are still present while values below 1 show that the correction algorithm removed parts of the wanted signal.

RMS Uncorrected to Corrected. van der Meer et al. (2010) compare their algorithm with the algorithm of Niazy et al. (2005) by calculating the ratio between the RMS of uncorrected EMG periods and artifact-corrected EMG periods. The bigger this ratio the better, i.e., the more artifact was

removed, but the same problem as noted in Sec. 2.4.1 applies here too: This value doesn't show whether the algorithm has removed too much of the signal. In this case [van der Meer et al. \(2010\)](#) use the ratio to show that their algorithm removes more of the artifacts than [Niazy et al. \(2005\)](#) do.

2.4.3 Signal to Noise Ratio

The Signal to Noise Ratio (SNR) relates the power of a wanted signal to the power of a superimposed noise signal. The SNR of a distorted signal $x(t) = x_S(t) + x_N(t)$ or $x_i = x_{S,i} + x_{N,i}$ is defined as the power S of the undistorted signal $x_S(t)$ or $x_{S,i}$ divided by the power N of the noise $x_N(t)$ or $x_{N,i}$ ([Lee & Messerschmitt, 2000](#))

$$\text{SNR} = \frac{S}{N} = \frac{\int_0^T x_S^2(t) dt}{\int_0^T x_N^2(t) dt} = \frac{\sum_{i=1}^n x_{S,i}^2}{\sum_{i=1}^n x_{N,i}^2}, \quad (2.4)$$

for continuous time and discrete time signals, respectively. It is usually converted to decibel (dB) due to the large dynamic range of the value

$$\text{SNR}_{\text{dB}} = 10 \log_{10} \left(\frac{S}{N} \right). \quad (2.5)$$

Note, that the definition relates the signal *power* values, which are the square of the signal RMS values (compare eqn. 2.3).

Pseudo-SNR. [Moosmann et al. \(2009\)](#) added a surrogate single trial ERP ([Quiroga & Garcia, 2003](#)) to the raw EEG data and compared it to the ERP after artifact correction. A 5 Hz 7 μV sine with random time jitter was used. The authors define the SNR as

$$\begin{aligned} \text{SNR} &= \left[\frac{\text{cov}(\text{ERP}_{\text{original}}, \text{ERP}_{\text{corrected}})}{\sigma_{\text{ERP}_{\text{original}}} \cdot \sigma_{\text{ERP}_{\text{corrected}}}} \right]^2 \\ &= \text{corr}(\text{ERP}_{\text{original}}, \text{ERP}_{\text{corrected}})^2 \end{aligned} \quad (2.6)$$

(see eq. (9) on p. 1147), i.e. by squaring the correlation coefficient of the original and the corrected signal.

Exact SNR from Correlation. The calculation of the SNR from the correlation coefficient with equation (2.6) (Moosmann et al., 2009) is only an approximation for low values of the correlation coefficient. This can easily be validated since the range of that value would be 0–1 which does not cover the range of a real SNR.

For an exact derivation let the original signal $x(t)$ be modeled as a wide-sense stationary random process $X(t)$ (Weinrichter & Hlawatsch, 1991). Its signal power is given by $S = \mathcal{E}\{X(t)^2\}$ where $\mathcal{E}\{\cdot\}$ is the expected value (Lee & Messerschmitt, 2000, p. 50).

The cross-correlation of two real, zero-mean and jointly wide-sense stationary random processes $X(t)$ and $Y(t)$ is given by $R_{XY}(t, \tau) = \mathcal{E}\{X(t)Y(t - \tau)\}$. The Pearson correlation coefficient $\rho_{XY}(t)$ is derived from $R_{XY}(t, \tau)$ by setting $\tau = 0$ and dividing by the standard deviations $\sigma_X = \sqrt{\mathcal{E}\{X(t)^2\}}$ and $\sigma_Y = \sqrt{\mathcal{E}\{Y(t)^2\}}$ (Lee & Messerschmitt, 2000, p. 55ff). Substitution finally gives the expression for the correlation coefficient

$$\rho_{XY}(t) = \frac{\mathcal{E}\{X(t)Y(t)\}}{\sqrt{\mathcal{E}\{X(t)^2\}\mathcal{E}\{Y(t)^2\}}}. \quad (2.7)$$

Two new signals $X_1(t) = X(t) + \eta_1(t)$ and $X_2(t) = X(t) + \eta_2(t)$ result from $X(t)$ by the addition of two different zero-mean noise signals $\eta_1(t)$ and $\eta_2(t)$ (again wide-sense stationary random processes). Their power is given by $N_i = \mathcal{E}\{\eta_i(t)^2\}$. $X(t)$, $\eta_1(t)$ and $\eta_2(t)$ are mutually uncorrelated.

The correlation coefficient (Borga, 2001)² of the two signals $X_1(t)$ and $X_2(t)$ with arbitrary amplification by the factors a and b , respectively, is given by (the time parameter (t) is omitted for better readability)

$$\begin{aligned} \rho &= \frac{\mathcal{E}\{a(X + \eta_1) \cdot b(X + \eta_2)\}}{\sqrt{\mathcal{E}\{a^2(X + \eta_1)^2\} \cdot \mathcal{E}\{b^2(X + \eta_2)^2\}}} \\ &= \frac{\mathcal{E}\{X^2\}}{\sqrt{(\mathcal{E}\{X^2\} + \mathcal{E}\{\eta_1^2\}) \cdot (\mathcal{E}\{X^2\} + \mathcal{E}\{\eta_2^2\})}} \\ &= \frac{S}{\sqrt{(S + N_1)(S + N_2)}}. \end{aligned} \quad (2.8)$$

For the special case³ that the first signal equals the original signal (i.e. $\eta_1 = 0$, $N_1 = 0$) and the second signal is the corrupted signal (the “noise” corresponds

²<http://www.imt.liu.se/~magnus/cca/tutorial/node10.html> [2012-01-05]

³<http://www.imt.liu.se/~magnus/cca/tutorial/node12.html> [2012-01-05]

to the error (signal) introduced by the correction algorithm), the correlation coefficient simplifies to

$$\rho = \frac{S}{\sqrt{S(S+N)}}. \quad (2.9)$$

From this equation, the signal-to-noise ratio SNR can be derived as

$$\text{SNR} = \frac{S}{N} = \frac{\rho^2}{1 - \rho^2}. \quad (2.10)$$

For low values of ρ the denominator approaches one

$$\lim_{\rho \rightarrow 0} (1 - \rho^2) = 1$$

and thus (2.10) simplifies to $\text{SNR} \simeq \rho^2$, which is identical to (2.6).

As assumed by Moosmann et al. (2009), the SNR of the ERP signal after the application of their artifact correction algorithm can be calculated from numeric data. However, while in their case *high* values for the correlation coefficient ρ with the original surrogate ERP signal are desired, the utilized formula (2.6) is only an approximation for *low* values of the correlation coefficient ρ . Therefore the exact formula (2.10) should be used.

2.4.4 Analysis in Frequency Domain

Various evaluation criteria were used by different authors which partly investigate EEG signal frequency bands and others investigate fMRI acquisition fundamental and harmonic frequencies.

Median Residual Activity. The mean activity in four representative EEG frequency bands (0.8–4 Hz (Delta waves), 4–8 Hz (Theta waves), 8–12 Hz (Alpha waves) and 12–24 Hz (part of the Beta wave spectrum)) was calculated by Allen et al. (2000). Therefore the average spectrum from ten 5.12 s periods (i.e., 1024 samples at 200 Sps) was determined for every channel and subject. Then the mean activity in every frequency band of the corrected signal (A_{IAR}) was compared to the mean activity during no fMRI acquisition (A_{NI}) by calculating the absolute value of the relative difference in percent

$$\text{Percentage Difference} = 100 \% \times \left| \frac{A_{\text{IAR}} - A_{\text{NI}}}{A_{\text{NI}}} \right|.$$

To summarize the percentage difference values, the median (due to non-normality) for all channels and subjects was determined. This performance indicator is a measure for the deviance of the corrected signal in EEG frequency bands.

Power Density at Slice Frequency. For the evaluation of their algorithm, Niaz et al. (2005) calculated the spectral power density at the slice frequency fundamental and harmonics. They compared the values for the data before, for some intermediate steps of the algorithm and for the final output. These indicate the attenuation of the fMRI noise base frequency and its harmonics achieved by the artifact correction algorithm.

For the practical calculation of the power spectral density the data is transformed from time domain to frequency domain with a discrete Fourier transform (DFT).⁴

Only periodic signals which exactly fit into the total DFT length, i.e. which have an integer number of periods, result in a single frequency bin. Signals with a non-integer number of periods also contribute to neighboring frequency bins. This so called “Leakage effect” (Doblinger, 2001; Glover & Grant, 2004) also was reported by Niaz et al. (2005). However, they didn’t further consider the considerable amount of signal power outside of the main bins of the slice frequency and its harmonics.

The disregarded leaked signal power can lead to a substantial error in the calculation of the slice frequency power density. This problem is reduced by the fact, that the comparison was performed between the values of the original signal and the corrected signal, which both had the same leakage conditions.

A second problem arises from the width of the frequency bins, which is inversely proportional to the total length of the signal. Therefore the evaluation of the correction result of an acquisition with a short fMRI activity has wider frequency bins and therefore higher spectral power values than a dataset with a long fMRI session. Again, since the comparison is performed between two equal length datasets, the problem equally applies to both and is cancelled.

Spectrograms. The visual representation of the time course of power spectral density of a signal is called *spectrogram* (see Fig. 2.7 for an example).

⁴For the calculation of a DFT usually the FFT (fast Fourier transform) is used, which is a very efficient implementation of the algorithm (Oppenheim et al., 1997; Doblinger, 2004).

This is used by [van der Meer et al. \(2010\)](#) to visualize the decreased power at slice harmonics achieved by their correction algorithm, compared to the algorithm of [Niazy et al. \(2005\)](#). Although the underlying data enables a quantitative analysis, the authors only suggest visual inspection.

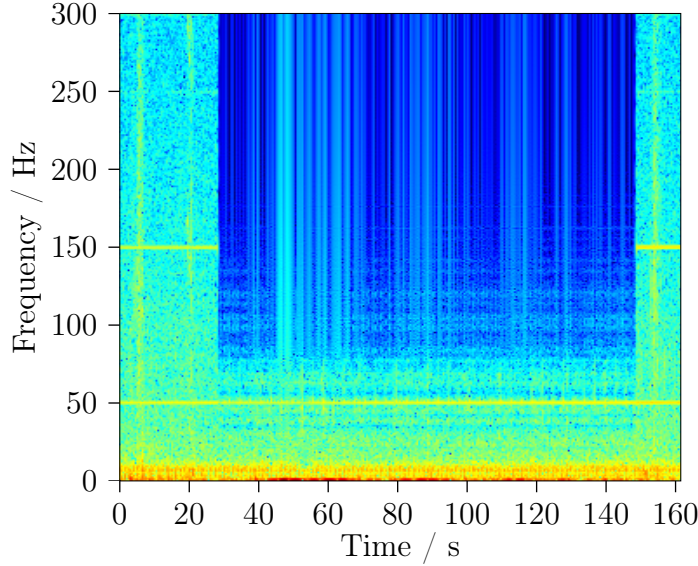


Figure 2.7: Exemplary spectrogram with a frequency resolution of 1 Hz and temporal resolution of 0.5 s. It shows the spectral contents of the FMRI dataset after correction with the algorithm presented by [Niazy et al. \(2005\)](#) (the hotter the color the more activity).

Residual Normalized Error Power. [Mandelkow et al. \(2010\)](#) calculate the power spectral density of the corrected signal $S_{\text{corrected}}(f)$ and of the baseline signal without fMRI acquisition $S_{\text{without}}(f)$. The normalized power spectral density is then calculated by $S_{\text{corrected}}(f)/S_{\text{without}}(f)$. The residual error is given by subtracting the expected value 1. The power $C|_{f_1}^{f_2}$ is calculated by summing up along the frequency from f_1 to f_2 .

$$C|_{f_1}^{f_2} = \sum_{f=f_1}^{f_2} \left| \frac{S_{\text{corrected}}(f)}{S_{\text{without}}(f)} - 1 \right|$$

The residual normalized error power is calculated for six frequency bands (< 20 Hz, < 40 Hz, < 90 Hz, < 190 Hz, < 690 Hz, < 990 Hz) and visualized as stacked bar graphs. This performance indicator is very similar to the median residual activity ([Allen et al., 2000](#)) above. Instead of 5.12 s periods

it uses the whole signal, and calculates the signal power in different frequency bands.

Average Spectrum. For every subject, the EEG acquisition data without acquisition, with acquisition, and after correction was split into 120 epochs of 8000 samples (1.6 s) (Ritter et al., 2007). For every epoch the FFT was calculated and averaged for each of the three cases separately. One number for each of six frequency bands corresponding to EEG bands was calculated (presumably by summing the frequency domain values). These numbers were compared in three ways: a) corrected without fMRI acquisition vs. corrected with fMRI acquisition, b) corrected with fMRI acquisition vs. uncorrected without fMRI acquisition and c) corrected without fMRI acquisition vs. uncorrected without fMRI acquisition.

Surrogate Biosignal Preservation. Ritter et al. (2007) added six continuous sine waves with certain frequencies from 3 Hz to 120 Hz and an amplitude of $100\ \mu\text{V}$ to the EEG data set. After performing the investigated artifact correction algorithms, the resulting data was visualized with spectrograms. The evaluation of the preservation of the surrogate signals was done by visual inspection.

2.4.5 Qualitative Performance Indicators

Besides the mathematical evaluation, there are also methods which require a human reviewer to rate the data. Although these methods cannot be used as reproducible and reliable performance indicators (Mandelkow et al., 2010), they often represent the practical usage of the corrected data (e.g. Allen et al., 2000).

Epileptiform Spike-waves. Spike-waves, recorded from a subject with epilepsy, were added to the raw EEG data of the healthy subjects at random times (Allen et al., 2000). This data was then corrected with their algorithm and reviewers had to identify these spike-waves. The proportion of correctly identified was used as an indicator of the quality of the corrected data.

α -Rhythm. Allen et al. (2000) and Niazy et al. (2005) identified α -rhythm in the corrected data and compared the channel and frequency to recordings of the same subject outside the scanner.

BCG Artifact. The presence of BCG artifacts, which show a distinct shape, equal with and without an active fMRI acquisition, were required to be present after the artifact removal by [Niazy et al. \(2005\)](#).

ECG Quality. The ECG signal has a unique shape. [Niazy et al. \(2005\)](#) asked reviewers to classify the quality of the features in the ECG signal after the artifact removal.

Principal Component Analysis. [Mandelkow et al. \(2010\)](#) used a principal component analysis (PCA) and visually inspected the leading principal components whether they are similar to the residual gradient artifact as well as “their contribution to the overall variance” (p. 2294).

3

FACET — A New Correction Toolbox

BASED on the algorithms summarized in Sec. 2.3 a new universal and flexible toolbox with improved artifact correction results is developed. This toolbox is called “FACET – A Flexible Artifact Correction and Evaluation Toolbox”. The algorithm by Niaz et al. (2005) is used as starting point. With the process of software re-engineering the Matlab code is reimplemented with the object-oriented design paradigm. This enables flexibility, maintainability and extensibility.

Dedicated tools for the analysis of the EEG input data as well as methods to correct faulty trigger recordings are implemented. Multiple algorithmic improvements are introduced which lead to an extended correction of the artifacts. To allow the flexible configuration of the algorithm and to ensure reproducible results, the setup and execution is guided by a configuration file instead of a graphical dialog. The toolbox is complemented by a dedicated framework for the evaluation of artifact correction algorithms using selected performance indicators as summarized in Sec. 3.11.3.

The goal is to provide a flexible toolkit which allows to combine algorithm components as required to acquire the best artifact correction results. These should surpass the quality of existing algorithms.

3.1 Starting Point

This work is mainly based on the correction algorithms by Niazy et al. (2005) and van der Meer et al. (2010).

3.1.1 EEGLAB, FMRIB Plugin

The FASTR algorithm published by Niazy et al. (2005) (see also Sec. 2.3.2) is available as a plugin¹ for the widely used EEG processing tool kit EEGLAB² (Delorme & Makeig, 2004). EEGLAB is a program for Matlab³ and is free software (open-source) under the terms of the GNU General Public License (GPL)⁴. This permits the free distribution of the software as well as all modifications thereof, given its source code is included.

To execute the FMRIB plugin, the user is offered a dialog window with several parameters (see Fig. 3.1). Although the labels are descriptive, it is tedious and error prone when performing the algorithm multiple times. The actual algorithm is a Matlab function with up to 13 parameters to configure its behavior (see Lst. 3.1).

This Matlab function is written in one long piece (1106 lines)⁵. Only five external functions (apart from standard Matlab functions) are used. The main part is a loop over the EEG channels with a body of 470 lines performing the actual template generation and subtraction, PCA and ANC. Most variable names are shortened and used without a description. Of the total 1106 lines, only 169 use a comment of which only 60 are related to code documentation.

3.1.2 FARM Algorithm

For the FARM algorithm (van der Meer et al., 2010) no code is available. Although several EMailS were sent to the corresponding author, he didn't send an answer. Therefore only the descriptions as available in the article were used for the implementation of the algorithm.

¹<http://www.fmrib.ox.ac.uk/eeglab/fmribplugin/>

²<http://sccn.ucsd.edu/eeglab/>

³<http://www.mathworks.com/>

⁴<http://www.gnu.org/licenses/old-licenses/gpl-2.0.html>

⁵sometimes pejoratively denoted as “spaghetti code”, http://en.wikipedia.org/wiki/Spaghetti_code

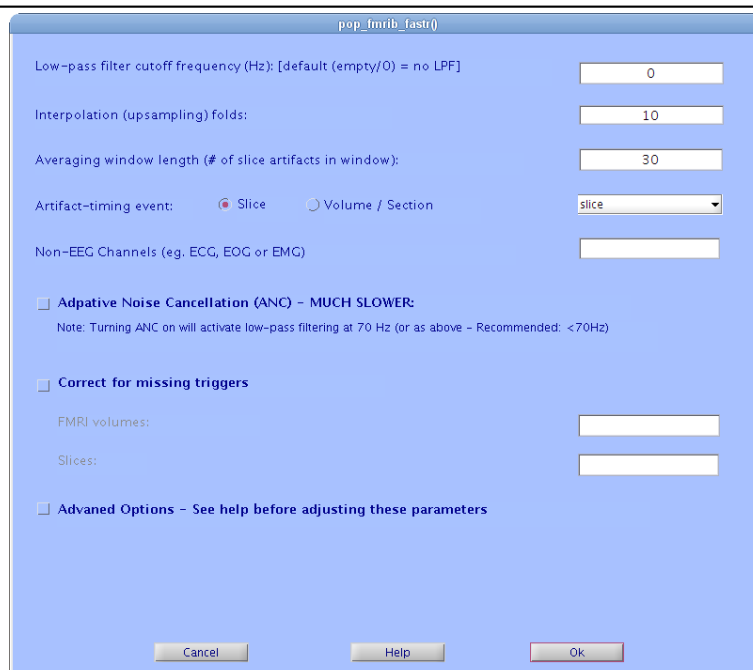


Figure 3.1: Screenshot of the FMRIB Plugin setup dialog.

3.2 Software Engineering

Software development is ideally performed in three steps: At the beginning the requirements are summarized as a specification. This is the starting point for the program implementation, which mainly involves programming. Finally, the implemented program needs to be validated to ensure meeting the specification and to sort out errors (Sommerville, 2004).

The final program is then deployed and set to operation. However, this is not the end of development: To remain useful, maintenance of the program has to be performed. This includes fault repair, adaption, and the addition or modification of functionality (Sommerville, 2004).

The task of this thesis includes such a software evolution process: The algorithm as provided by the FMRIB plugin has to be adapted and functionality has to be added. To start with, “[...] the process of system evolution involves understanding the program that has to be changed [...]” (Sommerville, 2004, p. 501). Ideally this should be supported by a full specification and foresighted planning with extensibility and maintainability in mind.

Listing 3.1: Section of the FMrib plugin implementing the FASTR algorithm (Niazy et al., 2005) from fmrib_fastr.m.

```
function EEG=fmrib_fastr(EEG,lpf,L>window,Trigs,strig,anc_chk,...
                        tc_chk,Volumes,Slices,varargin)
% ...
% EEG: EEGLAB data structure
% lpf: low-pass filter cutoff
% L: Interpolation folds
% window: length of averaging window in number of artifacts
% Trigs: An array of slice triggers locations.
% strig: 1 for slice triggers, 0 for volume / section triggers.
% anc_chk: 1 to do Adaptive noise cancellation
%          0 to not.
% tc_chk: 1 to correct for missing triggers, 0 for not
% Volumes: FMRI volumes for use in trigger correction
% Slices: FMRI Slices / Volume for use in trigger correction
% varargin{1}: relative position of slice trigger from beginning of
%              slice acquisition: 0 for exact start -> 1 for exact end
%              default=0.03;
% varargin{2}: Channels not to perform OBS on.
% varargin{3}: Numer of PCs to use in OBS. use 0 to skip this step.
%              'auto' or empty for auto order selection.
% ...
```

“However, many systems, especially older legacy systems [...], are difficult to understand and change. The programs may have been originally optimised for performance or space utilisation at the expense of understandability, [...]” (Sommerville, 2004, p. 501)

3.2.1 Reverse Engineering

As stated above, this also applies to the implementation of the FASTR correction algorithm (Niazy et al., 2005). Although their article is a well written specification of the algorithm, the actual implementation diverges at several points. Additionally, the source code itself is poorly documented, optimized for memory usage, and was not planned with maintainability in mind (compare Sec. 3.1.1).

Therefore, a prerequisite and first step was reverse-engineering the program (Sommerville, 2004). Its source code was analyzed to understand the func-

Check input and initialize parameters
Extract triggers and correct
Prepare internal variables and filters
Align slice triggers according to first channel
For every channel: Construct artifact and subtract
Up-sample data
Calculate average artifact and subtract
Calculate PCA of residuals and subtract
Down-sample data
Filter with low-pass
Adaptive noise cancellation
Print duration of execution

Figure 3.2: Structogram of the implementation of the FASTR algorithm (Niazy et al., 2005) in the EEGLAB FMRIB plugin.

tionality, the data (i.e., variables), and its organization. Figure 3.2 shows a structogram of the implementation of the FMRIB algorithm. In parallel, documentation was added to the code.

3.2.2 Software Re-Engineering

As a second step, the process of software re-engineering was utilized to increase the maintainability (Sommerville, 2004). This included the renaming of variables to more understandable names and improvements of the structure. Additionally, several simplification were performed, although at the expense of higher memory demand. In each of these cycles, special care was taken to keep the functionality and architecture unchanged by permanent validation and verification of the results.

3.2.3 Goals

In the course of software reverse-engineering and re-engineering, the algorithm of Niazy et al. (2005) and its implementation were understood. This established a basis to define the goals of the improved artifact correction algorithm.

The first goal is to build a universal and powerful toolbox, yet easy to use, with algorithms for the correction of gradient artifacts from EEG data recorded during fMRI acquisition.

As a second goal, this toolbox should be implemented using modern software design paradigms with understandability, maintainability and extensibility in mind.

Thirdly, the toolbox should provide an extensive set of utilities for data analysis, preparation, filtering and correction. These should include functionality as already published (Niazy et al., 2005, van der Meer et al., 2010, Allen et al., 2000, Moosmann et al., 2009 and others).

The fourth goal is to provide a mechanism to use a flexible combination of these utilities. This should still be executed in an automated process to minimize user interaction and to maximize reproducibility of the results.

Fifth, and most important, the toolbox should be demonstrated by implementing an improved algorithm which gives better results than established algorithms like Niazy et al. (2005).

Therefore, as a sixth goal, the toolbox should include an evaluation framework which allows to analyze the results of the correction algorithm using multiple performance indicators (see Sec. 2.4).

Finally, the toolbox should be released as free software under the terms of the GNU General Public License⁶ for public download.

3.2.4 Generalization

The generalized scheme for artifact reduction algorithms proposed in Sec. 2.3 and Fig. 2.6 is repeated here for reference (see Fig. 3.3). Reverse-engineering the source code of the FMRIB plugin revealed a structure very similar to the generalized scheme (see Fig. 3.2). The algorithm by van der Meer et al. (2010) also fits in this scheme, although no source code was available.

While Niazy et al. (2005) interpolates the EEG data by a default factor of 10 and corrects the slice trigger markers to the finer temporal resolution, van der Meer et al. (2010) use a temporal shift of every slice period with a sub-sample resolution. These *pre-processing* steps are introduced to avoid inaccuracies and thus residual artifacts in the following template subtraction step.

⁶<http://www.gnu.org/licenses/old-licenses/gpl-2.0.html>

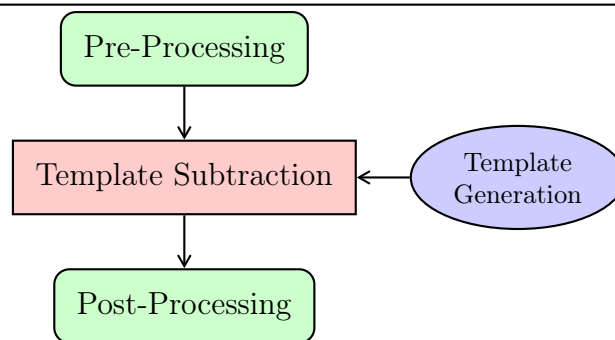


Figure 3.3: General approach of the artifact correction algorithms.

The *template generation* step of Niaz et al. (2005) implements nested loops to average n epochs before and after the current epoch, with only every second epoch included (i.e. sliding window). On the other hand, van der Meer et al. (2010) use a subset of n epochs of a larger number surrounding the current epoch which have the highest similarity to the current epoch (i.e. best candidates).

Niaz et al. (2005) and van der Meer et al. (2010) use a very similar *post-processing* with PCA and ANC. Additionally, van der Meer et al. (2010) fill the volume gaps with synthesized data.

3.3 Object-Oriented Design

The process of software re-engineering includes source code translation. This involves the conversion to a more modern version and design paradigm of the programming language (Sommerville, 2004).

The implementation of the FMRIB plugin utilizes a procedural design paradigm, where all functionality is divided into self-contained sub-routines. The processed data is supplied as input parameters and returned as output parameters. This architecture was re-engineered to the *object-oriented design paradigm* (Sommerville, 2004). This paradigm was selected to utilize its specific advantages of data encapsulation, maintainability and extensibility.

3.3.1 Object-Oriented Design Paradigm

“An object is an entity that has a state and a defined set of operations that operate on that state.” (Sommerville, 2004, p. 316). In other words, an

object is a container, which stores all parameters and data (“state”). Additionally it has associated methods, which perform operations on that object, i.e. on its parameters and data. While the word “object” denotes an actual instance, the definition of its data (also called “fields”) and its methods is specified by the so called “class”.

During design specification the classes and their relationships are visualized using the Unified Modeling Language (UML) class diagrams (Sommerville, 2004, p. 316). Every class is drawn as a rectangle with the class name in the top portion. This is followed by the fields and the methods, which are annotated to express their visibility (i.e. the access permissions like private, public, ...). Inheritance, instantiation and all other relationships are denoted by arrows with defined tips and labels.

Although **Matlab** itself is a procedural language, the support for object oriented programming was introduced with version 7.6 (R2008a). Differing names are used for fields, which are termed “properties”.

3.3.2 Software Design

For the artifact correction toolbox, no advantageous points were identified to split the data and/or functionality into multiple classes. Therefore a single class “FACET” was created to hold all parameters and data. Its methods operate on this data to perform the artifact correction. Besides the data encapsulation, no other object oriented concepts like inheritance and polymorphism are used. Figure 3.4 shows the UML class diagram.

Public member fields for parameters and the EEG data are placed in the class. These have to be set by the user after instantiation of the class. For some of these fields, setter methods are used to extract derived values from the assigned parameters. These are stored to member fields with public read-only accessibility.

Keeping the EEG data (which by far requires the largest amount of memory) inside the object as a member variable also improves memory management. In contrast, Niazy et al. (2005) used functions and handed over the EEG data as function parameter and return value. In this case, **Matlab** creates a copy of the data every time. In the object-oriented approach, all methods work on the object member variables, therefore no copy is performed. This leads to reduced memory requirements and faster execution.

Several public methods are provided to analyze the data and remove the artifact. First of all, the constructor `FACET()` creates a new instance of the

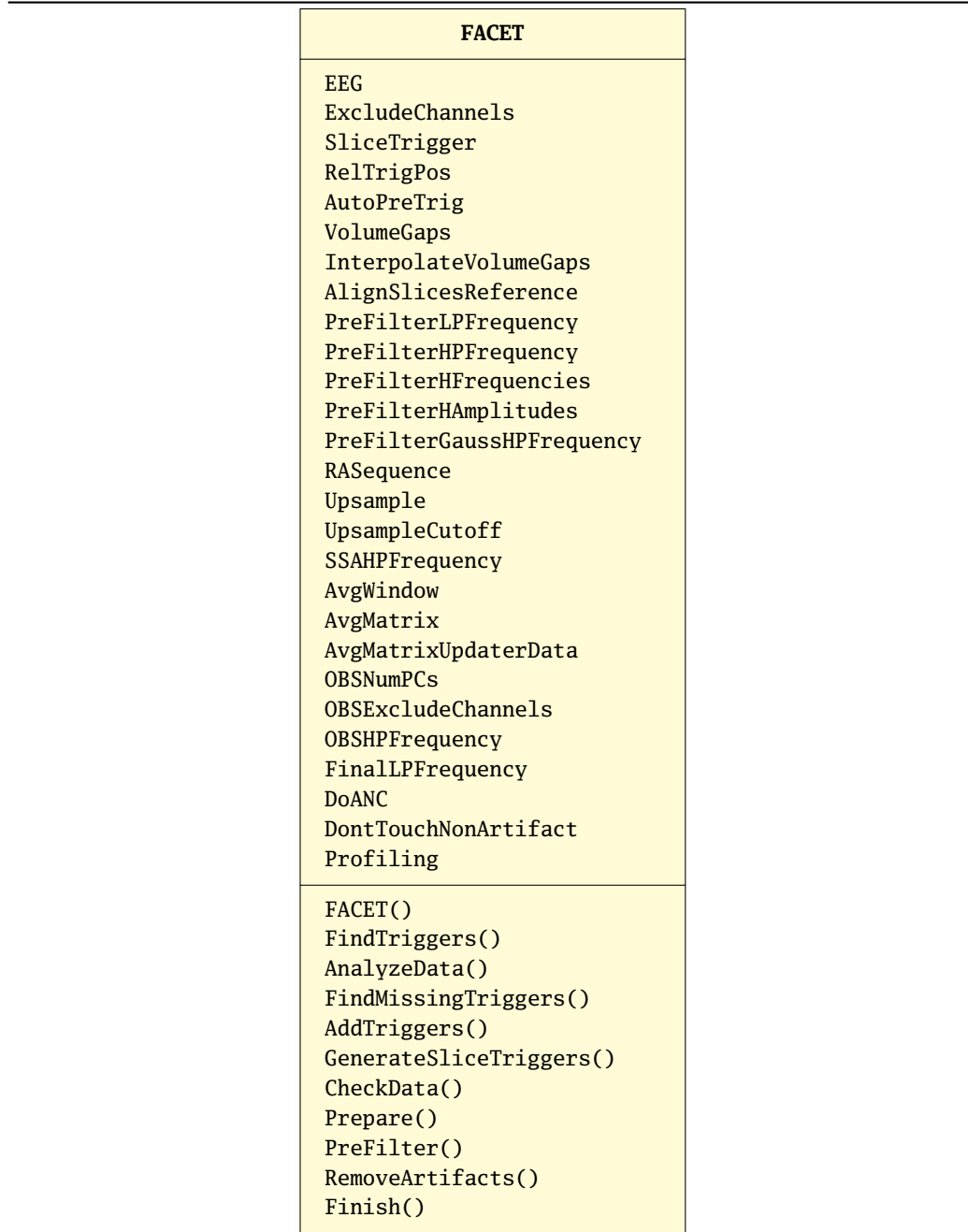


Figure 3.4: Class diagram of the FACET base class of the artifact correction toolbox. Only the public fields and methods are shown and the method parameters and return values are omitted.

class. Other methods are used to identify (and optionally correct) trigger events and to print an analysis of the EEG data. Finally, the core algorithm is performed by executing its associated methods.

The internal working is split into multiple private and protected methods. Additionally, events are issued at important points of execution to notify any interested programs. This allows, e.g., to modify the data or to print progress reports during the algorithm execution.

Visual output. The central class **FACET** silently performs the algorithm and does not print anything to the screen. The above mentioned events are used by the derived class **FACET_Text**, which inherits from **FACET** (see Fig. 3.5). It registers listeners to every event and prints a short message for every notification.

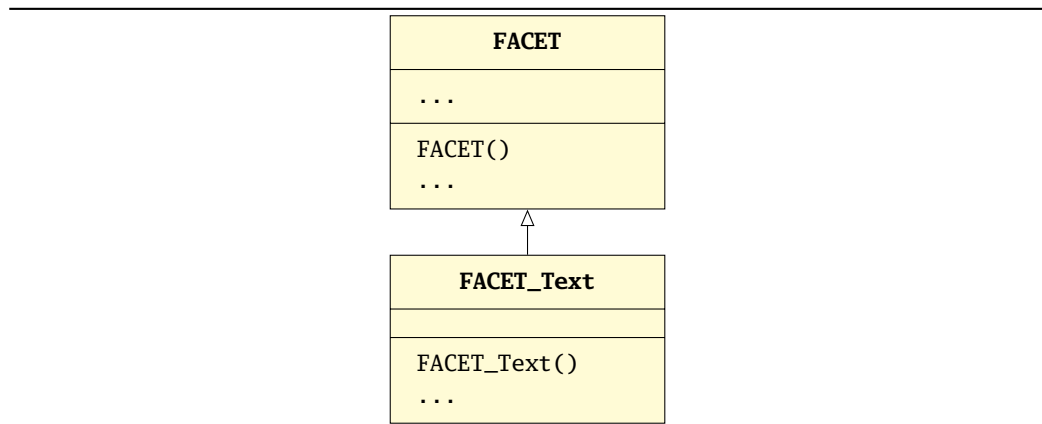


Figure 3.5: Class diagram of the **FACET_Text** class, which prints a textual progress report of the artifact correction algorithm.

Package. All classes (including the evaluation framework, see Sec. 3.11) are put together in the **Matlab** package **FACET** (note: it has the same name as the class of the correction toolbox).

3.3.3 Algorithm Setup

The original FASTR algorithm was configured with a graphical dialog (see Fig. 3.1). As stated above, for multiple invocations of the algorithm, this is tedious and error prone. The dialog is a front-end for the **Matlab** function **fmrrib_fastr()**, which is called with up to 13 input parameters (see Lst. 3.1). This can be directly called by the user and therefore guarantee

identical settings for multiple invocations. On the other hand, there is no direct possibility to document and to justify the chosen values.

A configuration file is an alternative to the dialog and to the direct command entry. The user sets options and parameters for the algorithm before it is executed. It should allow user comments, so that he can put notes on the entered information like description of the configuration values and rationale for decisions. Therefore, a configuration file guarantees reproducible and documented results.

Using the object-oriented paradigm and employing **Matlab** itself as a scripting language enables the setup of the algorithm in exactly this way. Instead of a pure configuration file, a **Matlab** script or function is used. It can be documented with comments to the users desire. The configuration values are assigned to public properties of the **FACET** object. Here the full power of **Matlab** is available to determine the value, either as a direct value, or calculated with user-defined formulas and even functions.

3.3.4 Application Example

The algorithm setup and execution should be demonstrated by an example. The toolbox provides several examples in the files **CleanEx1.m** to **CleanEx6.m** (short for “cleaning example number 1–6”) which will be used in excerpts throughout this work to demonstrate the features of the toolbox. The example **CleanEx1.m** uses the FMRIB dataset (see Sec. 4.1.1) and is given in extracts in Lst. 3.2.

For easier execution of the example, it is wrapped in a **Matlab** function which accepts the raw EEG data in an **EEGLAB** dataset structure as an input parameter (line 4) and returns the cleaned data (line 33). This function is executed with

```
cleaned = CleanEx1(EEG_FMRIB);
```

where the variable **EEG_FMRIB** holds the FMRIB data set.

As first step, a **FACET_Text** object is instantiated (line 7) by executing the class constructor. The next step is to assign the raw EEG data to the public property **EEG** (line 11). Note that this property internally is implemented with a setter method. This automatically checks for the proper data format and extracts the number of channels and other values. In lines 15 and 18 two assignments of configuration values are shown. In the first case a direct value is assigned while the second case shows a formula using another configuration value. Actually, any **Matlab** construct can be used.

Listing 3.2: Cleaning Example 1 from CleanEx1.m.

```

1 % Cleaning example 1
2 % Note: This only works with the EEG dataset supplied by Niazy with the
3 % EEGLAB plugin.
4 function EEGout = CleanEx1(EEGin)
5
6     %%% Create object
7     E = FACET.FACET_Text();
8
9     %%% Set Input Parameters
10    %%% EEGLAB EEG data structure
11    E.EEG = EEGin;
12    ...
13    %%% Averaging of artifacts
14    % Length of averaging window in number of artifacts
15    E.AvgWindow = 30;
16    ...
17    % calculate AvgMatrix for every channel separately, ...
18    E.AvgMatrixUpdaterData.SearchHalfWindow = 3*E.HalfWindow;
19    ...
20    % Analyze EEG dataset and print information.
21    E.AnalyzeData;
22    ...
23    %%% Perform Artifact Removal
24    E.Prepare;
25
26    E.PreFilter;
27
28    E.RemoveArtifacts;
29
30    E.Finish;
31
32    %%% Return parameters
33    EEGout = E.EEG;
34
35 end

```

The first method called is `AnalyzeData()` in line 21, which prints information about the EEG data to the screen (see Sec. 3.4.1). Execution of the actual artifact removal algorithm is invoked in lines 23–30. `Prepare()` derives some further internal variables from the setup configuration values. Then a filter (e.g. a high-pass, see Sec. 3.5) is applied to the EEG data using `PreFilter()`. This is a part of the pre-processing step shown in Fig. 3.3. The main part of the correction algorithm is encapsulated in `RemoveArtifacts()`. It internally iterates over all EEG channels for which further pre-processing steps, template generation, template subtraction and post-processing are performed. The method `Finish()` simply stops the run-time counter and executes a final

event notification. Finally, the cleaned EEG in the property `EEG` is returned to the caller (line 33).

3.4 Data Analysis and Preparation

Although the user of the developed artifact correction algorithm usually is informed about the parameters of EEG and fMRI acquisition, methods are provided to analyze the EEG data to find problems, but also to find more detailed information. As a first step to prepare the execution of the artifact correction algorithm, the time instances of fMRI volume or slice acquisition have to be determined with a dedicated method. Two methods are provided to correct missing triggers, automatically and manually. An additional method helps to convert volume triggers to slice triggers. Finally, before the correction can start, all settings should be checked for completeness and sanity using a dedicated method.

3.4.1 `AnalyzeData()`: Analyze EEG Dataset and Setup

The method `AnalyzeData()` provides functionality to characterize the EEG dataset and display information about it (see Lst. 3.3). It prints the number of samples, sampling rate and the resulting duration of the recording. The number of channels and a list of all channel labels is printed.

In the `EEGLAB` dataset structure, a list of events (triggers) is stored, each with a name and an according latency (= index of corresponding sample). This data indicates, e.g., the begin of every slice acquisition, volume acquisition, the subject's heart beat or stimulus onset. The function `AnalyzeData()` prints a list of all event names which occur in the `EEGLAB` Dataset and shows their frequency.

The next step of data analysis estimates the begin and end of the fMRI acquisition during the EEG recording. Its duration as well as the duration of unimpaired EEG data before and after the fMRI acquisition are shown.

If the function `FindTriggers()` (see Sec. 3.4.2) was already executed, additional information is displayed. A histogram of the distances between successive triggers is shown and used to warn, if triggers are missing. These can be completed with the function `FindMissingTriggers()` (see Sec. 3.4.3). It is also checked if the number of triggers is enough for the duration of

Listing 3.3: Exemplary output of `AnalyzeData()` for the FMRIB dataset.

```

Samples:          332416
Sampling Rate: 2048
Duration:         162.3125s (2 minutes 42.3 seconds)
Channels:         32
    1-10: Fp1 Fp2 F7 F3 Fz F4 F8 T3 C3 Cz
    11-20: C4 T4 T5 P3 Pz P4 T6 O1 O2 AF4
    21-30: AF3 FC2 FC1 CP1 CP2 P03 P04 FC6 FC5 CP5
    31-32: EMG ECG
Events:
    'slice'      840x
Acquisition
    approx. begin:      58883 ( 28.75s)
    approx. end:        304491 ( 148.68s)
    approx. duration:   245609 ( 119.93s)
Non-Acquisition
    approx. before:     58882 ( 28.75s)
    approx. after:      27924 ( 13.63s)
    approx. total:      86806 ( 42.39s)
Trigger Distances Histogram
    292 (142.58ms):    707x #####
    293 (143.07ms):    93x #####
    302 (147.46ms):    28x ##
    303 (147.95ms):    11x #
Mean trigger distances 142.87ms are less than 1.0s, assuming SLICE triggers.
Found 800 smaller (slice) distances of 142.63ms and 39 larger (volume)
distances of 147.60ms, with a volume gap of 4.96ms.
This most probably shows an fMRI acquisition of 40 volumes with 21 slices
each, 840 in total.

```

fMRI acquisition. Missing triggers can be added manually using the function `AddTriggers()` (see Sec. 3.4.4).

If the mean distance between the triggers is below 1.0 s, it is assumed that they denote slice acquisition, otherwise volume acquisition is assumed. For slice triggers, an analysis for volume gaps (see Sec. 3.7) is performed and an estimate of total volume and slice count is printed. If volume triggers are assumed, the function estimates the slice period by finding maxima in the auto-correlation function of one volume interval. The acquired information can be used for `GenerateSliceTriggers()` (see Sec. 3.4.5) to convert the volume triggers to slice triggers.

3.4.2 FindTriggers(): Get Trigger Latencies

As mentioned above, the EEGLAB dataset contains a list of trigger events, each characterized by a name and a latency value. The method `FindTriggers()` filters the events with a given name and stores a list of all latency values in a member variable. The function should be used to select the triggers for slice or volume fMRI acquisition onset. The latency values are used by the template generation and subtraction steps (compare Fig. 3.3).

3.4.3 FindMissingTriggers(): Automatically Correct Missing Triggers

In some datasets the list of triggers misses one or more events. The method `FindMissingTriggers()` is used for the automatic correction of these missing trigger events. It scans the list of triggers, which was previously setup by `FindTriggers()`, for too large distances and inserts a trigger. Care is taken to handle volume gaps correctly.

3.4.4 AddTriggers(): Manually Correct Missing Triggers

The method `FindMissingTriggers()` can only handle missing triggers between other triggers, but not before the first or after the last event. These missing triggers can be added manually using the method `AddTriggers()`.

The example program `CleanEx3.m` uses a dataset, which requires to add two triggers at the beginning. Listing 3.4 shows how to use `AddTriggers()` to add these triggers at -1 and -2 times the mean trigger distance before the first trigger.

Listing 3.4: Usage of `AddTriggers()` from `CleanEx3.m`.

```
% Add triggers outside of defined trigger range
E.AddTriggers([-2 -1] * mean(diff(E.Triggers)) + E.Triggers(1));
```

3.4.5 GenerateSliceTriggers(): Convert Volume to Slice Triggers

If the EEG data was recorded with triggers for the onset of every fMRI volume but without information on the slice onset, the method `Generate-`

`SliceTriggers()` aids in the calculation of the according slice triggers. It creates a list of triggers from the number of slices per volumes, the duration of every slice acquisition and the relative position of the slice acquisition within the volume acquisition.

3.4.6 CheckData(): Test Data and Setup

Finally, before the actual artifact correction algorithm is started, it is advisable to check the data and the setup for notable or problematic conditions. This is performed by the method `CheckData()`. The current implementation checks that EEG data is provided and that triggers were setup. Future extensions are planned to check filter properties for sensible values and certain interdependencies of the settings.

3.5 Pre-Filter

Many EEG recordings during fMRI acquisition contain slow fluctuations of the baseline, including the FMRI dataset (see Fig. 3.6). These are highly irregular and last for several seconds which means a frequency considerably below 1 Hz.

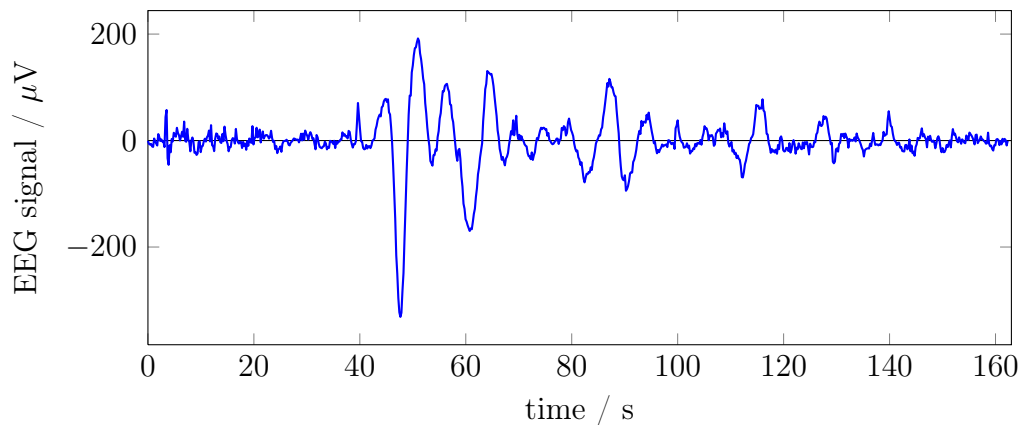


Figure 3.6: Slow fluctuations of the baseline in the FMRI dataset after correction with the algorithm by [Niazy et al. \(2005\)](#) (note the time scale).

3.5.1 Slow Fluctuations

These slow fluctuations cause an unpredictable offset between the short slice epochs as well as a (nearly) linear trend of their baseline. Subtracting the mean value from the whole EEG signal or from every slice therefore does not solve the problem. It can only be tackled with a high-pass filter with a very low cut-off frequency.

3.5.2 High-Pass Filter Implementations

During the development of the artifact correction algorithm, three different implementations of this high-pass filter were investigated.

- FIR (finite impulse response) filter
- Ideal filter in frequency domain
- Gaussian filter

A fourth filter type, namely IIR (infinite impulse response) filters, were not investigated because of the difficult design and adoption to the unknown sampling rate of the processed EEG data as well as possible stability problems.

FIR filter. To realize a high attenuation in the narrow frequency band from 0 Hz to the cut-off frequency, a very high number of filter coefficients is necessary (1000 were used). This results in high demand of processing power. Additionally, the steep characteristic resulted in large overshoot of the transfer function, which contributed signal distortion effects.

Ideal filter in frequency domain. Due to the problems to realize a high attenuation in the stop band using a FIR filter, another approach was investigated. While FIR filters work in the time domain, the frequency domain can be used to implement an ideal filter. This allows arbitrary modification of the amplitude of the frequency domain values of the signal. In the case of an ideal high-pass filter, all amplitude values below the cut-off frequency are set to 0.0.

This approach gives best attenuation, but results in severe ringing and oscillations after the inverse Fourier transform of the signal to time domain (Oppenheim et al., 1997). This is a direct consequence of the time domain signal corresponding to a rectangular frequency response

$$H(j\omega) = \begin{cases} 1 & |\omega| \leq \omega_c \\ 0 & |\omega| > \omega_c \end{cases} \quad \bullet \text{---} \circ \quad x(t) = \frac{\omega_c}{\pi} \frac{\sin(\omega_c t)}{\omega_c t}$$

which is a weakly attenuating ($1/x$) oscillation with the cut-off frequency ω_c .

The Fourier transform to convert the EEG data from time domain to frequency domain and back is an overhead required to apply the filter in frequency domain. However, using an FFT and iFFT for these operations, leads to a dramatic *reduction* of the runtime of the filter compared to the high-order FIR filter used before.

Gaussian filter. The maximum edge steepness of the frequency response without overshoot is provided by Gaussian filters⁷ (Rappaport, 2001). The shape of the impulse response as well as the transfer function are Gaussian functions.

Although Matlab provides a function to design a Gaussian FIR filter (`gaussfir`), the implemented algorithm uses a frequency domain filter because of its higher processing speed. Due to the differences in the mean value (i.e., DC value) of the three sections of the EEG signal (before, during and after fMRI acquisition), the filter is applied separately.

3.5.3 Low-Pass Pre-Filter

Allen et al. (2000) applied a low-pass filter with a cut-off frequency of 50 Hz to the EEG data to remove the fMRI gradient artifacts. The result still had large artifact amplitudes, because the base frequency of both, the volume and slice acquisition, are well below 50 Hz (see Sec. 2.2.2). Therefore, a low-pass alone is not enough to remove the artifacts.

On the other hand, can a low-pass pre-filter *support* the artifact removal algorithm, so that the final signal contains less residual artifact? The low-pass filter strongly attenuates the harmonics of the volume and slice periods. This leads to temporal jitter of the low frequency components of the artifact signal. The artifact template generation routines are severely impaired by this jitter which results in large residual artifacts after template subtraction. To summarize, the final signal posed more residual artifacts in this case. Therefore the low-pass pre-filter is not activated.

⁷<http://de.wikipedia.org/wiki/Gau%C3%9F-Filter>

3.6 Sub-Sample Alignment

As mentioned earlier, the main part of the algorithm is the template subtraction (comp. Fig. 3.3). The templates are generated using an average of slice or volume epochs. Before this averaging step can be performed, it is advisable to further reduce sources of uncertainties.

3.6.1 Problem

In most cases the fMRI scanner and the EEG recording use separate clocks and do not utilize synchronization. This means that, in general, every period of the MR gradient artifact is sampled by the EEG recording system with a varying temporal offset. This leads to differences in the EEG values of every fMRI period (see Fig. 3.7). Calculating an average of successive periods (i.e., epochs) leads to substantial error and thus residual artifact.

To cope with this problem, several methods were used (see Sec. 2.3.1). Niaz et al. (2005) increases the sampling rate by interpolating the data by a factor of 10 (step “Up-sample data” in Fig. 3.2) and aligning the triggers within this finer temporal quantization. This reduces the residual amplitudes, but at steep slopes even a short uncertainty leads to large vertical differences.

3.6.2 Time-Shift with Sub-Sample Resolution

Further increasing the sampling rate (by up-sampling the data) helps to reduce the error, but also increases memory and processing demands. A different approach uses a time-shift of the data with a sub-sample resolution (van der Meer et al., 2010). The time shifting property of the Fourier transform is utilized (Oppenheim et al., 1997). As a first step the EEG signal is converted to frequency domain using the FFT. Then a linear phase is added, depending on the desired sub-sample time-shift, before it is transformed back to time domain using the inverse FFT.

Since the necessary temporal shift is unknown, this work implements an iterative optimization algorithm. It minimizes the least square error of the current epoch to a (configurable) reference epoch using the bisection method.

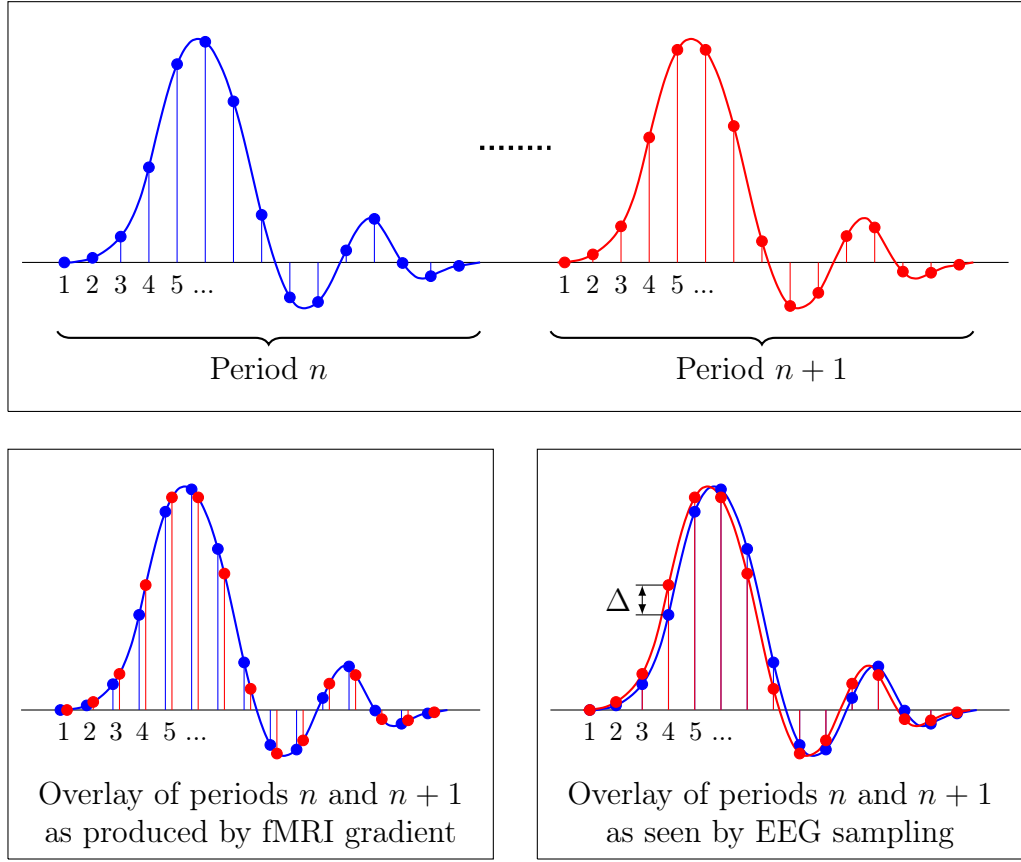


Figure 3.7: Sampling by the EEG recording is not synchronized with the fMRI gradient signal. Successive periods of the fMRI gradient signal are sampled by the EEG recording system with a varying temporal offset (top graph). Period n is drawn in blue and the following period $n + 1$ in red. The bottom left graph shows these fMRI periods overlayed as sampled by the EEG recorder during period n (blue stems) and period $n + 1$ (red stems). Overlaying the EEG samples at the quantized sampling times therefore leads to a vertical difference Δ for every period as denoted in the bottom right graph.

3.6.3 Interpolation Error

The interpolation performed using the **Matlab** function `interp` in the FMRIB plugin (Niazy et al., 2005) sets the relative cut-off frequency parameter for the interpolation filter to 1.0. This leads to deviation of the up-sampled signal from the smooth signal between the original samples (see Fig. 3.8). The default relative cut-off frequency of 0.5 results in a smooth signal. Therefore this value is implemented with a configurable property which defaults to 0.5.

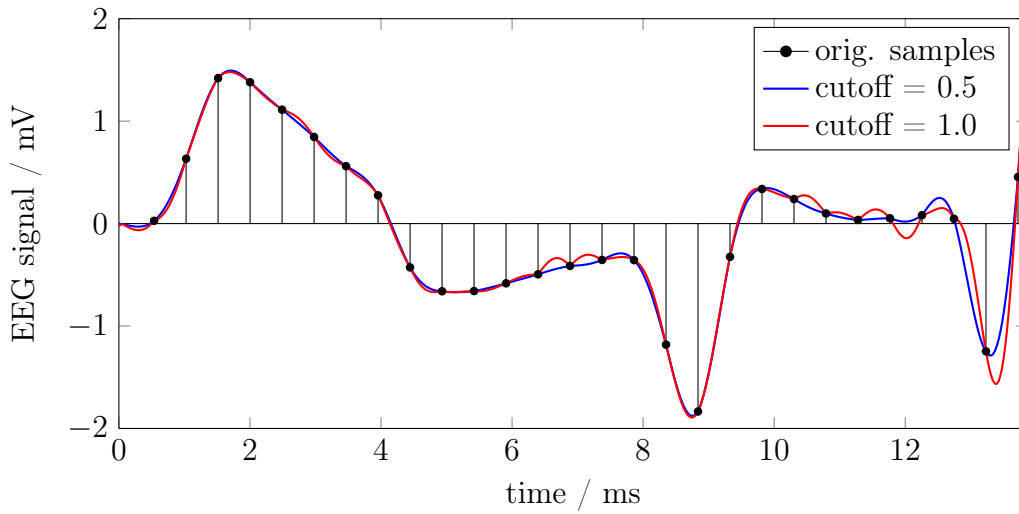


Figure 3.8: Setting the cut-off frequency parameter of Matlab's `interp` function to 1.0 results in deviations of the up-sampled data (red curve) from the smooth signal (blue curve) between the original samples (black stems).

3.7 Volume Artifact

The fMRI acquisition is performed volume by volume, therefore it shows a main period of the volume acquisition. For every volume a number of slices are acquired which pose a sub-period. Two cases for the relationship of slice and volume timing are possible: The time of a volume acquisition is an exact integer multiple of the time of the slice acquisition. This means that after the acquisition of the last slice the fMRI scanner immediately continues with the acquisition of the first slice of the following volume. The second, more general, case exists if the acquisition of all slices lasts shorter than the repetition time of the volume acquisition. This results in a (short) delay between the acquisition of the last slice until the next volume starts with the acquisition of its first slice.

3.7.1 Problem

For example, the FMRI dataset was recorded while 40 volumes with 21 slices each were acquired by the MR scanner. The volume repetition time is 3000 ms, while the slice period is 142.62 ms. This leads to a volume gap of 5 ms.

An optimization algorithm was developed by [van der Meer et al. \(2010\)](#) to determine the slice period $sdur$ and the volume gap $dtime$. They report $sdur = 56.855$ ms and $dtime = 11.723$ ms for the employed fMRI EPI sequence, which recorded 150 volumes of 45 slices each within a total time of 384 s.

During this volume acquisition gap, an additional gradient artifact was recorded. Additionally, the artifact extended to the surrounding slice periods (see Fig. 3.9). This means that these slice periods have to be corrected with an additional method. The volume gap was replaced with synthesized data.

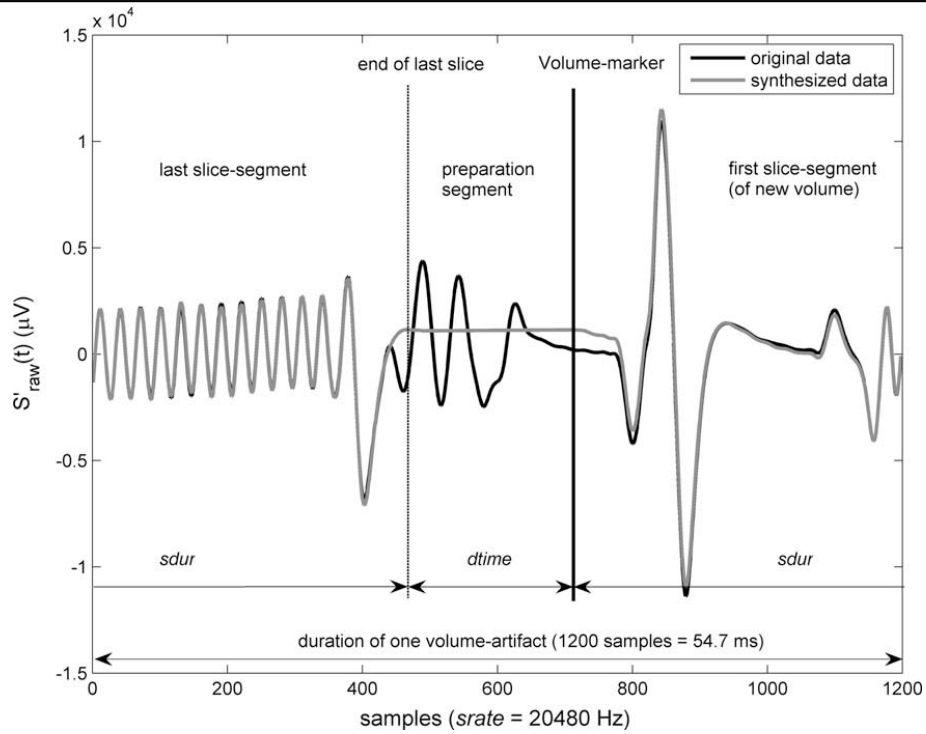


Figure 3.9: Volume artifact during volume gap (preparation segment) and extending to the surrounding slice periods (from Fig. 6 on p. 771 in [van der Meer et al., 2010](#)).

3.7.2 Correction of the Volume Artifact

The algorithm implemented in this work is similar to that of [van der Meer et al. \(2010\)](#). Assume an fMRI acquisition with n_v volumes of n_s slices each, i.e. a total of $n_v \cdot n_s = n_e$ slices. For every slice the time of its onset is given by t_e (with the epoch index $e = 1, \dots, n_e$). Due to the double periods, the epoch index can be expressed by the volume index $v = 1, \dots, n_v$ and slice

index $s = 1, \dots, n_s$ as $e = (v-1) \cdot n_s + (s-1) + 1$ ⁸. This enables to write the trigger events $t_e = t_{v,s}$. With this notation, the volume gap exists between the last slice $s = n_s$ of each volume v at t_{v,n_s} and the first slice $s = 1$ of the following volume $v+1$ at $t_{v+1,1}$.

In a first step, the positions of the $n_v - 1$ volume gaps is determined by investigating the distances between the slice trigger events t_e , utilizing the fact that

$$t_{v+1,1} - t_{v,n_s} > t_{v,s+1} - t_{v,s} \quad \forall v = 1, \dots, n_v - 1 \text{ and } s = 1, \dots, n_s - 1.$$

As a second step, the volume artifact, which extends to the slice periods right next to the volume gap at t_{v,n_s} and $t_{v+1,1}$, is calculated. For this purpose the five slice epochs t_{v,n_s-4} to t_{v,n_s} before the volume gap and the five slice epochs $t_{v+1,1}$ to $t_{v+1,5}$ after the volume gap are averaged and subtracted from the adjacent slice periods at t_{v,n_s} and $t_{v+1,1}$, respectively.

These volume artifact templates are weighted with a logistic function

$$w_x = \frac{1}{1 + e^{\alpha(x-x_0)}}$$

to emphasize the artifact near the volume gap and de-emphasize it farther away. The parameters α and x_0 are chosen to give a 50 % weight at 80 % of the slice interval, 10 % at 69 % of the interval and 1 % at 57 % of the interval. The weighted templates are then subtracted from the adjacent slice epochs.

In a final step, the gap is filled with a linear function from the end of the last slice t_{v,n_s} to the begin of first slice of the next volume $t_{v+1,1}$.

3.8 Averaging Matrix

The template generation step as outlined in Sec. 3.2.4 and Fig. 3.3 usually calculates the average of surrounding artifact epochs. Depending on the exact algorithm, different epochs are selected for averaging.

3.8.1 Generalization

The selection of epochs and calculation of the average value is usually implemented using a loop which iterates over the epochs from a start to the end

⁸ -1 for v and s as well as +1 for the whole formula are necessary because the indices start at 1

index value. A generalized approach uses a square matrix with the size equal the number of epochs where the row and column indices correspond to the epochs (Moosmann et al., 2009).

Figure 3.10 shows a visual representation of such a matrix. Every element is represented by a square. Its gray shade shows the value: white squares represent the value 0.0, dark squares indicate the value 1.0. Every row (y -coordinate, top to bottom) shows by the value of its columns (x -coordinate, left to right) which epochs are averaged to build the template for the epoch corresponding to this row.

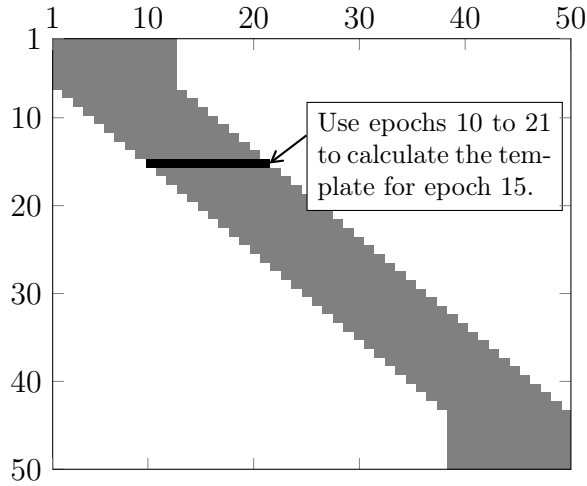


Figure 3.10: Visual representation of an averaging matrix for 50 epochs. White squares represent 0.0, dark squares 1.0.

By populating the matrix with the appropriate numbers, any averaging algorithm can be described. It is even possible to include weights, e.g. to enhance epochs near the current one while attenuating epochs further away. Therefore, any *linear combination* of the epochs is possible.

Using a matrix to describe the averaging process poses another advantage: The averaging can be performed with a single matrix multiplication. Highly optimized implementations of this operation are available. Therefore a speed improvement is expected. Let the raw EEG data of one channel be stored in the row vector d_i with $i = 1, \dots, n$, where n is the total number of samples of the EEG recording. This vector is wrapped to the data matrix $\mathbf{D} = (d_{e,j})$, where each row $e = 1, \dots, n_e$ is one of the n_e epochs and $j = 1, \dots, n_l$ is the sample index within each epoch of length n_l ($n_e \cdot n_l = n$).

The averaging matrix $\mathbf{A} = (a_{e,f})$ is a $n_e \times n_e$ square matrix, where the columns f of every row e specify which epochs f are averaged (see above). The multiplication with the data matrix \mathbf{D}

$$\mathbf{N} = \mathbf{A} \mathbf{D} \quad (3.1)$$

results in the noise (artifact) matrix $\mathbf{N} = (n_{e,j})$ with the same dimensions as \mathbf{D} . Every value $n_{e,j}$ is given by the equation

$$n_{e,j} = \sum_{k=1}^{n_e} a_{e,k} d_{k,j}. \quad (3.2)$$

For every sample j of the epoch e , all epochs $k = 1, \dots, n_e$ of $d_{k,j}$, multiplied by the averaging matrix element $a_{e,k}$, are summed.

The final step is to wrap back the noise matrix \mathbf{N} to a row vector like d_i . Note that if the fMRI acquisition poses volume gaps (compare Sec. 3.7), the estimated noise during these intervals is unknown. Two approaches are implemented by the artifact correction algorithm and setup with a configuration parameter. One method sets the noise values in the volume gaps to 0.0. The other method fills the gap with a linear function from the end of the last slice to the begin of first slice of the next volume, i.e., interpolated values are used. In contrast to the volume artifact correction detailed in Sec. 3.7 this interpolation is performed on the estimated noise data during template generation instead of the EEG input data during pre-processing.

The averaging matrix provides a simple mean to calculate the templates in the template generation step (compare Fig. 3.3). The matrix clearly shows which epochs are used for the templates. It is a general and yet complete interface to specify an arbitrary template algorithm.

3.8.2 Implementation

In the process of software re-engineering the legacy averaging algorithm was replaced by a matrix based algorithm. Due to the simple matrix multiplication, the whole averaging is performed by a single **Matlab** operation. Numerous methods for the generation of the matrix to reflect specific averaging algorithms were implemented and added to the **FACET** package. Section 3.10.1 provides details on the usage of these methods.

- Block-wise processing (Allen et al., 2000)
- Averaging according to Niazy et al. (2005)

- Realignment-Parameter Informed Algorithm ([Moosmann et al., 2009](#))
- Corresponding slices of every volume
- Best fit according to [van der Meer et al. \(2010\)](#)

As the matrix usually contains many zeros, it can be implemented as a sparse matrix. This considerably reduces the memory consumption and processing time for a high number of epochs.

3.9 Low-Pass Filter

As mentioned by [Allen et al. \(2000\)](#) (see Sec. 2.2.2), a low-pass filter as the only algorithm to reduce the artifacts does not suffice. On the other hand, it greatly improves the result as a post-processing step ([Niazy et al., 2005](#), see Sec. 2.3.2). Therefore the toolbox provides the feature to apply a low-pass filter with a configurable cut-off frequency.

As the filter is a post-processing step, it is only applied to the processed data, i.e., to the period with artifacts from fMRI acquisition, and not to the unimpaired EEG data before and after the fMRI acquisition. The result is visualized in the left spectrogram in Fig. 3.11. This leaves high-frequency components in the EEG outside of the fMRI acquisition. Therefore the filter optionally can be applied to these periods too (see right spectrogram in Fig. 3.11).

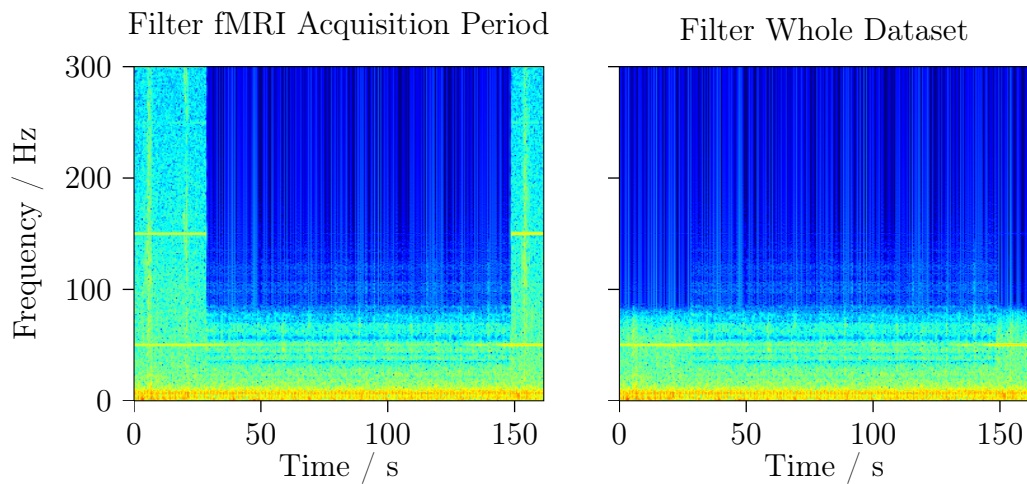


Figure 3.11: Apply a low-pass as post-processing step to the cleaned EEG during fMRI acquisition or to the whole EEG acquisition (the hotter the color the more activity).

3.10 Algorithm Sequence

All investigated algorithms, especially those of [Niazy et al. \(2005\)](#) and [van der Meer et al. \(2010\)](#), which are used as basis for this work, implement the individual steps in a fixed order (compare Fig. 3.2). Depending on the EEG dataset, which should be corrected, not every step is necessarily required. On the other hand, additional steps or innovative combinations of present steps can contribute to an improvement of the results. For example, the template subtraction can be performed twice with different methods for the template generation. Therefore the presented algorithm provides the ability to customize the sequence of individual artifact removal steps.

3.10.1 Customization of Sequence

The artifact correction algorithm was split into multiple blocks with a common interface for the input and output data. This allows these blocks to be combined flexibly and setup in an arbitrary order. Each block is implemented as a method of the **FACET** class. It operates on object member variables, which represent the EEG data (in successively improved quality) as well as the (reconstructed) artifact data. Using the usually large amount of data as a common (member) variable avoids the copy operation for the call of every function, which would be required in a pure procedural design paradigm (compare Sec. 3.3.2).

To configure which blocks are executed, the member variable **RASquence** is set to an array⁹ of strings (see Lst. 3.5). Each string specifies a corresponding block of the algorithm. These blocks are executed in exactly the given order. Additionally, user-defined functions can be included (note the entry **@FACET.AvgArtWghtFARM**), which are executed as well.

The use-case in the given example is to specify the method to create the averaging matrix for the template generation individually for every channel before it is used by the next step **CalcAvgArt** (see Sec. 3.8). The member variable **AvgMatrixUpdaterData** is provided for this case to supply configuration data to this function (compare line 18 in Lst. 3.2).

Two functions for adaptively calculating the averaging matrix depending on the EEG data are provided: **@FACET.AvgArtWghtFARM** uses the best matching slice periods within a given window as proposed by [van der Meer et al. \(2010\)](#) and **@FACET.AvgArtWghtAllen** provides the functionality as implemented by

⁹precisely, a **Matlab** cell array

Allen et al. (2000). The approach to include user-defined functions in the sequence is a clean and elegant solution for the configuration of the template generation.

Besides these data-dependent methods for the template generation, other methods exist, which do not depend on the data but solely on the number of slices and possible external data. A collection of such functions is provided in the FACET package, which implement the behavior of Niazy et al. (2005), Moosmann et al. (2009) and others (see Sec. 3.8.2). Note that these are not integrated in the `RASequences` setting, since they can be executed before the algorithm itself.

Regarding the customization of the algorithm sequence, the events generated throughout the execution (see Sec. 3.3.2) offer a complementary method to include custom user code at any point during the algorithm runtime.

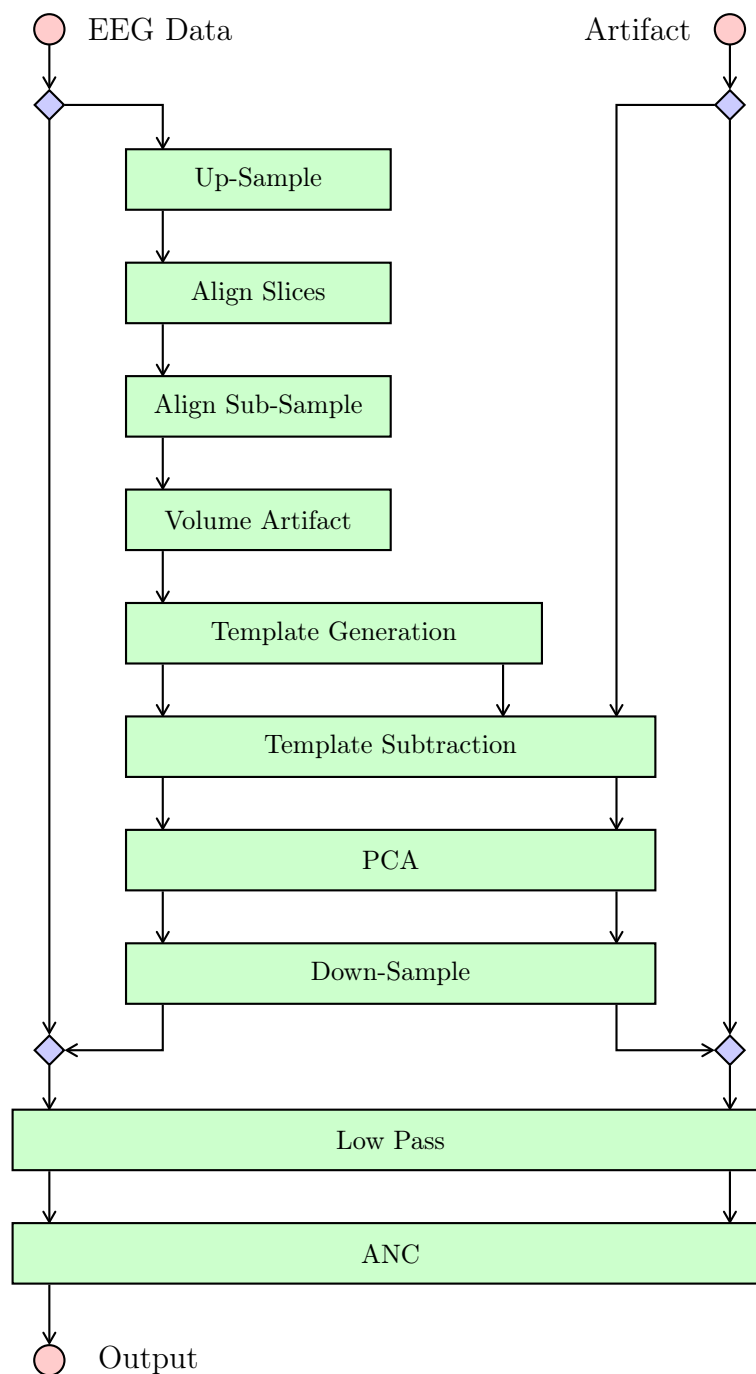
Listing 3.5: Exemplary specification of the steps, which should be performed for artifact removal (from `CleanEx1.m`).

```
%%% Artifact Removal Steps
E.RASequences = {
    'Cut',...
    'UpSample',...
    'AlignSlices',...
    'AlignSubSample',...
    'RemoveVolumeArt',...
    @FACET.AvgArtWghtFARM,...
    'CalcAvgArt',...
    'PCA',...
    'DownSample',...
    'Paste',...
    'LowPass',...
    'ANC' };

```

3.10.2 Example

Listing 3.5 shows an example as implemented by `CleanEx1.m`. In Fig. 3.12 the corresponding data flow graph is given. The top blue diamond symbols denote the function 'Cut', which extracts the period of actual fMRI acquisition from the total EEG data and estimated artifact. This subarea of data is first up-sampled and further processed, including the template subtraction and PCA, before its sampling rate is reduced again. The bottom blue diamonds denote 'Paste', which merges the data back to the full EEG data. This is

**Figure 3.12:** Artifact removal sequence as configured by Lst. 3.5.

finally filtered with a low-pass filter and corrected using adaptive noise cancellation (ANC). Note that the (reconstructed) artifact signal (starting at the top right red circle) is initially zero, i.e. no artifact at all. The data is reconstructed step by step during the artifact removal.

3.11 Evaluation Framework

As soon as the EEG data with gradient artifacts is improved by the artifact correction algorithm, the quality of the results should be assessed. For this purpose, an evaluation framework was developed as part of the toolbox. It provides an extensive set of performance indicators as utilized by different authors (compare Sec. 2.4).

3.11.1 Software Design

The goal was to perform multiple evaluation algorithms on the output data from the artifact removal algorithms. These evaluation results should be saved and then presented to the user in several formats. One format is to print the numbers with some descriptive text to the screen. Additionally, L^AT_EX source code for tables and diagrams should be emitted to be used in high-quality publications. From the user perspective, the evaluation algorithm should provide extensive configurability, but should also be usable as a Matlab one-line command.

As integral part of the artifact correction toolbox, the evaluation framework is included in the Matlab package FACET. The same modern design paradigm of object oriented programming (Sommerville, 2004) as for the correction algorithm is used. The software design provides a separation of the

- execution of performance indicator algorithms, from the
- storage of their results, and the
- presentation of these results.

This is achieved by the object-oriented design as shown in Fig. 3.13. The functionality is divided and realized by the classes.

Eval is the main class which holds all evaluation algorithms. It is instantiated with the original and the corrected EEG data (EEGLAB data structure). The evaluation is performed by the method `eval()`. The

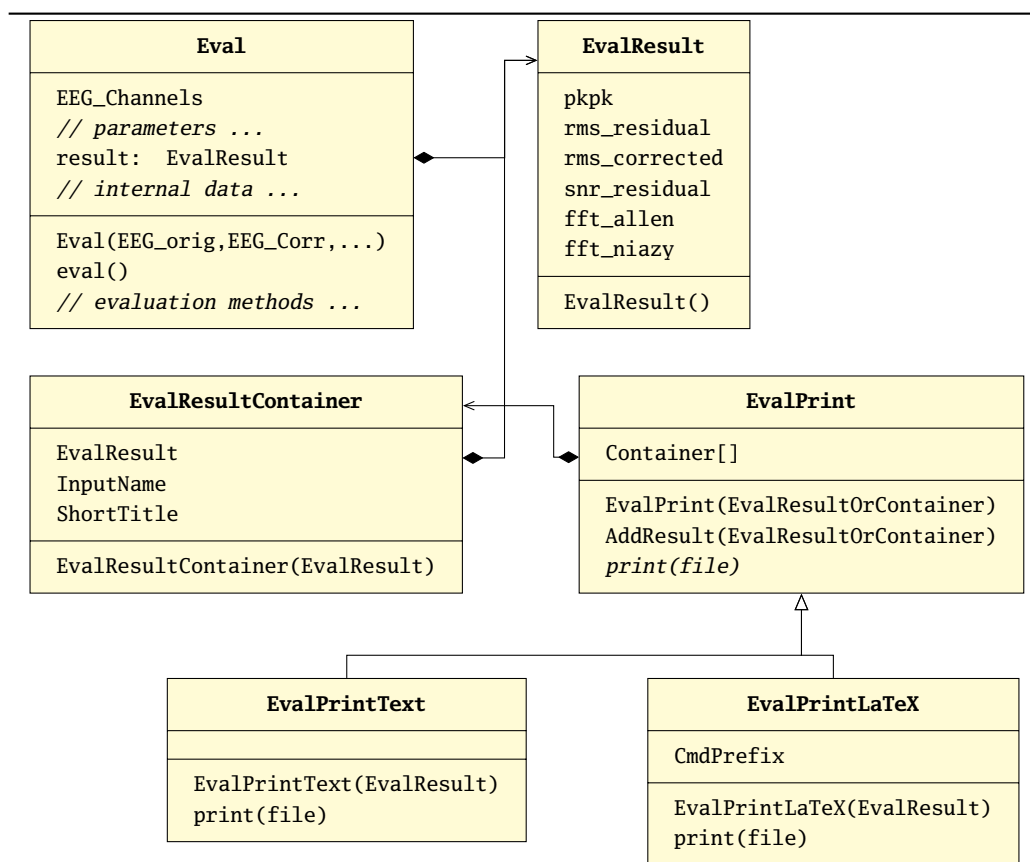


Figure 3.13: UML Class Diagram of the evaluation framework.

results are stored in the member variable `result`, which is an instance of the `EvalResult` class.

EvalResult is a storage object for the evaluation results.

EvalResultContainer wraps the `EvalResult` object and adds meta information (the variable name and a short title), later used by the `EvalPrint` descendants.

EvalPrint is an abstract base class to print the evaluation results in an arbitrary format. Actual printing routines are implemented in descendant classes (see below).

EvalPrintText is a descendant class of `EvalPrint` which implements the `print()` method to display a human-readable table.

EvalPrintLaTeX also descends from `EvalPrint` and implements the creation of output to be used in \LaTeX documents. It generates code using the

TikZ and PGFPlots packages with multiple commands, which are used by the user inside of `table` and `figure` environments.

3.11.2 Data Preparation

All datasets contain recordings during which fMRI acquisition was performed. They additionally contain short periods before and after the fMRI acquisition which don't show gradient artifacts. To utilize these periods for comparison with the corrected data, the period before and after the fMRI acquisition are merged to a single interval and supplied to the individual evaluation algorithms.

A second point to consider is the processing of these periods by the artifact correction algorithms. In some cases, only the period during fMRI acquisition is filtered by a low-pass (cmp. Sec. 3.9). In the left spectrogram in Fig. 3.11, the blue portions in the frequency range above 70 Hz from approx. 30 s to 150 s show, that the low-pass was only applied for this period. A comparison of the corrected data (with an applied low-pass) with data outside of the fMRI gradient artifacts (without a low-pass filtering) would lead to invalid results. Therefore the evaluation framework provides means to apply filters to the undisturbed data.

3.11.3 Performance Indicators

Section 2.4 summarizes performance indicators found in publications. Many of these were implemented in the evaluation framework. Unfortunately the publications didn't provide enough details for all algorithms, therefore some assumptions were necessary.

Median Imaging Artifact. The median signal amplitude range across all channels is calculated. The amplitude of the artifact is used by [Allen et al. \(2000\)](#) as an indicator of the quality of their algorithm (see Sec. 2.4.1). Unfortunately the publication is vague on the definition of this indicator therefore some assumptions had to be made for the implementation.

Ten intervals with a length of 10 % to 20 % more than the slice period time are taken from the EEG data of every channel. These intervals are equally spaced with a distance to cover the whole duration of the fMRI acquisition. The range (maximum value minus minimum value) of each interval is calculated and averaged across the ten samples. This results in a mean imaging artifact

range (also called peak-to-peak value) of every channel of every subject of every recording. Finally the minimum, maximum and median of these ranges are calculated, where the latter is called “Median Imaging Artifact”.

Although [Allen et al. \(2000\)](#) solely use the median imaging artifact to show the reduction of the residual artifact, we also calculate the median range of the EEG data without fMRI acquisition for comparison. Therefore the very same algorithm is performed on the (merged) EEG data before and after fMRI acquisition.

RMS Corrected to Unimpaired. The performance indicator used by [Moosmann et al. \(2009\)](#) is the ratio of the RMS of the (DC-free) corrected EEG signal to the RMS of the signal without fMRI acquisition (see Sec. 2.4.2). The evaluation tool calculates this ratio individually for every channel and returns descriptive statistics on them.

RMS Uncorrected to Corrected. [van der Meer et al. \(2010\)](#) use the ratio of the RMS of the uncorrected EEG signal to the RMS of the corrected signal (see Sec. 2.4.2). The evaluation tool calculates this ratio individually for every channel and returns descriptive statistics on them.

SNR of Corrected. The Signal to Noise Ratio (SNR) as defined by equation (2.4) in Sec. 2.4.3 relates the undistorted signal power S to the noise power N . In many cases these values are not directly available for practical calculations. Examples are the EEG signal from an fMRI acquisition or the result from the artifact correction algorithm.

In these cases only the power of the distorted signal D is known. Assuming additive noise, the distorted signal can be written as sum of the undistorted signal and the noise signal $x_D(t) = x_S(t) + x_N(t)$. Utilizing the statistical independence, the power of the undistorted signal and the noise signal are also additive: $D = S + N$.

Most EEG datasets with fMRI acquisition also contain periods without fMRI acquisition. These can be used as a sample of the undistorted signal to calculate S . With this information, the noise power is given by $N = D - S$ and the SNR is

$$\text{SNR} = \frac{S}{D - S}. \quad (3.3)$$

This equation is applied for every channel of the corrected EEG dataset with D as the corrected signal and S the signal outside of the fMRI acquisition periods.

Due to the subtraction term $D - S$ the result can be negative. This happens when the correction algorithm has removed more signal power than the artifact signal power. Physically a negative noise power $N = D - S$ does not make sense, therefore only positive SNR values are considered in the descriptive statistics.

Median Residual Activity. To compare the activity in four EEG frequency bands (0.8–4 Hz (Delta waves), 4–8 Hz (Theta waves), 8–12 Hz (Alpha waves) and 12–24 Hz (part of the Beta wave spectrum)) (Allen et al., 2000, see also Sec. 2.4.4), ten equally spaced periods of 3 sec. (which are 6.000 samples at a sampling rate of 2 kSps) were averaged and then transformed to frequency domain with an FFT. The activity is calculated as the sum of the magnitude spectrum in the frequency band.

Power Density at Slice Frequency. This performance indicators lists the power density reduction achieved by the artifact correction at the slice frequency and its harmonics. For the given original and the corrected datasets an FFT is performed for every channel. The magnitudes at the frequency bins of the volume and the slice frequencies and four harmonics are divided (corrected/original) and squared. These values are converted to decibel (dB) and the mean over all channels is calculated.

The automatic generation of L^AT_EX source code by EvalPrintLaTeX for clarity only includes a subset of the evaluation results. For the “Median Imaging Artifact” the median amplitude range of the corrected data is shown. The “RMS Corrected to Unimpaired”, the “RMS Uncorrected to Corrected” as well as the “SNR of Corrected” are represented by the respective mean values across all channels. The mean SNR value is supplemented by the number of included values with a positive noise power. For the “Power Density at Slice Frequency” the averaged value in dB of the slice frequency and its harmonics across all channels are given.

3.11.4 Usage Examples

For a quick evaluation of the results, the evaluation framework is usable with a one line Matlab command. The example in Lst. 3.6 compares the corrected

dataset `clean1` to the raw dataset `EEG_FMRIB`, but limits the comparison to channels 1 to 30 (because channel 31 contains ECG data, see Sec. 4.1.1). Additionally, the number of slices per volumes is given as 21. The command-line creates an `Eval` object and executes its `eval()` method. Then it creates an `EvalPrintText` object and `print()`s the evaluation result to the screen. The evaluation result is stored to the variable `eval1`.

Listing 3.6: Exemplary one-line Matlab command to evaluate the result of the correction algorithm and to print the result.

```
>> eval1=FACET.EvalPrintText(FACET.Eval(EEG_FMRIB,cleaned1,[1:30],21).eval()).print();
```

For a more complex cases, it is advisable to store the `Eval`, `EvalResult` and `EvalPrint*` objects to variables and access their member variables for fine tuning. An example is given in Lst. 3.7. In the first part, three datasets are evaluated, each corrected with different algorithm parameters. In the second part, a `EvalPrintLaTeX` object is created. The evaluation results are added and short labels are provided. A prefix for the generated \LaTeX commands is given, before the result is printed to a file. This can be used in a \LaTeX document, which flexibly places the generated tables and diagrams. Chapter 4 extensively uses this feature.

Listing 3.7: Example of the usage of the evaluation framework to generate \LaTeX tables and diagrams.

```
% Evaluate data
eval_CleanEx4 = FACET.Eval(EEG_FMRIB,HBM_CleanEx4,[1:30],21).eval();
eval_Niazy    = FACET.Eval(EEG_FMRIB,HBM_Niazy,    [1:30],21).eval();
eval_CleanEx1 = FACET.Eval(EEG_FMRIB,HBM_CleanEx1,[1:30],21).eval();
% Create LaTeX include file with tables and diagrams
epl=FACET.EvalPrintLaTeX();
epl.AddResult(FACET.EvalResultContainer(eval_CleanEx4,'Allen'));
epl.AddResult(FACET.EvalResultContainer(eval_Niazy,   'Niazy'));
epl.AddResult(FACET.EvalResultContainer(eval_CleanEx1,'EEGfMRI'));
epl.CmdPrefix='HBM';
% Save to file
fid=fopen(' ../paper/eval.inc.tex','w');
epl.print(fid);
fclose(fid);
```

Evaluation of EEGfMRI

THE presented artifact correction toolbox “FACET” is used to implement an optimum artifact correction algorithm named “EEGfMRI”. The degree to which the artifacts were removed by this algorithm as well as selected existing algorithms as summarized in Sec. 2.3 is evaluated with the performance indicators outlined in Sec. 2.4. For the reproducible and user-friendly application of the evaluation a dedicated framework was developed, which was described in Sec. 3.11. The results for the existing artifact correction algorithms and for the presented new algorithm are given in the following sections. This is followed by a discussion of these results.

Two datasets are used for the evaluation: the example data supplied with the FMRIB plugin by Niazy et al. (2005) and an own pilot dataset (see Sec. 4.1). These are corrected using the algorithm by Allen et al. (2000) (see Sec. 2.3.1) and the algorithm by Niazy et al. (2005) (see Sec. 2.3.2) as well as with EEGfMRI. The abbreviations “Allen”, “Niazy” and “EEGfMRI” will be used from now on.

Precisely, the toolbox FACET is also used to implement the algorithm by Allen et al. (2000) showing its universal applicability. Allen et al. (2000) report to use blocks of 25 volumes for averaging if the fMRI sequence produces volume gaps. Since the FMRI dataset was recorded with only 40 volumes and the FACET toolbox inherently handles volume gaps, the algorithm is setup to treat the data as Allen et al. (2000) did if no volume gaps were present. This means that a block length of 100 slices are used. The pilot dataset does not show volume gaps, so this is also corrected with 100 slices per blocks. The equal treatment of both datasets also allows better comparison of the results.

Since FACET is a generic toolbox of which multiple options and procedures are used by EEGfMRI, the individual gain of each option is investigated. These options should provide an improvement to the starting point of the algorithm by Niazy et al. (2005). According to the generalized scheme of fMRI artifact correction algorithms (see Sec. 3.2.4) the evaluation is split to the improvements located in the pre-processing, template-generation and post-processing parts.

Firstly, the pre-processing and template generation improvements provided by FACET and employed by EEGfMRI are investigated. The post-processing steps are disabled to enable a clear view to their effect. This evaluation is preceded by a comparison of the three mentioned algorithms with deactivated post-processing. This is followed by the incremental activation of the pre-processing and template-generation steps.

Secondly, the post-processing steps also used by Niazy et al. (2005) are incrementally activated in EEGfMRI and the results evaluated. Finally all three algorithms are compared with fully activated post-processing.

The same evaluation is then performed again using the pilot dataset. The final comparison is extended by the evaluation of the artifact correction results achieved by the online algorithm provided by the used EEG recorder.

All computations were performed using Matlab 7.8.0.347 (R2009a) 64-bit (glnxa64) on a GNU/Linux Debian operating system (kernel release 3.2, architecture x86_64). It was executed on a PC with an Intel® Core™ i7 860 CPU with 2.80 GHz and 8 GiB RAM. Although a multi-core CPU was used, only a single computational task was employed to work around a Matlab bug.¹

¹<http://www.mathworks.com/support/bugreports/532399> [visited 2012-04-24, login required], Matlab was started with the command line parameter `-singleCompThread`

4.1 Data

For the evaluation two datasets are used, the FMRI and an own pilot dataset. This section describes the datasets including their origin, properties and appearance.

4.1.1 FMRI Dataset

The FMRI dataset is included in the FMRI EEGLAB plugin and is also freely available at <http://www.fmrib.ox.ac.uk/eeqlab/fmribplugin/>. The site doesn't give a lot details on the recording, but those given are mostly consistent with [Niazy et al. \(2005\)](#). Therefore we use this paper for information which is missing for the dataset as well as results from the investigation of the dataset itself.

The MR device employed for acquisition was a 3 T Varian Inova scanner. They used an echo planar imaging (EPI) sequence with $TR=3$ s and 21 slices per volume with a slice time of 142.6 ms and an inter-volume gap of 5 ms. Each slice consists of 64 lines. A total of 40 volumes were recorded which results in an acquisition time of 120 s (2 minutes) and 840 slices. The subject's task was to open and close his eyes every 10 seconds.

Of the total 32 recorded channels, 30 EEG channels according to the 10–20 international system with common reference electrode at the FCz location were used. These are complemented by two bipolar channels for electromyograph (EMG) and electrocardiograph (ECG). An SystemPLUS EEG system and an SD32 MRI amplifier by Micromed s.r.l., TV, Italy were employed. All channels had a 10 k Ω series resistor for current limiting and a 600 Hz, first order (20 dB/decade) low-pass anti-aliasing filter as well as a 0.15 Hz, second-order (40 dB/decade) high-pass filter. The recording used a sigma-delta analog-to-digital converter (ADC) with a sampling rate of 2048 Hz. The amplifier has an input voltage range of ± 25.6 mV and a resolution of 12.2 nV what means 22 bits resolution.

The data itself ranges from -45.5 mV to $+51.8$ mV. Visual inspection reveals no clipping or saturation effects. It has a quantization resolution of 390.2 nV, so it seems that it used a different amplifier setting with a 32 times (5 bits) coarser resolution and also higher input voltage range.

The EEG was recorded for 162 s and stored as Matlab file with data type single ([IEEE Task P754, 1985](#)) (32 bits, 23 bits mantissa, 8 bits exponent).

Since the dynamic range of the data is approx. 18 bits, and the single precision data type offers 23 bits mantissa, it does not affect the data resolution.

This dataset was used throughout this work to visualize the artifact, see Figs. 1.1, 2.2, 2.3 and 2.5 for reference on the amplitude values and artifact pattern.

4.1.2 Pilot Dataset

The pilot dataset was recorded for this work as a test acquisition at the MR Center of Excellence, Medical University Vienna, Vienna, Austria in accordance with the 1975 Helsinki declaration and local ethics regulations. The subject's task was to keep his eyes closed, stay as still as possible and not thinking of anything.

The MR acquisition was performed with a 3 T Siemens TIM Trio scanner using a 32-channel head coil. The parameters of the echo planar imaging (EPI) sequence were a volume repetition time of $TR=2$ s with 25 axial slices per volume and a slice time of 80 ms (12.5 Hz). The sequence does not have an inter-volume gap. Each slice consists of a 128×128 matrix. A total of 150 volumes were recorded which results in 5 minutes of acquisition.

For the EEG and EMG recording a neuroConn NEURO PRAX[®] MR device with 64 channels, an 800 Hz anti-aliasing filter, with a 24 bit ADC was used (*neuroConn NEURO PRAX MR*, 2009; Schlegelmilch et al., 2004; Berkes, Schellhorn, Schlegelmilch, Markert, & Husar, 2004; Berkes, Husar, et al., 2004). The data was recorded with 2000 samples per second.

The dataset consists of 22 channels of which three channels are EEG (Fz, Cz, Pz) and ten channels are unipolar EMG signals from which 5 bipolar EMG channels are calculated. These measured the facial muscles M. frontalis, M. corrugator supercilii, M. orbicularis oculi, M. zygomaticus major, and M. masseter. Two channels recorded the horizontal and vertical electrooculogram (EOG), one channel recorded the current heart rate and one recorded the electrocardiograph (ECG). The latter does not contain data due to a recording problem.

The ten raw unipolar EMG channels have a range from -263.4 mV to 286.4 mV, the five bipolar EMG channels range from -251.4 mV to 342.2 mV. The two EOG channels range from -213.0 mV to 508.9 mV. The three EEG channels range from -156.0 mV to 503.8 mV. The data does not show quantization effects so it seems it was preprocessed and no conclusions on the ADC reso-

lution can be drawn. Figure 4.1 shows an exemplary section of the dataset recorded at an EMG electrode.

The EEG and EMG data was recorded for 324.5 s and stored as a Matlab file with data type single.

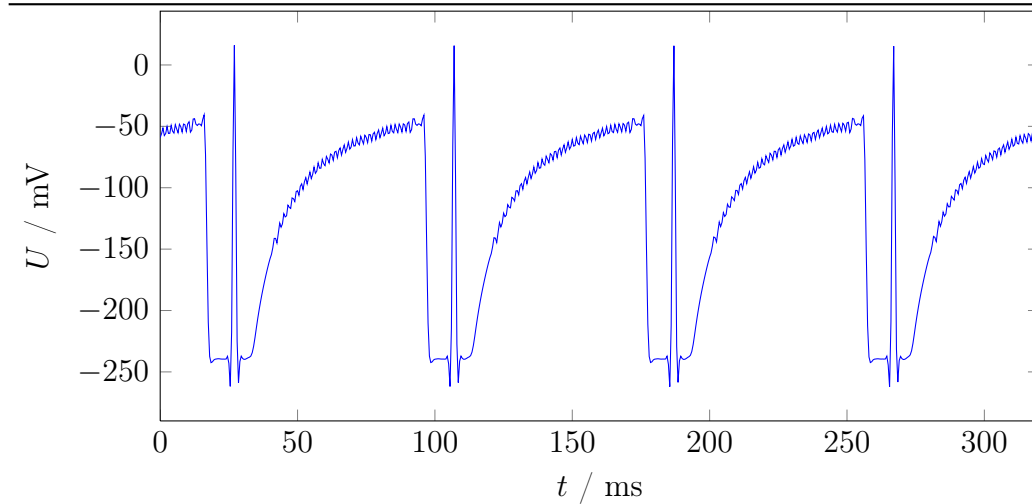


Figure 4.1: Exemplary section of the pilot dataset with four consecutive fMRI slice acquisition periods measured with a facial EMG electrode. The artifact amplitude is nearly 300 mV.

4.2 Comparison Without Post-Processing

As a starting point, the results of the algorithms of [Allen et al. \(2000\)](#), [Niazy et al. \(2005\)](#) and EEGfMRI are compared, while the post-processing is switched off. EEGfMRI is configured with all improvements over [Niazy et al. \(2005\)](#) switched off, i.e. to be as close as possible to their algorithm. The evaluation results are given in Tab. 4.1 and Figs. 4.2 to 4.7. For a description of the utilized performance indicators see Sec. 3.11.3.

All three algorithms show similar results. Allen shows slightly less residual median imaging artifact and RMS of the corrected signal and hence higher ratio of RMS of the uncorrected to the corrected signal and higher SNR. The median residual activity is worse for the 8–12 Hz and 12–24 Hz bands but better for the 0.8–4 Hz and 4–8 Hz bands.

The reason for this advantage most probably lies in Allen’s template generation algorithm. As outlined in Sec. 2.3.1 the main problem of averaging slices

Table 4.1: Comparison of the results of Allen et al. (2000), Niazy et al. (2005) and EEGfMRI without post-processing.

	Allen	Niazy	EEGfMRI
Median Imaging Artifact (μV)	513	557	557
RMS Corrected to Unimpaired	4.92	5.67	5.68
RMS Uncorrected to Corrected	20.3	17.9	17.9
SNR of Corrected	0.224 (30)	0.218 (30)	0.215 (30)
Median Residual Activity			
0.8 – 4.0 Hz	30 %	35 %	35 %
4.0 – 8.0 Hz	20 %	25 %	25 %
8.0 – 12.0 Hz	35 %	25 %	25 %
12.0 – 24.0 Hz	33 %	26 %	25 %
Power Density at Slice Frequency			
1: 7.00 Hz	-53 dB	-50 dB	-49 dB
2: 14.00 Hz	-50 dB	-52 dB	-48 dB
3: 21.00 Hz	-63 dB	-62 dB	-58 dB
4: 28.00 Hz	-59 dB	-59 dB	-55 dB
5: 35.00 Hz	-64 dB	-62 dB	-57 dB

is the missing synchronization of the fMRI and EEG periods which leads to a sub-sample uncertainty. The algorithm selects slices for averaging with a cross-correlation of at least 0.975 (cmp. Sec. 2.3.1) while the others do not consider the congruence.

EEGfMRI shows nearly identical values to Niazy except for the power density reduction at slice frequency harmonics, where it is 4–5 dB worse.

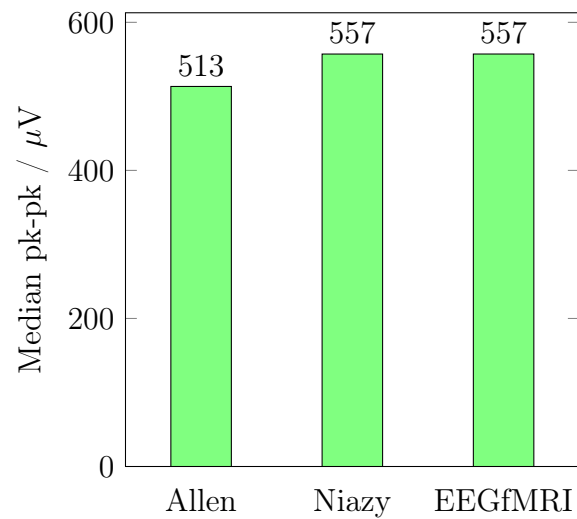


Figure 4.2: Comparison of the results of [Allen et al. \(2000\)](#), [Niazy et al. \(2005\)](#) and EEGfMRI without post-processing by the median imaging artifact (lower is better).

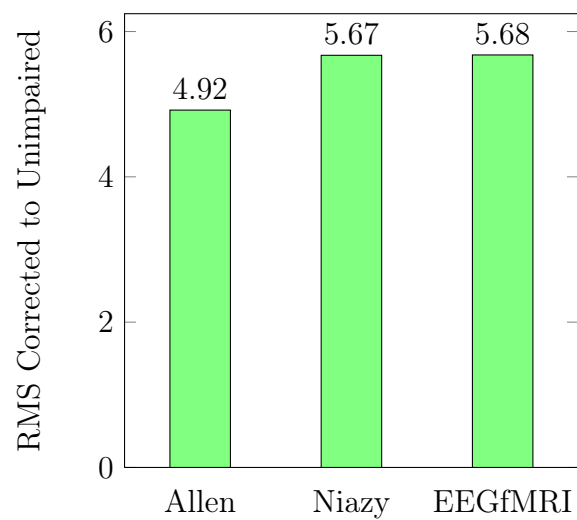


Figure 4.3: Comparison of the results of [Allen et al. \(2000\)](#), [Niazy et al. \(2005\)](#) and EEGfMRI without post-processing by the RMS of the corrected to the unimpaired signal (nearer to 1.0 is better).

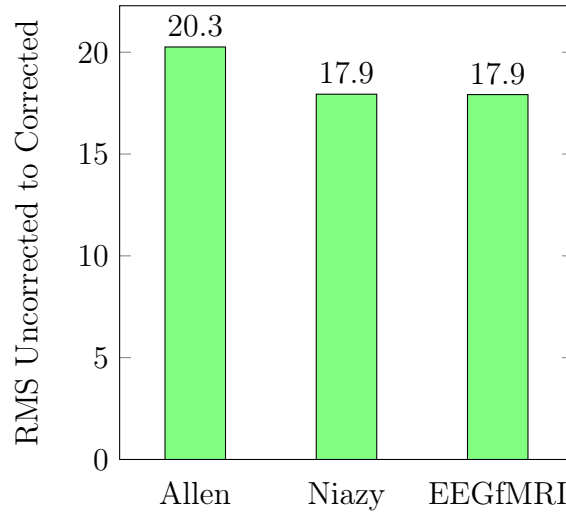


Figure 4.4: Comparison of the results of [Allen et al. \(2000\)](#), [Niazy et al. \(2005\)](#) and EEGfMRI without post-processing by the RMS of the uncorrected to the corrected signal (larger is better).

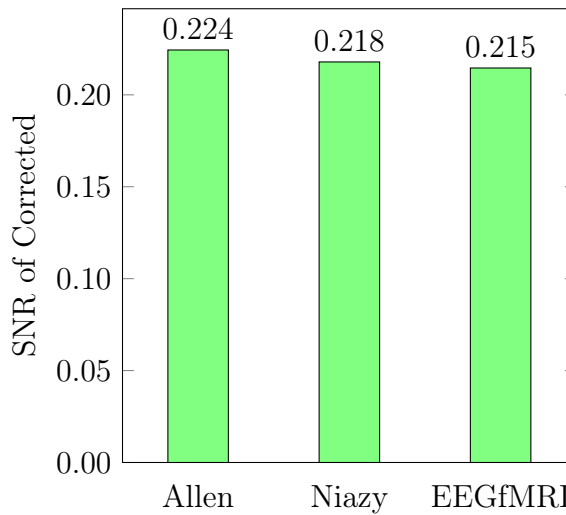


Figure 4.5: Comparison of the results of [Allen et al. \(2000\)](#), [Niazy et al. \(2005\)](#) and EEGfMRI without post-processing by the SNR of the corrected signal (larger is better).

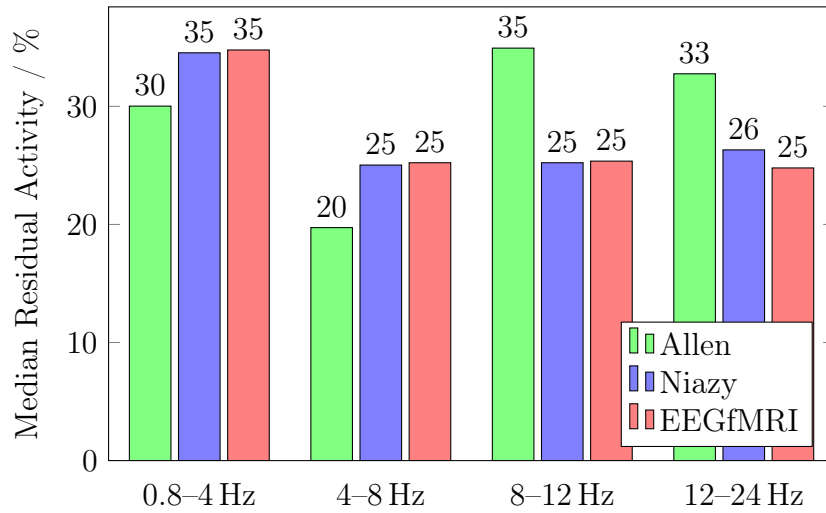


Figure 4.6: Comparison of the results of Allen et al. (2000), Niazy et al. (2005) and EEGfMRI without post-processing by the median residual activity (lower is better).

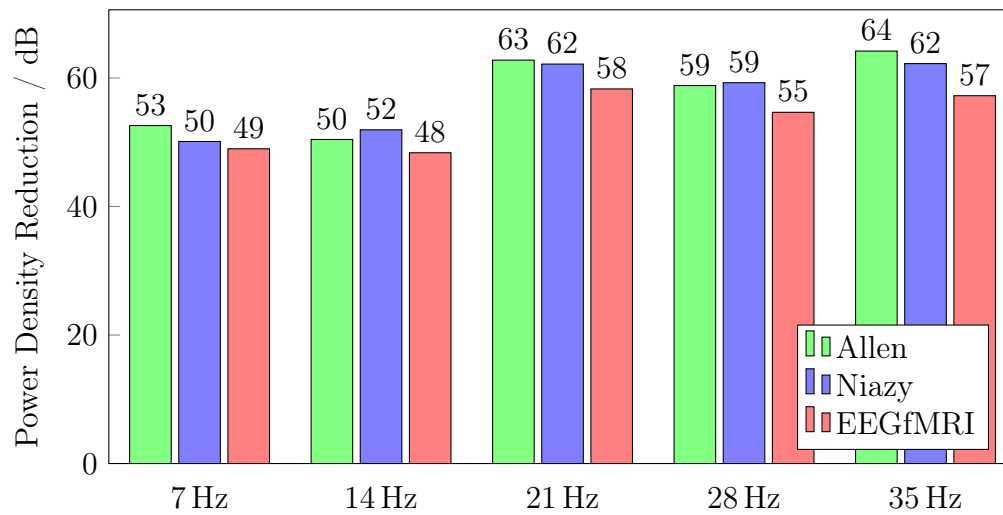


Figure 4.7: Comparison of the results of Allen et al. (2000), Niazy et al. (2005) and EEGfMRI without post-processing by the power density reduction at slice frequency harmonics (larger is better).

4.3 Incremental Activation of Pre-Processing and Template Generation Improvements

In this section six improvements of the pre-processing and template generation steps are added incrementally to the correction algorithm. The order of activation is the same as the order of their occurrence in the algorithm flow (cmp. Sec. 3.10 and Fig. 3.12).

The starting point (abbreviated **raw**) are the settings used in the previous section. To be as similar to Niaz et al. (2005) as possible, firstly the cut-off frequency during upsampling was set to 1.0 which results in interpolation errors (see Sec. 3.6.3). Secondly, the template generation used alternating slices, i.e., slices 2, 4, 6, ... for the first slice, slices 3, 5, 7, ... for the second slice, and so on, using a sliding average. And thirdly, the volume gaps in the templates were set to 0.0.

In the following abbreviations are used to specify each improvement throughout this section.

PreFilter adds a 1 Hz high-pass to filter the EEG signal before any further processing (see Sec. 3.5).

Upsample0.5 corrects the interpolation cut-off frequency setting from 1.0 to 0.5 (see Sec. 3.6.3).

AlignSubSample switches on the temporal alignment of the slices with sub-sample resolution to the reference slice (see Sec. 3.6).

RemoveVolumeArtifact removes the volume artifact at volume acquisition boundaries (see Sec. 3.7).

AvgArtWghtFARM changes the template generation algorithm to select the best fit slices for the averaging according to van der Meer et al. (2010) (see Sec. 3.8.2).

InterpolateVolGaps generates an interpolated signal during volume gaps when calculating the artifact estimation instead of 0.0 as described at the end of Sec. 3.8.1.

The results are given in Tab. 4.2 and Figs. 4.8 to 4.13.

(a) **raw**: The first column repeats the results from the previous section as reference.

Table 4.2: Comparison of the results with incremental activation of the pre-processing and template generation improvements.

	(a)	(b)	(c)	(d)	(e)	(f)	(g)
(a) raw							
(b) +PreFilter							
(c) +Upsample0.5							
(d) +AlignSubSample							
(e) +RemoveVolumeArt							
(f) +AvgArtWghtFARM							
(g) +InterpolateVolGaps							
Median Imaging Artifact (μ V)	557	557	509	143	141	110	110
RMS Corrected to Unimpaired	5.68	5.67	4.99	1.58	1.57	1.02	1.01
RMS Uncorrected to Corrected	17.9	18.0	20.1	64.6	65.2	93.5	93.6
SNR of Corrected	0.215 (30)	0.225 (30)	0.267 (30)	2.61 (19)	3.51 (19)	4.29 (12)	4.36 (12)
Median Residual Activity							
0.8 – 4.0 Hz	35 %	37 %	33 %	33 %	37 %	47 %	47 %
4.0 – 8.0 Hz	25 %	26 %	24 %	24 %	27 %	17 %	15 %
8.0 – 12.0 Hz	25 %	25 %	32 %	31 %	37 %	37 %	38 %
12.0 – 24.0 Hz	25 %	24 %	30 %	30 %	27 %	24 %	22 %
Power Density at Slice Frequency							
1: 7.00 Hz	-49 dB	-49 dB	-51 dB	-51 dB	-49 dB	-40 dB	-39 dB
2: 14.00 Hz	-48 dB	-48 dB	-50 dB	-50 dB	-52 dB	-47 dB	-51 dB
3: 21.00 Hz	-58 dB	-58 dB	-62 dB	-62 dB	-62 dB	-55 dB	-57 dB
4: 28.00 Hz	-55 dB	-55 dB	-57 dB	-56 dB	-57 dB	-54 dB	-56 dB
5: 35.00 Hz	-57 dB	-57 dB	-60 dB	-60 dB	-61 dB	-57 dB	-61 dB

- (b) **+PreFilter**: Adding a 1 Hz high-pass pre-filter has only minor influence.
- (c) **+Upsample0.5**: Correcting the interpolation error shows an improvement in all numbers except in the median residual activity from 8–24 Hz.
- (d) **+AlignSubSample**: If the slices are aligned with sub-sample resolution, a large improvement in all time-domain values (median imaging artifact, RMS corrected to unimpaired, RMS uncorrected to corrected and SNR of corrected) is achieved. The frequency domain performance indicators (median residual activity and power density reduction at slice frequency) show mixed results.
- (e) **+RemoveVolumeArt**: Removing the volume artifact shows only a small improvement. The median residual activity from 0.8–12 Hz even gets worse and the removed power density at slice frequency 7 Hz also drops.
- (f) **+AvgArtWghtFARM**: Using best-fit slices for averaging leads to a strong reduction of artifacts, as shown by the time-domain values. The frequency domain shows increased residual activity at 0.8–4 Hz and less removed power density at slice frequency harmonics.
- (g) **+InterpolateVolGaps**: Ensuring a continuous signal during volume gaps with a linear interpolated signal has a small positive effect.

A closer look at the FFT of the corrected EEG signal shows that (a)-(e) have deep notches at the slice frequency and its harmonics. These result in a good power density reduction at these frequencies. When **AvgArtWghtFARM** is added, these notches vanish and show a continuous spectrum. This means that less of the real EEG components are removed.

In total, these six improvements result in a reduction of the median imaging artifact and the RMS of the corrected to the RMS of the unimpaired signal by a factor of approximately 5 while the RMS of the uncorrected to the RMS of the corrected signal increases by approximately the same amount. The SNR is even improved by a factor of 20.

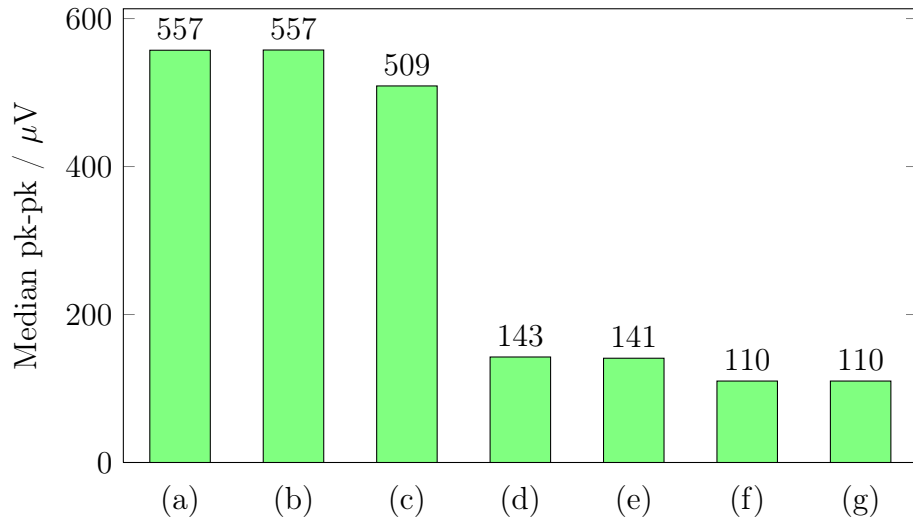


Figure 4.8: Comparison of the results with incremental activation of the pre-processing and template generation improvements by the median imaging artifact (lower is better). (a) raw, (b) +PreFilter, (c) +Upsample0.5, (d) +AlignSubSample, (e) +RemoveVolumeArt, (f) +AvgArtWghtFARM, (g) +InterpolateVolGaps

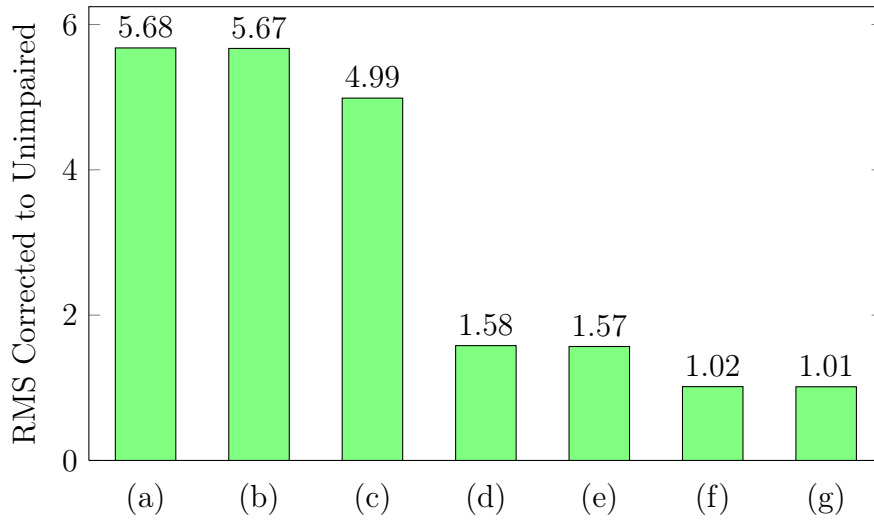


Figure 4.9: Comparison of the results with incremental activation of the pre-processing and template generation improvements by the RMS of the corrected to the unimpaired signal (nearer to 1.0 is better). (a) raw, (b) +PreFilter, (c) +Upsample0.5, (d) +AlignSubSample, (e) +RemoveVolumeArt, (f) +AvgArtWghtFARM, (g) +InterpolateVolGaps

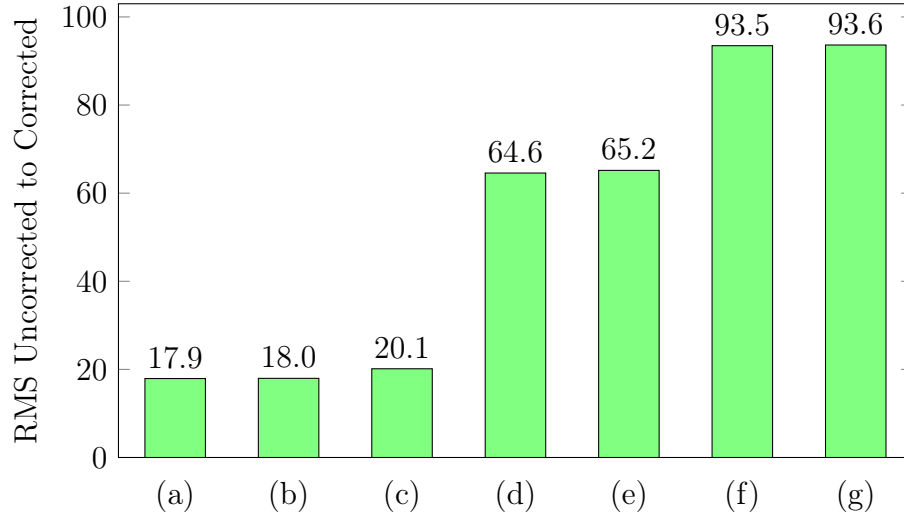


Figure 4.10: Comparison of the results with incremental activation of the pre-processing and template generation improvements by the RMS of the uncorrected to the corrected signal (larger is better). (a) raw, (b) +PreFilter, (c) +Upsample0.5, (d) +AlignSubSample, (e) +RemoveVolumeArt, (f) +AvgArtWghtFARM, (g) +InterpolateVolGaps

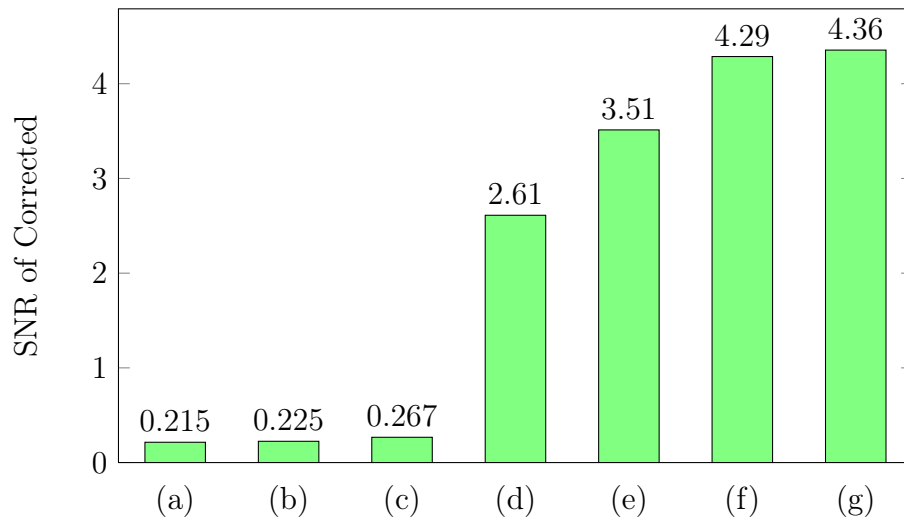


Figure 4.11: Comparison of the results with incremental activation of the pre-processing and template generation improvements by the SNR of the corrected signal (larger is better). (a) raw, (b) +PreFilter, (c) +Upsample0.5, (d) +AlignSubSample, (e) +RemoveVolumeArt, (f) +AvgArtWghtFARM, (g) +InterpolateVolGaps

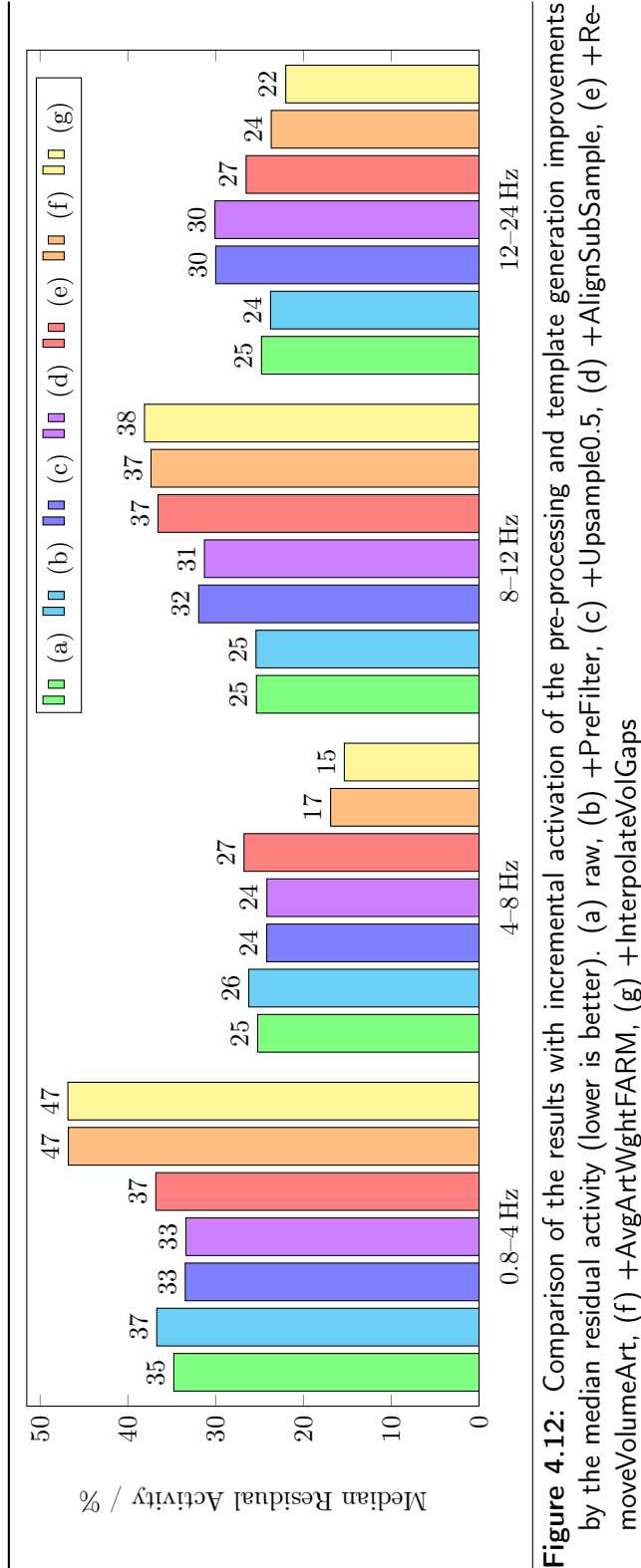
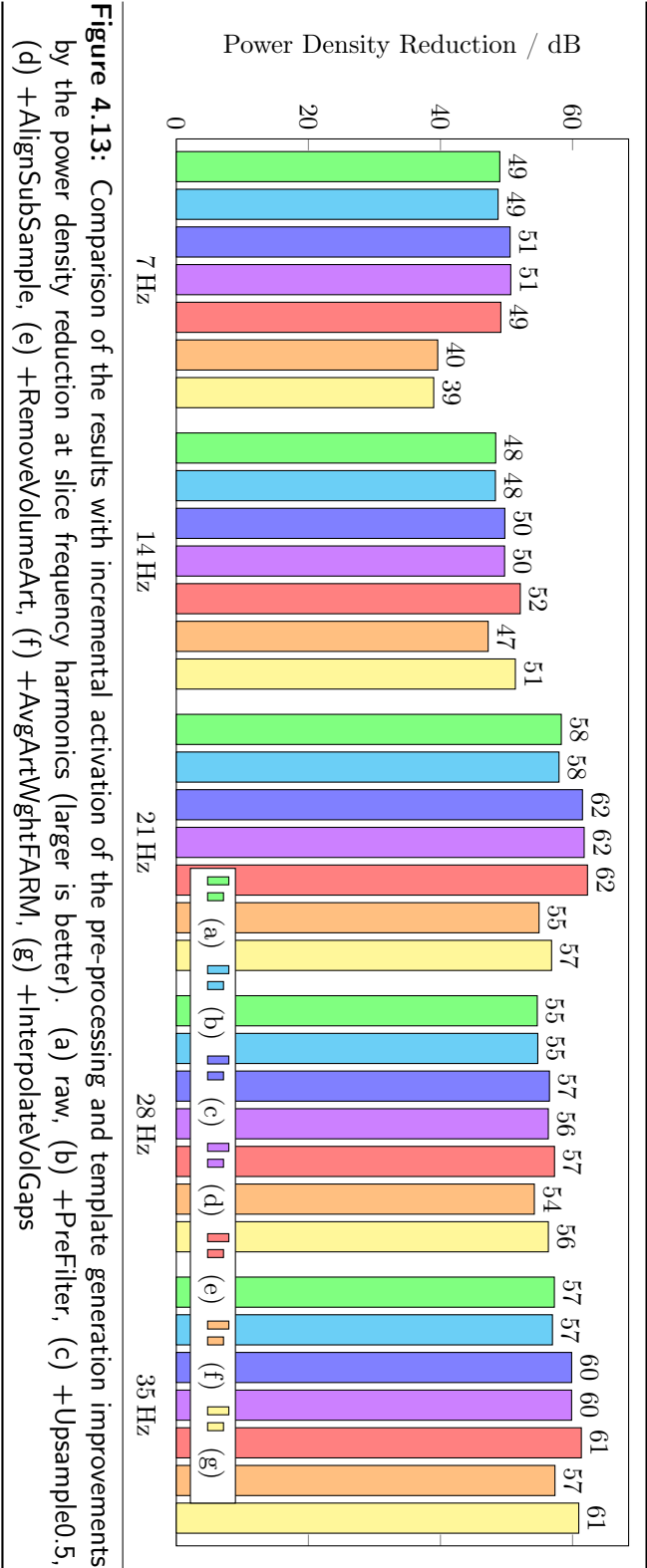


Figure 4.12: Comparison of the results with incremental activation of the pre-processing and template generation improvements by the median residual activity (lower is better). (a) raw, (b) +PreFilter, (c) +Upsample0.5, (d) +AlignSubSample, (e) +Re-moveVolumeArt, (f) +AvgArtWghtFARM, (g) +InterpolateVolGaps



4.4 Incremental Activation of Post-Processing Steps

In the previous sections the results of the pre-processing and template generation with switched off post-processing were investigated. In this section the post-processing steps are enabled incrementally. The following abbreviations are used.

PCA adds a principal component analysis and removes the strongest components related to the fMRI artifact. This was called optimum basis set by [Niazy et al. \(2005\)](#).

LowPass filters the corrected signal with a 70 Hz low-pass which removes all residual high-frequency components. Compare the spectrogram given in [Fig. 3.11](#).

ANC uses adaptive noise cancellation as introduced by [Allen et al. \(2000\)](#) and also used by [Niazy et al. \(2005\)](#) (see [Sec. 2.3.1](#) and [2.3.2](#)).

These three post-processing steps are the same as used by [Niazy et al. \(2005\)](#). The results are given in [Tab. 4.3](#) and [Figs. 4.14](#) to [4.19](#).

(a) **previous**: Again, the last result of the previous section with all pre-processing and template generation improvements enabled is repeated for reference.

(b) **PCA**: Adding PCA shows a large improvement of the SNR and a small improvement in the other time-domain performance indicators. The frequency domain values do not change.

(c) **LowPass**: Filtering with a low-pass results in a strong reduction of the median imaging artifact, i.e, the amplitude. The other time-domain performance indicators also show improvements. While the power density at slice frequency harmonics did not change, the median residual activity is slightly deteriorated in the 4–8 Hz and 8–12 Hz bands.

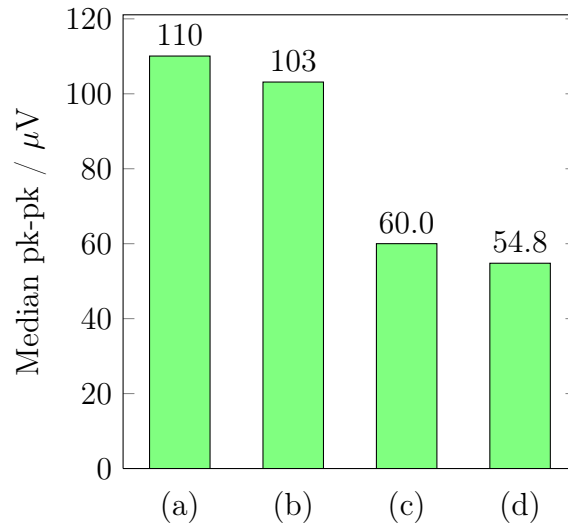
(d) **ANC**: A strong improvement of the median imaging artifact (amplitude) and the SNR are achieved using ANC. It also effects a considerable reduction of the power density in higher harmonics of the slice frequency (21 Hz, 28 Hz and 35 Hz).

Note that the ratio of the RMS of the corrected EEG to the RMS of the unimpaired EEG is below 1.0. This means that the correction algorithm has even removed a small fraction of the real EEG.

Table 4.3: Comparison of the results with incremental activation of the post-processing steps.

- (a) previous
 (b) +PCA
 (c) +LowPass
 (d) +ANC

	(a)	(b)	(c)	(d)
Median Imaging Artifact (μV)	110	103	60.0	54.8
RMS Corrected to Unimpaired	1.01	0.982	0.861	0.840
RMS Uncorrected to Corrected	93.6	96.3	106	109
SNR of Corrected	4.36 (12)	15.2 (12)	16.4 (8)	53.5 (6)
Median Residual Activity				
0.8 – 4.0 Hz	47 %	47 %	43 %	42 %
4.0 – 8.0 Hz	15 %	15 %	16 %	13 %
8.0 – 12.0 Hz	38 %	38 %	42 %	42 %
12.0 – 24.0 Hz	22 %	22 %	19 %	10 %
Power Density at Slice Frequency				
1: 7.00 Hz	-39 dB	-39 dB	-39 dB	-42 dB
2: 14.00 Hz	-51 dB	-51 dB	-51 dB	-53 dB
3: 21.00 Hz	-57 dB	-57 dB	-57 dB	-69 dB
4: 28.00 Hz	-56 dB	-56 dB	-57 dB	-68 dB
5: 35.00 Hz	-61 dB	-61 dB	-61 dB	-69 dB

**Figure 4.14:** Comparison of the results with incremental activation of the post-processing steps by the median imaging artifact (lower is better). (a) previous, (b) +PCA, (c) +LowPass, (d) +ANC

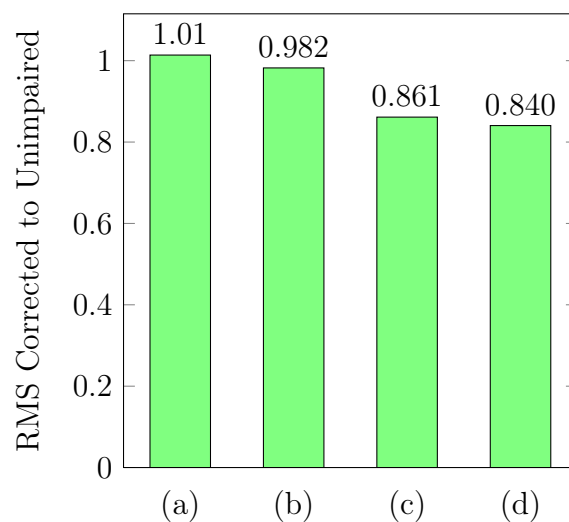


Figure 4.15: Comparison of the results with incremental activation of the post-processing steps by the RMS of the corrected to the unimpaired signal (nearer to 1.0 is better). (a) previous, (b) +PCA, (c) +LowPass, (d) +ANC

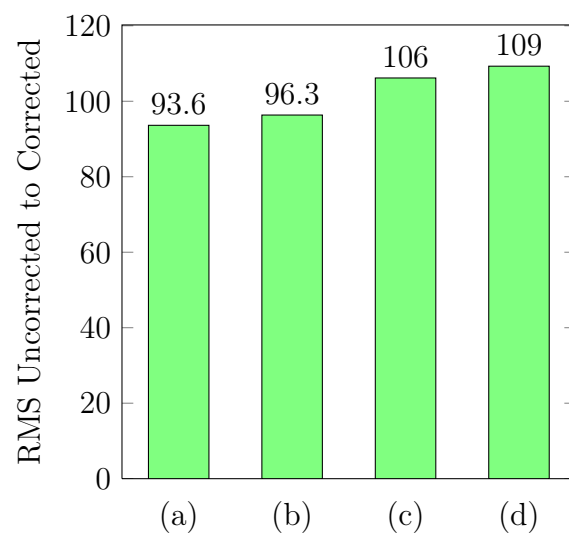


Figure 4.16: Comparison of the results with incremental activation of the post-processing steps by the RMS of the uncorrected to the corrected signal (larger is better). (a) previous, (b) +PCA, (c) +LowPass, (d) +ANC

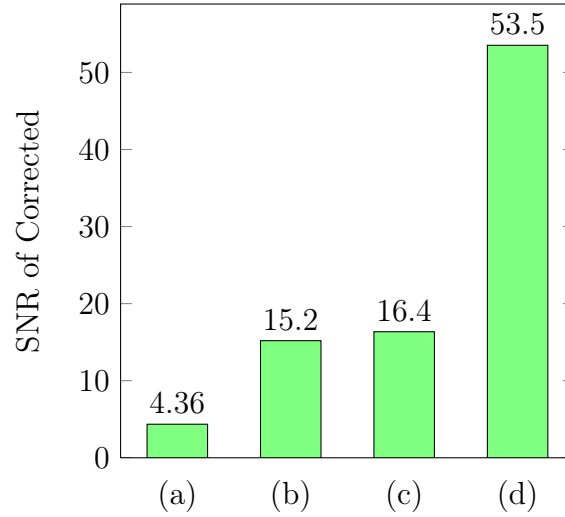


Figure 4.17: Comparison of the results with incremental activation of the post-processing steps by the SNR of the corrected signal (larger is better). (a) previous, (b) +PCA, (c) +LowPass, (d) +ANC

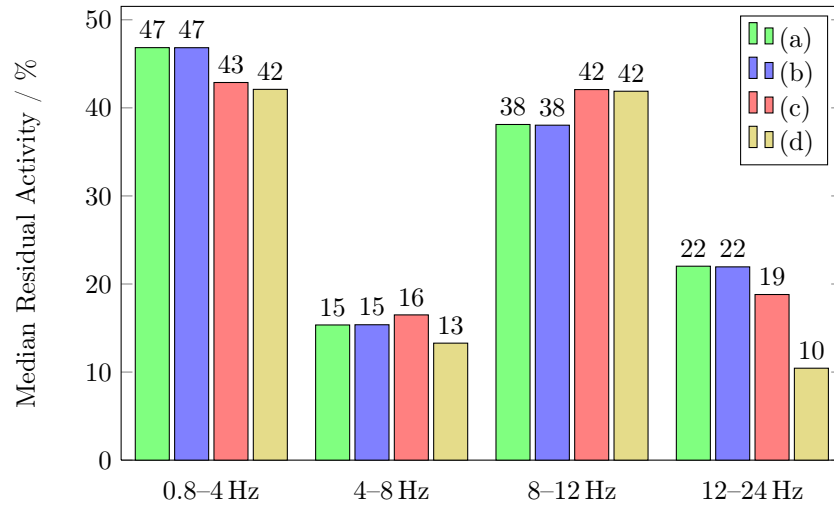


Figure 4.18: Comparison of the results with incremental activation of the post-processing steps by the median residual activity (lower is better). (a) previous, (b) +PCA, (c) +LowPass, (d) +ANC

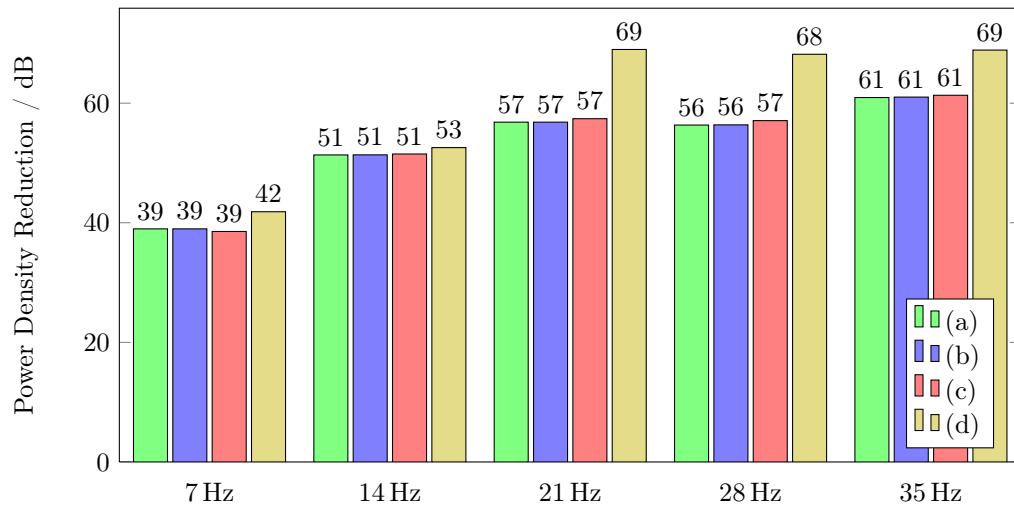


Figure 4.19: Comparison of the results with incremental activation of the post-processing steps by the power density reduction at slice frequency harmonics (larger is better). (a) previous, (b) +PCA, (c) +LowPass, (d) +ANC

4.5 Comparison with Post-Processing

Finally, all pre-processing and template generation improvements and all post-processing options are used in EEGfMRI and compared with [Allen et al. \(2000\)](#) and [Niazy et al. \(2005\)](#). Note that [Allen et al. \(2000\)](#) does not use PCA in post-processing. Although their low-pass filter has a cut-off frequency of 80 Hz, here it is set to 70 Hz as used by [Niazy et al. \(2005\)](#) and EEGfMRI. An exemplary section of the EEG signal as result of the EEGfMRI algorithm is shown in Fig. 4.20. The results are given in Tab. 4.4 and Figs. 4.21 to 4.26.

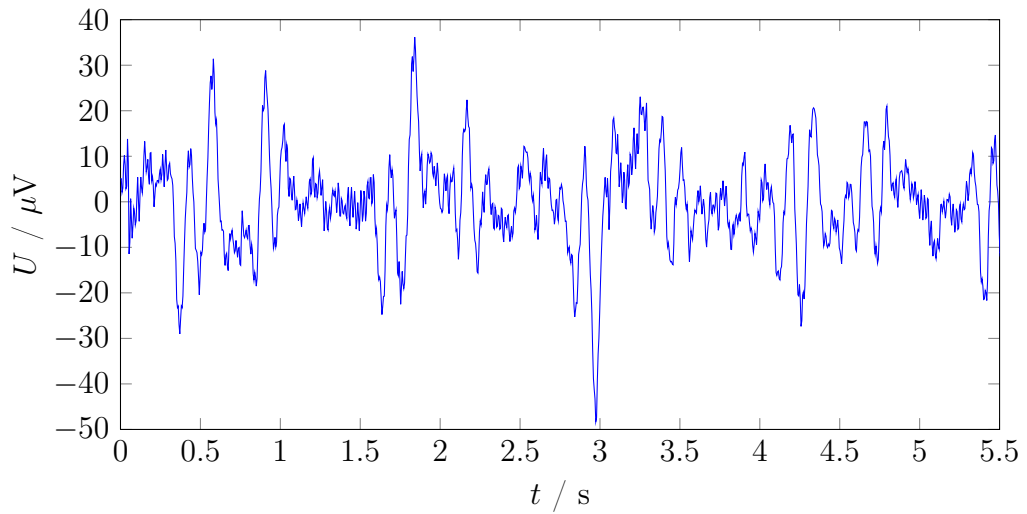


Figure 4.20: Exemplary section of the FMRIB dataset (see Sec. 4.1.1) after artifact removal with the EEGfMRI algorithm. The signal does not show any slice or volume artifacts. The residual variation is due to the BCG artifact which is not considered in this work.

All performance indicators in time-domain (median imaging artifact, RMS, SNR) show an advantage of Niazy over Allen as well as a strong improvement of EEGfMRI over both.

On the other hand, the frequency domain performance indicators show a partial deterioration in the 0.8–4 Hz and 8–12 Hz bands of the median residual activity. While these bands do not contain slice frequency harmonics (7 Hz, 14 Hz, 21 Hz, 28 Hz, ...), these are present in the 4–8 Hz and 12–24 Hz bands, which both show a noticeable improvement over Niazy.

The power density reduction at slice frequency harmonics shows a deterioration at 7 Hz and 14 Hz compared to Niazy and similar results for the higher harmonics. The reason is the same as already discussed in Sec. 4.3 that

Table 4.4: Comparison of the results of [Allen et al. \(2000\)](#), [Niazy et al. \(2005\)](#) and EEGfMRI with post-processing.

	Allen	Niazy	EEGfMRI
Median Imaging Artifact (μV)	71.0	64.9	54.8
RMS Corrected to Unimpaired	0.979	0.922	0.840
RMS Uncorrected to Corrected	93.7	99.6	109
SNR of Corrected	4.17 (11)	11.9 (9)	53.5 (6)
Median Residual Activity			
0.8 – 4.0 Hz	28 %	29 %	42 %
4.0 – 8.0 Hz	15 %	20 %	13 %
8.0 – 12.0 Hz	45 %	33 %	42 %
12.0 – 24.0 Hz	25 %	23 %	10 %
Power Density at Slice Frequency			
1: 7.00 Hz	-52 dB	-52 dB	-42 dB
2: 14.00 Hz	-56 dB	-57 dB	-53 dB
3: 21.00 Hz	-68 dB	-68 dB	-69 dB
4: 28.00 Hz	-69 dB	-70 dB	-68 dB
5: 35.00 Hz	-67 dB	-68 dB	-69 dB

EEGfMRI spectrum does not show deep notches at slice frequency harmonics but an even form.

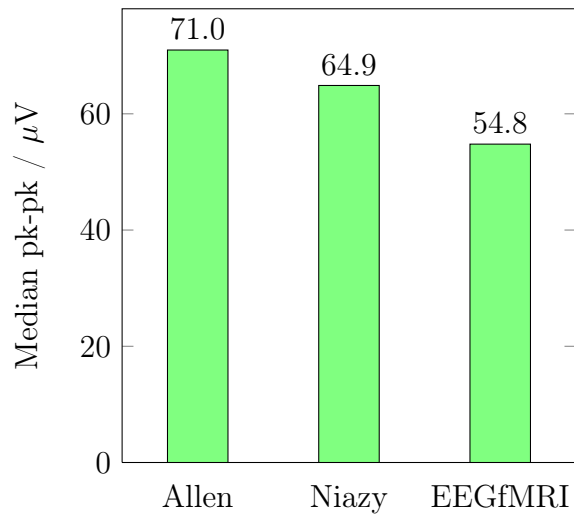


Figure 4.21: Comparison of the results of [Allen et al. \(2000\)](#), [Niazy et al. \(2005\)](#) and EEGfMRI with post-processing by the median imaging artifact (lower is better).

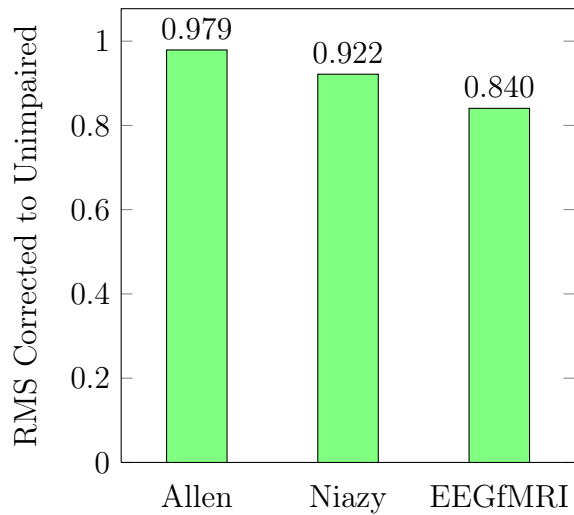


Figure 4.22: Comparison of the results of [Allen et al. \(2000\)](#), [Niazy et al. \(2005\)](#) and EEGfMRI with post-processing by the RMS of the corrected to the unimpaired signal (nearer to 1.0 is better).

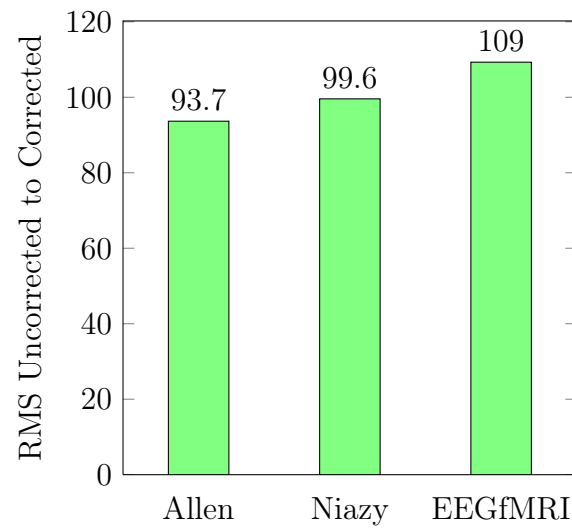


Figure 4.23: Comparison of the results of [Allen et al. \(2000\)](#), [Niazy et al. \(2005\)](#) and EEGfMRI with post-processing by the RMS of the uncorrected to the corrected signal (larger is better).

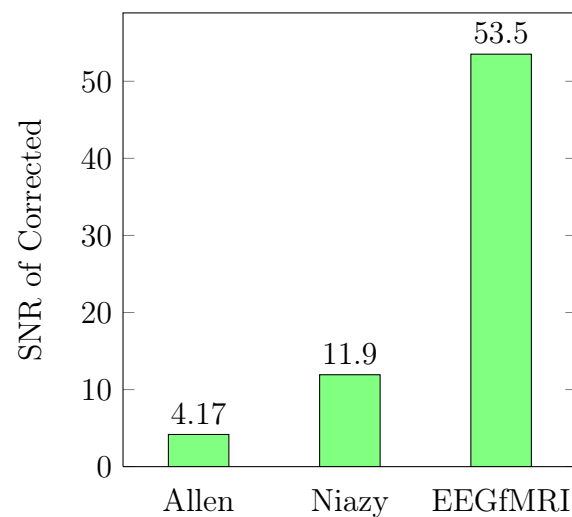


Figure 4.24: Comparison of the results of [Allen et al. \(2000\)](#), [Niazy et al. \(2005\)](#) and EEGfMRI with post-processing by the SNR of the corrected signal (larger is better).

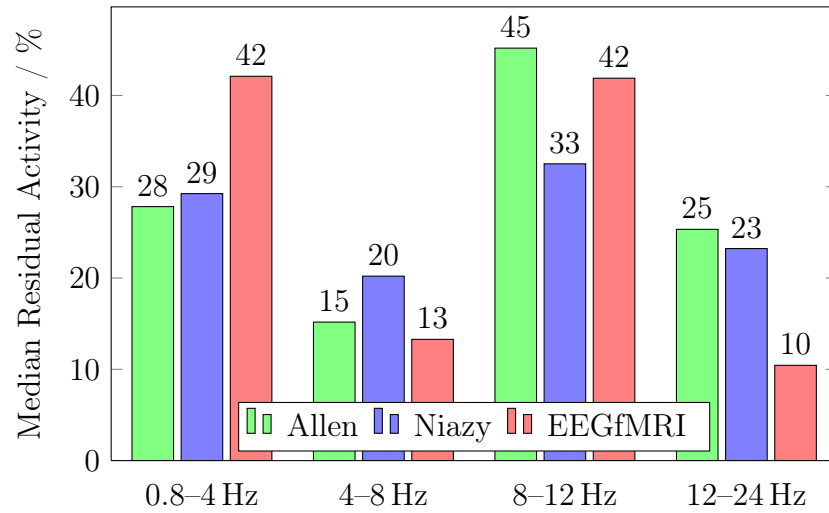


Figure 4.25: Comparison of the results of Allen et al. (2000), Niazy et al. (2005) and EEGfMRI with post-processing by the median residual activity (lower is better).

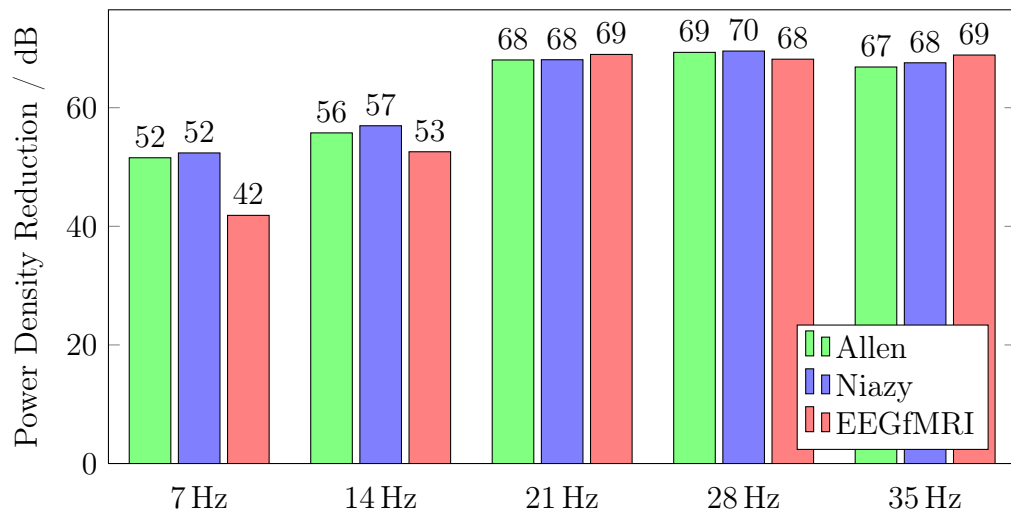


Figure 4.26: Comparison of the results of Allen et al. (2000), Niazy et al. (2005) and EEGfMRI with post-processing by the power density reduction at slice frequency harmonics (larger is better).

4.6 Pilot Dataset

In this section the same evaluation is performed with the pilot dataset. The final comparison with all pre-processing and template-generation improvements and all post-processing steps enabled is extended by the evaluation of the resulting EEG data from the built-in algorithm of the neuroConn NEURO PRAX[®] MR EEG recorder (see Sec. 4.1.2).

The artifact amplitude of the pilot dataset is much larger than the amplitude of the FMRI dataset (see Tab. 2.1, Sec. 4.1.2 and Fig. 4.1). While the FMRI dataset has a median range of $17.9 \text{ mV}_{\text{pp}}$ the pilot dataset has a nearly 23 times larger range of $408.8 \text{ mV}_{\text{pp}}$.

4.6.1 Comparison Without Post-Processing

As first step the results of the algorithms by Allen et al. (2000), Niazy et al. (2005) and the presented algorithm EEGfMRI are compared with disabled post-processing. The results are shown in Tab. 4.5 and Figs. 4.27 to 4.32.

Table 4.5: Comparison of the results of Allen et al. (2000), Niazy et al. (2005) and EEGfMRI without post-processing.

	Allen	Niazy	EEGfMRI
Median Imaging Artifact (μV)	10533	9465	11367
RMS Corrected to Unimpaired	29.4	26.6	28.0
RMS Uncorrected to Corrected	40.8	45.2	42.8
SNR of Corrected	0.00591 (20)	0.00705 (20)	0.00653 (20)
Median Residual Activity			
0.8 – 4.0 Hz	192 %	142 %	142 %
4.0 – 8.0 Hz	738 %	665 %	677 %
8.0 – 12.0 Hz	1331 %	1146 %	1132 %
12.0 – 24.0 Hz	2934 %	2830 %	2920 %
Power Density at Slice Frequency			
1: 12.50 Hz	-62 dB	-69 dB	-69 dB
2: 25.00 Hz	-55 dB	-61 dB	-59 dB
3: 37.50 Hz	-54 dB	-63 dB	-59 dB
4: 50.00 Hz	-53 dB	-63 dB	-57 dB
5: 62.50 Hz	-51 dB	-63 dB	-56 dB

Niazy shows better results than Allen in all performance indicators. Although EEGfMRI was configured as close as possible to Niazy, it shows slightly worse results than Niazy.

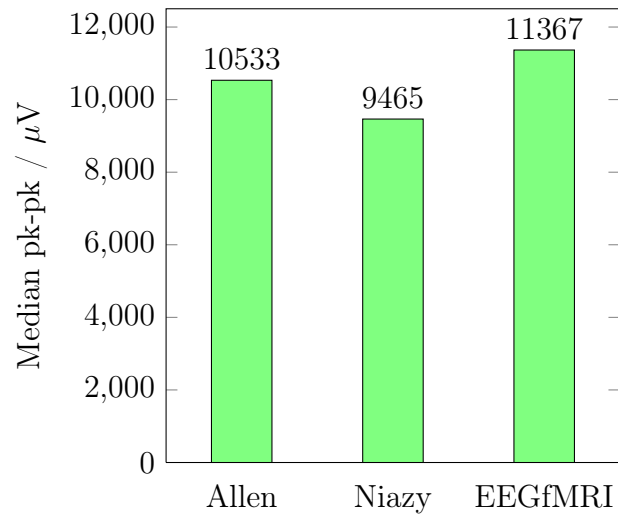


Figure 4.27: Comparison of the results of [Allen et al. \(2000\)](#), [Niazy et al. \(2005\)](#) and EEGfMRI without post-processing by the median imaging artifact (lower is better).

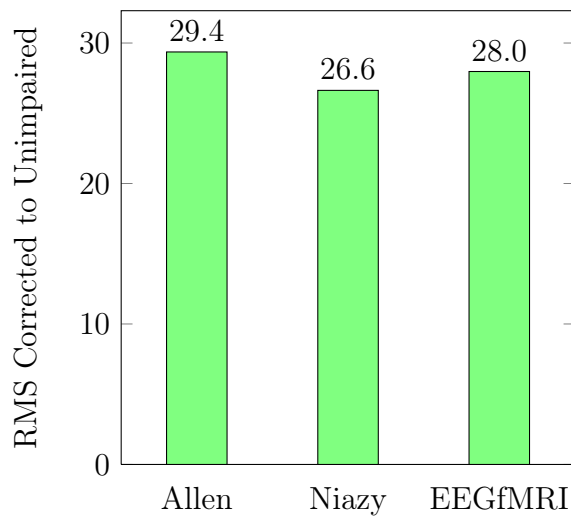


Figure 4.28: Comparison of the results of [Allen et al. \(2000\)](#), [Niazy et al. \(2005\)](#) and EEGfMRI without post-processing by the RMS of the corrected to the unimpaired signal (nearer to 1.0 is better).

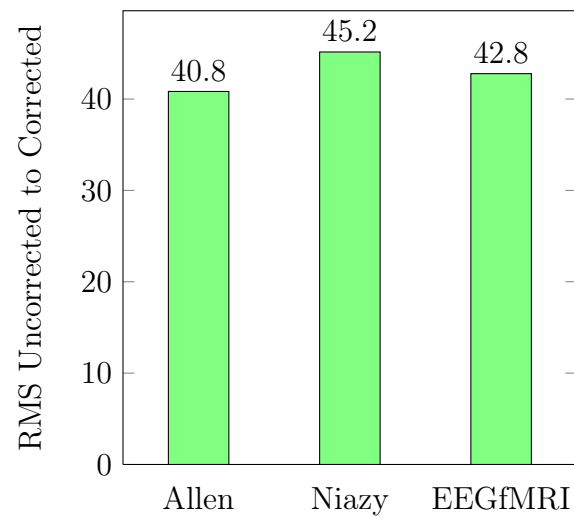


Figure 4.29: Comparison of the results of [Allen et al. \(2000\)](#), [Niazy et al. \(2005\)](#) and EEGfMRI without post-processing by the RMS of the uncorrected to the corrected signal (larger is better).

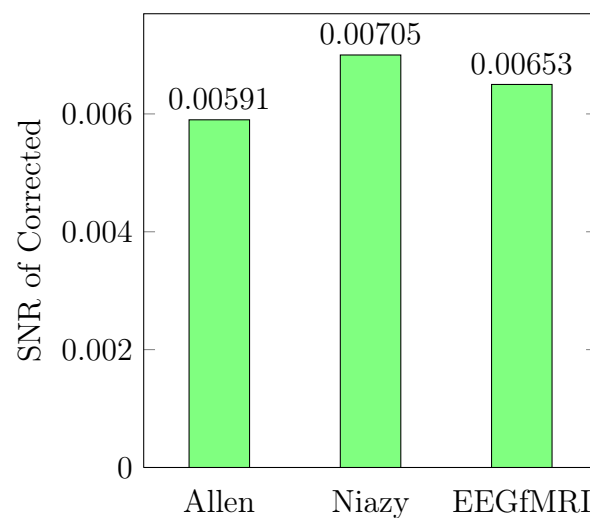


Figure 4.30: Comparison of the results of [Allen et al. \(2000\)](#), [Niazy et al. \(2005\)](#) and EEGfMRI without post-processing using the SNR of the corrected signal (larger is better).

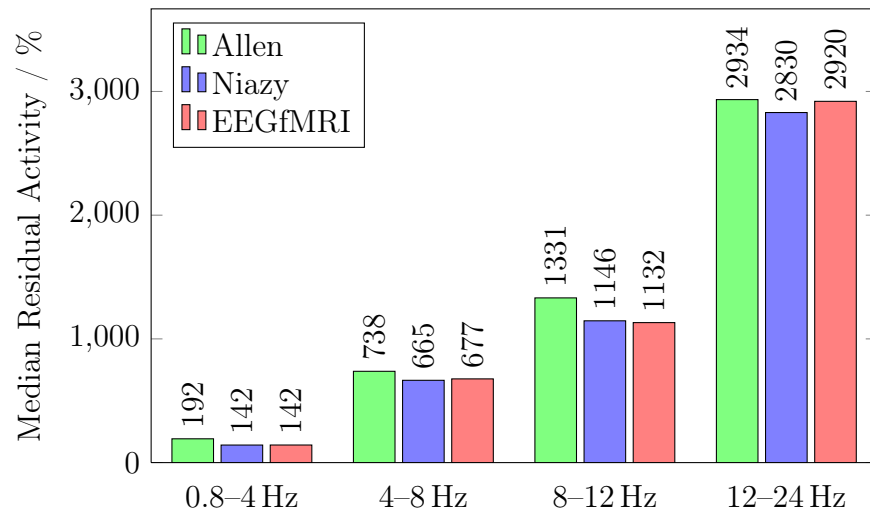


Figure 4.31: Comparison of the results of Allen et al. (2000), Niazy et al. (2005) and EEGfMRI without post-processing using median residual activity (lower is better).

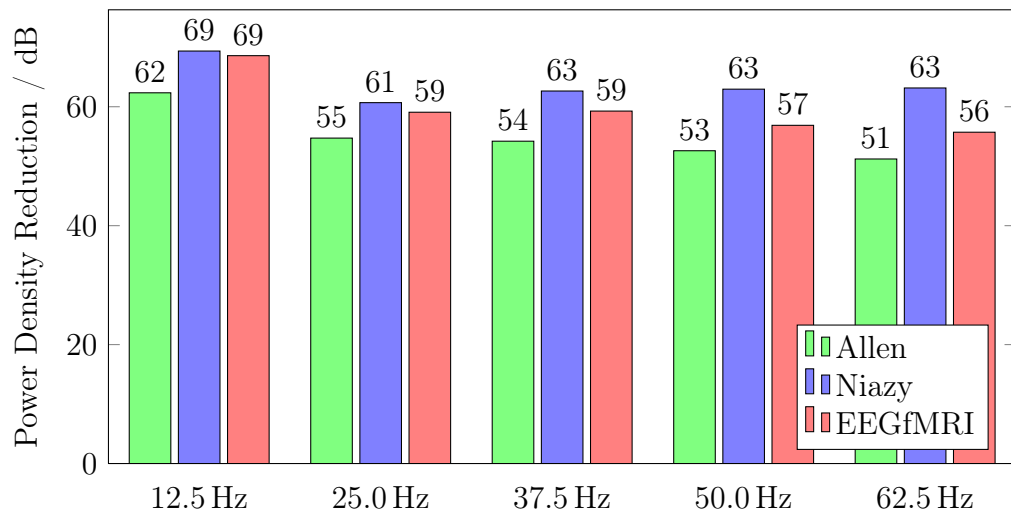


Figure 4.32: Comparison of the results of Allen et al. (2000), Niazy et al. (2005) and EEGfMRI without post-processing using the power density reduction at slice frequency harmonics (larger is better).

4.6.2 Incremental Activation of Pre-Processing and Template Generation Improvements

In the next step the pre-processing and template generation improvements are enabled incrementally for the EEGfMRI algorithm. The same abbreviations as in Sec. 4.3 are used. Note that the MR sequence used for the pilot dataset does not employ volume gaps, therefore the option `InterpolateVolGaps` is not considered. On the other hand, the data does show volume artifacts, thus the option `RemoveVolumeArt` is evaluated.

- (a) `raw`: The results from the previous step are repeated as reference.
- (b) `+PreFilter`: Using a 1 Hz high-pass pre-filter deteriorates the results according to the time-domain data. The median residual activity shows slight improvement. The power density reduction at slice frequency harmonics shows large deterioration by as much as 10 dB.
- (c) `+Upsample0.5`: Correcting the interpolation error shows an improvement in most numbers back to a level without the pre-filter. Switching off the pre-filter for this and the next steps has ambiguous effects, but generally does not give better results.
- (d) `+AlignSubSample`: The alignment of all slice period to a reference period with sub-sample resolution shows a large improvement in all time-domain values. In contrast, the median residual activity slightly deteriorates in the 4–8 Hz band. On the other hand, the power density reduction at slice frequency harmonics is much improved.
- (e) `+RemoveVolumeArt`: Removing the volume artifact shows an improvement in all values.
- (f) `+AvgArtWghtFARM`: Using best-fit slices for averaging again leads to a strong reduction of the artifacts as shown by the time-domain values. The frequency domain performance indicator “median residual activity” shows a large improvement while the power density reduction at slice frequency harmonics show a large deterioration.

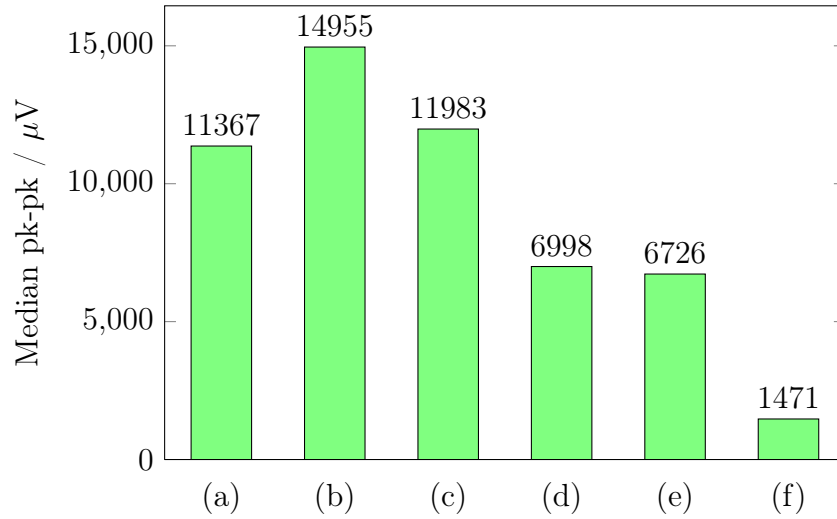


Figure 4.33: Comparison of the results with incremental activation of the pre-processing and template generation improvements by the median imaging artifact (lower is better). (a) raw, (b) +PreFilter, (c) +Upsample0.5, (d) +AlignSubSample, (e) +RemoveVolumeArt, (f) +AvgArtWghtFARM

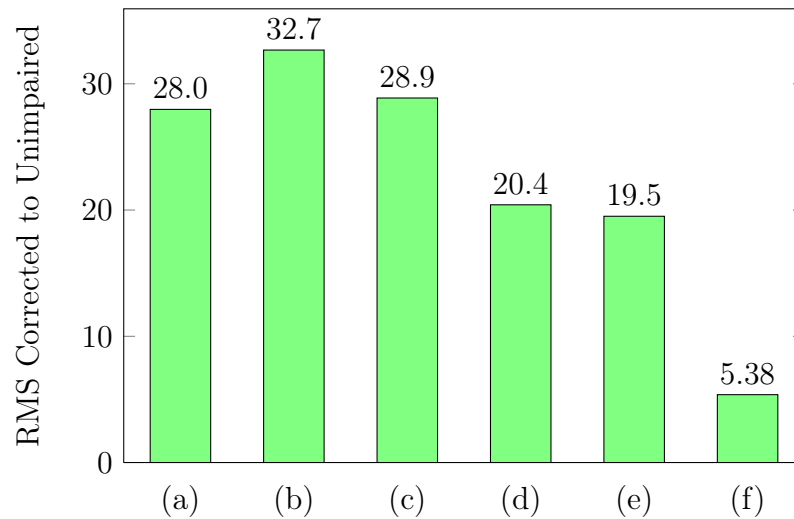


Figure 4.34: Comparison of the results with incremental activation of the pre-processing and template generation improvements by the RMS of the corrected to the unimpaired signal (nearer to 1.0 is better). (a) raw, (b) +PreFilter, (c) +Upsample0.5, (d) +AlignSubSample, (e) +RemoveVolumeArt, (f) +AvgArtWghtFARM

Table 4.6: Comparison of the results with incremental activation of the pre-processing and template generation improvements.

	(a)	(b)	(c)	(d)	(e)	(f)
(a) raw						
(b) +PreFilter						
(c) +Upsample0.5						
(d) +AlignSubSample						
(e) +RemoveVolumeArt						
(f) +AvgArtWghtFARM						
Median Imaging Artifact (μV)	11367	14955	11983	6998	6726	1471
RMS Corrected to Unimpaired	28.0	32.7	28.9	20.4	19.5	5.38
RMS Uncorrected to Corrected	42.8	36.6	41.4	66.1	74.1	236
SNR of Corrected	0.00653 (20)	0.00552 (20)	0.00616 (20)	0.0134 (20)	0.0198 (20)	0.177 (20)
Median Residual Activity						
0.8 – 4.0 Hz	142 %	139 %	151 %	151 %	138 %	71 %
4.0 – 8.0 Hz	677 %	658 %	681 %	688 %	668 %	214 %
8.0 – 12.0 Hz	1132 %	1120 %	1161 %	1148 %	1131 %	383 %
12.0 – 24.0 Hz	2920 %	2764 %	2858 %	2839 %	2699 %	882 %
Power Density at Slice Frequency						
1: 12.50 Hz	-69 dB	-61 dB	-64 dB	-77 dB	-83 dB	-70 dB
2: 25.00 Hz	-59 dB	-51 dB	-54 dB	-65 dB	-67 dB	-55 dB
3: 37.50 Hz	-59 dB	-49 dB	-52 dB	-66 dB	-69 dB	-56 dB
4: 50.00 Hz	-57 dB	-47 dB	-50 dB	-69 dB	-71 dB	-59 dB
5: 62.50 Hz	-56 dB	-45 dB	-48 dB	-71 dB	-73 dB	-61 dB

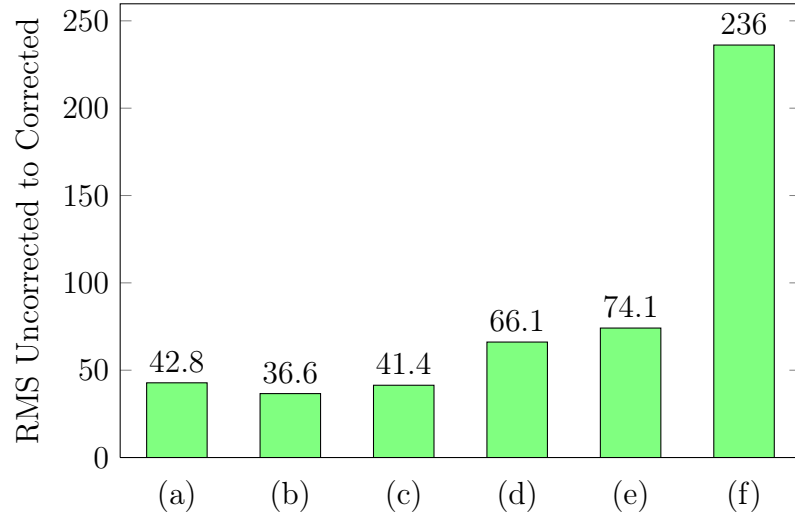


Figure 4.35: Comparison of the results with incremental activation of the pre-processing and template generation improvements by the RMS of the uncorrected to the corrected signal (larger is better). (a) raw, (b) +PreFilter, (c) +Upsample0.5, (d) +AlignSubSample, (e) +RemoveVolumeArt, (f) +AvgArtWghtFARM

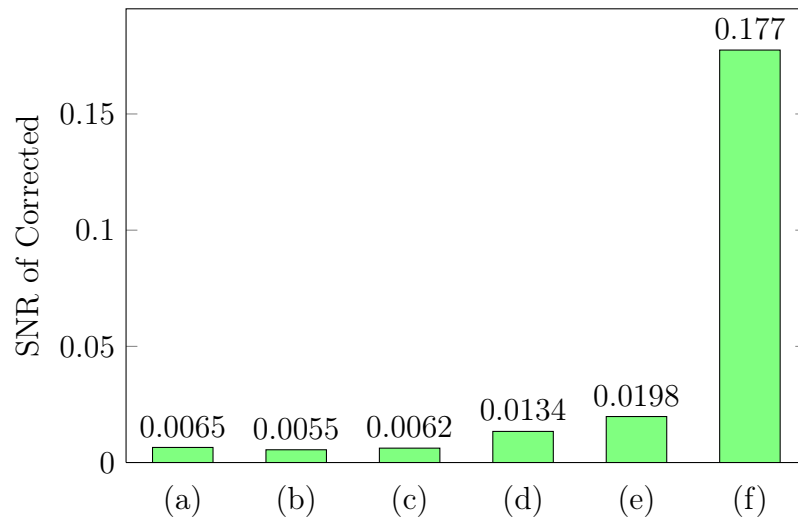


Figure 4.36: Comparison of the results with incremental activation of the pre-processing and template generation improvements by the SNR of the corrected signal (larger is better). (a) raw, (b) +PreFilter, (c) +Upsample0.5, (d) +AlignSubSample, (e) +RemoveVolumeArt, (f) +AvgArtWghtFARM

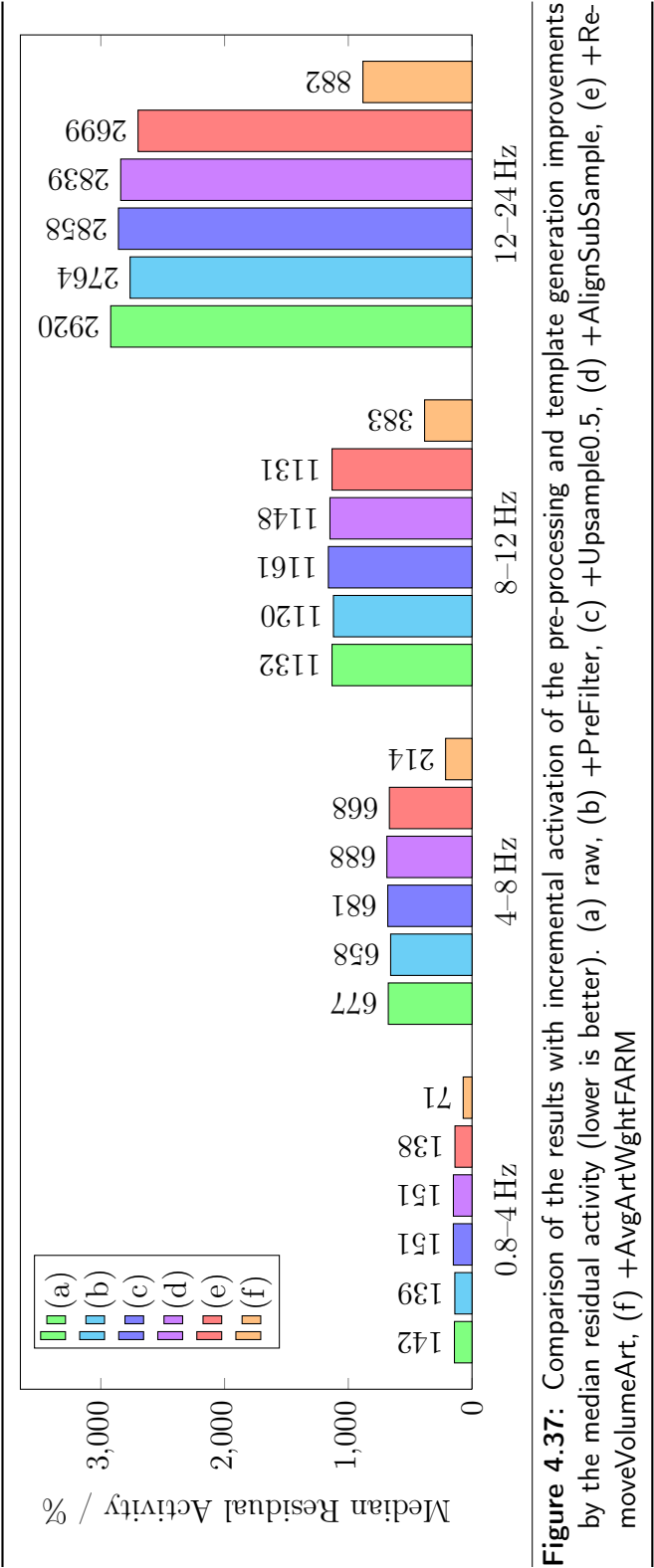


Figure 4.37: Comparison of the results with incremental activation of the pre-processing and template generation improvements by the median residual activity (lower is better). (a) raw, (b) +PreFilter, (c) +Upsample0.5, (d) +AlignSubSample, (e) +Re-moveVolumeArt, (f) +AvgArtWghtFARM

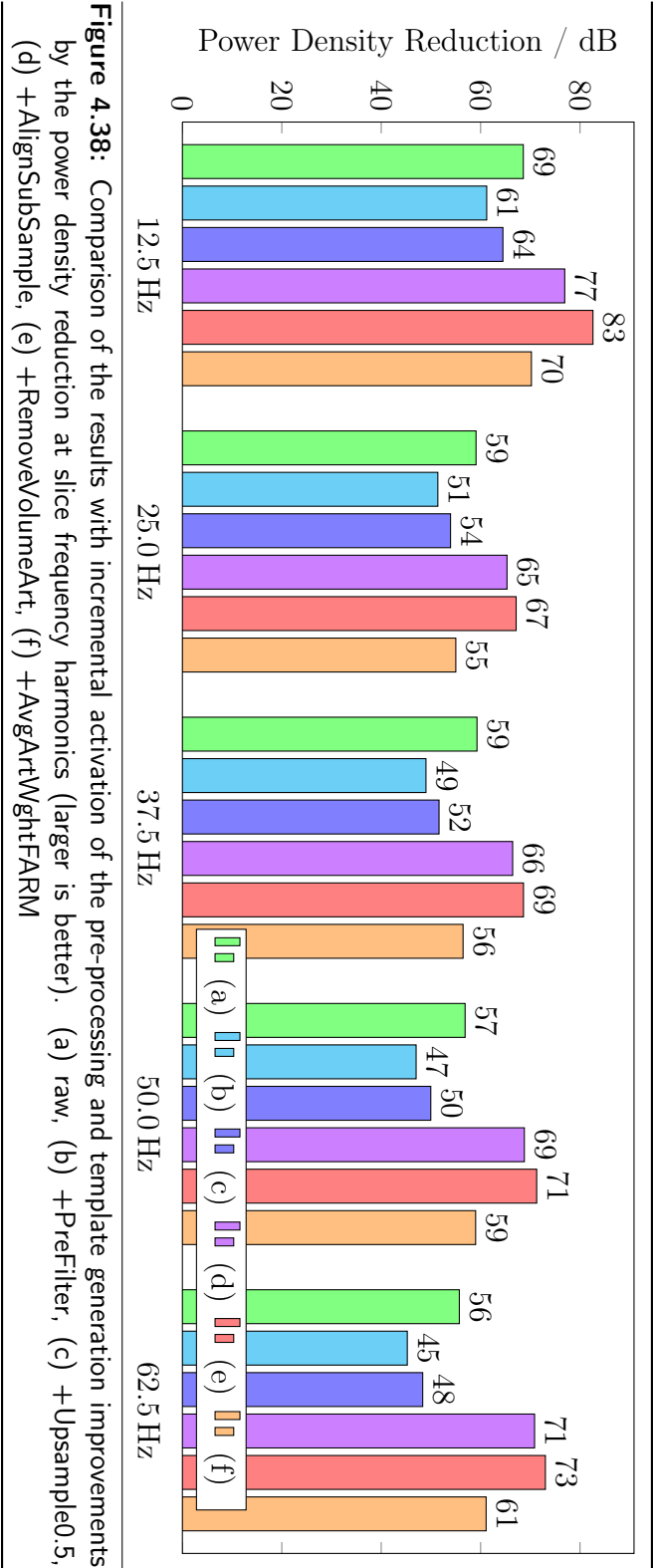


Figure 4.38: Comparison of the results with incremental activation of the pre-processing and template generation improvements by the power density reduction at slice frequency harmonics (larger is better). (a) raw, (b) +PreFilter, (c) +Upsample0.5, (d) +AlignSubSample, (e) +RemoveVolumeArt, (f) +AvgArtWghttFARM

4.6.3 Incremental Activation of Post-Processing Steps

After all pre-processing and template generation improvements are enabled, the three post-processing steps PCA (OBS), 70 Hz low-pass and adaptive noise cancellation are activated.

Table 4.7: Comparison of the results with incremental activation of the post-processing steps.

	(a)	(b)	(c)	(d)
(a) previous				
(b) +PCA				
(c) +LowPass				
(d) +ANC				
Median Imaging Artifact (μV)	1471	1147	417	221
RMS Corrected to Unimpaired	5.38	4.96	3.66	2.73
RMS Uncorrected to Corrected	236	259	363	522
SNR of Corrected	0.177 (20)	0.240 (20)	0.906 (19)	35.5 (16)
Median Residual Activity				
0.8 – 4.0 Hz	71 %	71 %	86 %	83 %
4.0 – 8.0 Hz	214 %	214 %	234 %	220 %
8.0 – 12.0 Hz	383 %	382 %	394 %	208 %
12.0 – 24.0 Hz	882 %	877 %	822 %	325 %
Power Density at Slice Frequency				
1: 12.50 Hz	-70 dB	-70 dB	-70 dB	-85 dB
2: 25.00 Hz	-55 dB	-55 dB	-56 dB	-78 dB
3: 37.50 Hz	-56 dB	-57 dB	-56 dB	-79 dB
4: 50.00 Hz	-59 dB	-59 dB	-58 dB	-84 dB
5: 62.50 Hz	-61 dB	-61 dB	-63 dB	-89 dB

(a) previous: The results of the previous section are repeated for reference.

(b) PCA: Removing the strongest principal components related to the artifact signal shows an improvement in all time-domain values but no change in the frequency domain performance indicators.

(c) LowPass: Filtering the EEG data with a 70 Hz low-pass results in strong improvements in all time domain performance indicators. On the other hand the median residual activity slightly deteriorates in the frequency bands 0.8–4 Hz, 4–8 Hz and 8–12 Hz.

(d) ANC: Adaptive noise cancellation leads to a strong improvement in all values.

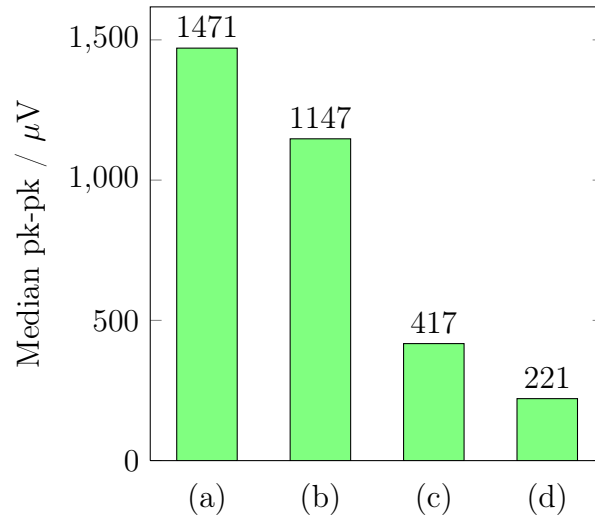


Figure 4.39: Comparison of the results with incremental activation of the post-processing steps by the median imaging artifact (lower is better). (a) previous, (b) +PCA, (c) +LowPass, (d) +ANC

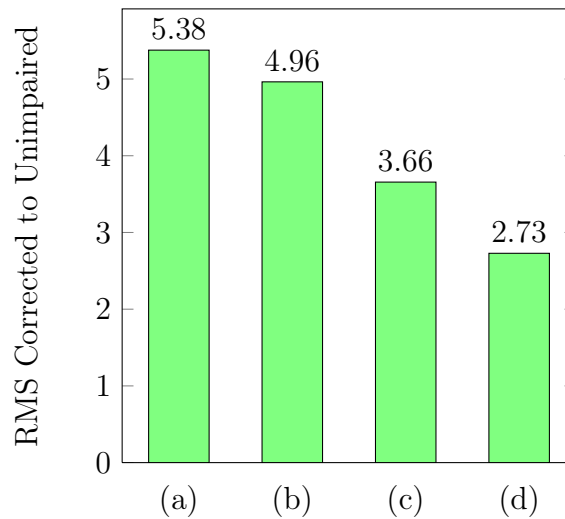


Figure 4.40: Comparison of the results with incremental activation of the post-processing steps by the RMS of the corrected to the unimpaired signal (nearer to 1.0 is better). (a) previous, (b) +PCA, (c) +LowPass, (d) +ANC

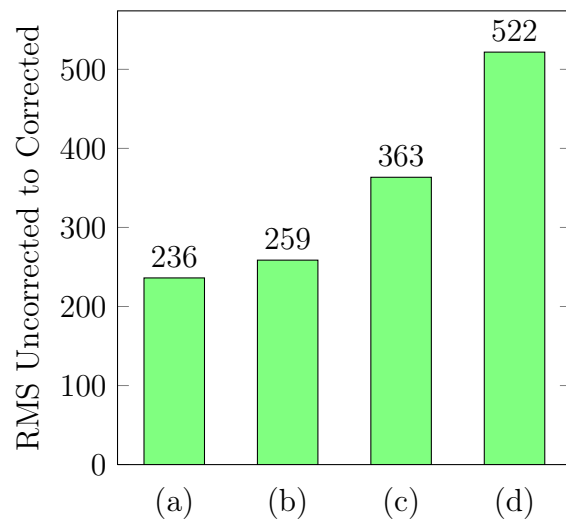


Figure 4.41: Comparison of the results with incremental activation of the post-processing steps by the RMS of the uncorrected to the corrected signal (larger is better). (a) previous, (b) +PCA, (c) +LowPass, (d) +ANC

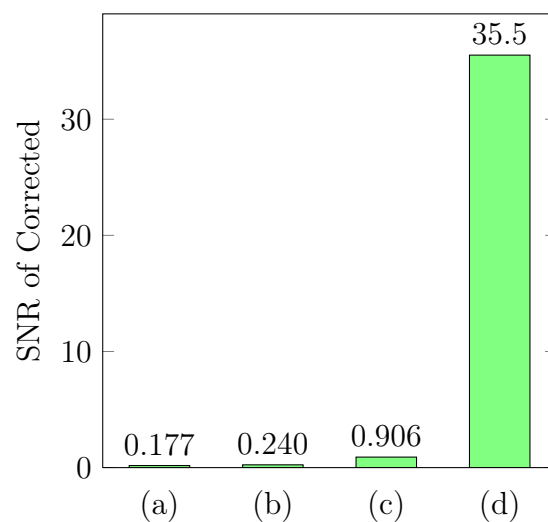


Figure 4.42: Comparison of the results with incremental activation of the post-processing steps by the SNR of the corrected signal (larger is better). (a) previous, (b) +PCA, (c) +LowPass, (d) +ANC

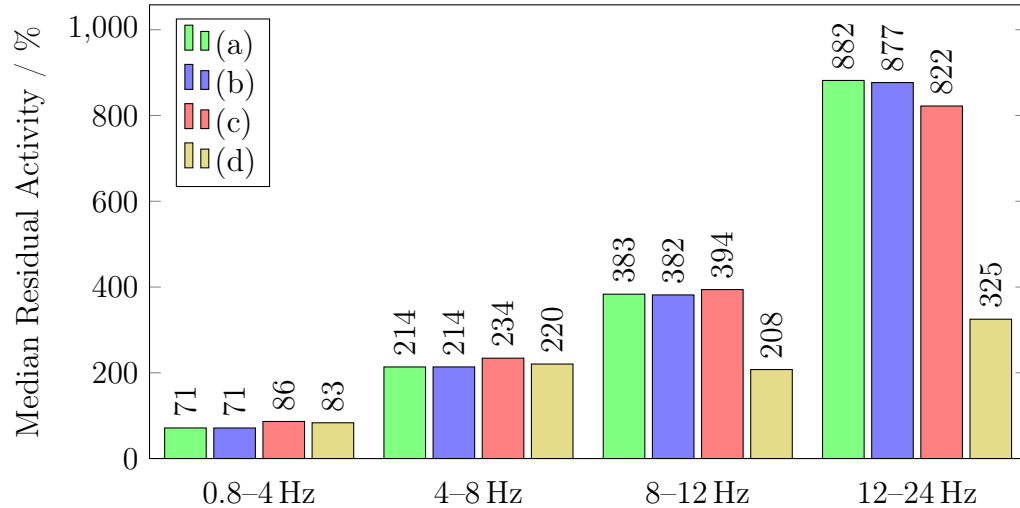


Figure 4.43: Comparison of the results with incremental activation of the post-processing steps by the median residual activity (lower is better). (a) previous, (b) +PCA, (c) +LowPass, (d) +ANC

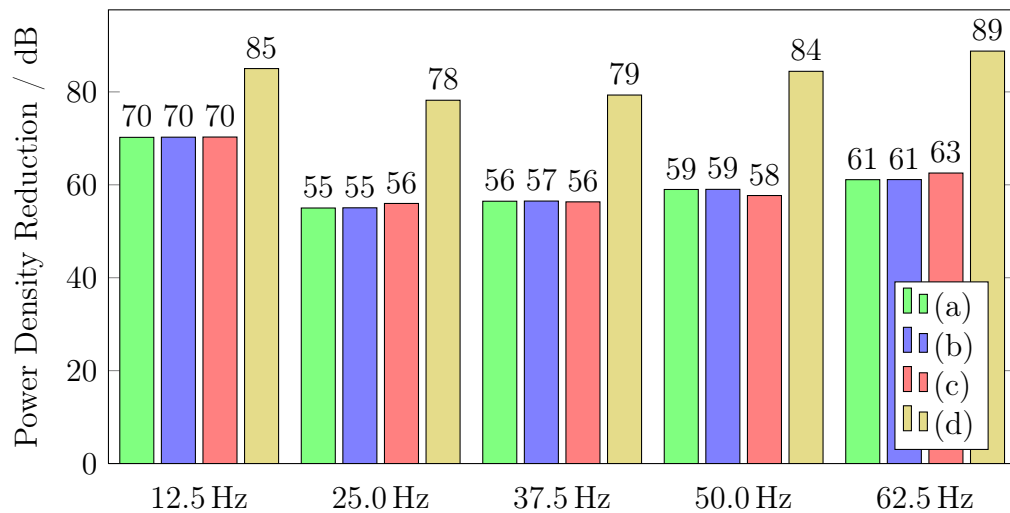


Figure 4.44: Comparison of the results with incremental activation of the post-processing steps by the power density reduction at slice frequency harmonics (larger is better). (a) previous, (b) +PCA, (c) +LowPass, (d) +ANC

4.6.4 Comparison with Post-Processing

Finally, the result of EEGfMRI with all pre-processing and template generation improvements and all post-processing steps enabled are compared with Allen, Niazy and NeuroPrax. The results of NeuroPrax show strong oscillations directly after the onset of fMRI acquisition for approximately 2 sec. This period of badly corrected EEG data is excluded from further evaluation.

Figure 4.45 shows an exemplary section of the EEG data after correction using the EEGfMRI algorithm. The signal shows considerable residual artifacts with the slice frequency of 12.5 Hz as well as a strong 1 Hz component. The latter is twice the volume repetition frequency (TR=2 s, i.e., 0.5 Hz) and is present in all artifact corrected signals.

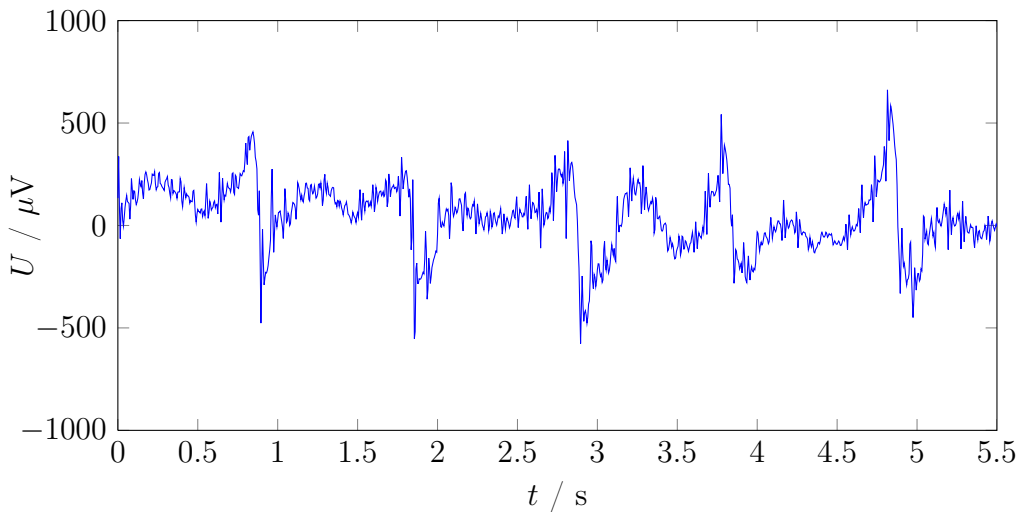


Figure 4.45: Exemplary section of the pilot dataset (see Sec. 4.1.2) after artifact removal with the EEGfMRI algorithm. The signal has considerable residual artifacts.

The results of Niazy are worse than Allen’s in the time-domain performance indicators and the 8–12 Hz and 12–24 Hz bands of the median residual activity. The power density reduction at slice frequency harmonics shows mixed results.

Compared to Niazy, EEGfMRI has nearly ten times less (residual) median imaging artifact and five times better ratio of the RMS of the corrected to the RMS of the unimpaired signal as well as five times better ratio of the RMS of the uncorrected to the RMS of the corrected signal. The SNR is more than 200 times better compared to next-best Allen. The frequency-domain perfor-

Table 4.8: Comparison of the results of [Allen et al. \(2000\)](#), [Niazy et al. \(2005\)](#), EEGfMRI and NeuroPrax with post-processing.

	Allen	Niazy	EEGfMRI	NeuroPrax
Median Imaging Artifact (μV)	1294	2125	221	1989
RMS Corrected to Unimpaired	10.7	13.5	2.73	10.3
RMS Uncorrected to Corrected	156	102	522	146
SNR of Corrected	0.148 (20)	0.0458 (20)	35.5 (16)	0.125 (20)
Median Residual Activity				
0.8 – 4.0 Hz	203 %	199 %	83 %	323 %
4.0 – 8.0 Hz	794 %	707 %	220 %	469 %
8.0 – 12.0 Hz	756 %	1035 %	208 %	1111 %
12.0 – 24.0 Hz	1505 %	1814 %	325 %	2263 %
Power Density at Slice Frequency				
1: 12.50 Hz	-77 dB	-82 dB	-85 dB	-64 dB
2: 25.00 Hz	-77 dB	-78 dB	-78 dB	-60 dB
3: 37.50 Hz	-74 dB	-75 dB	-79 dB	-52 dB
4: 50.00 Hz	-76 dB	-73 dB	-84 dB	-54 dB
5: 62.50 Hz	-78 dB	-73 dB	-89 dB	-54 dB

mance indicator of median residual activity also shows strong improvement as well as the power density reduction at slice frequency harmonics.

NeuroPrax has similar results in most performance indicators to Allen and Niazy. In the frequency domain values its results are considerably worse, e.g., 13–24 dB less reduction at slice frequency harmonics.

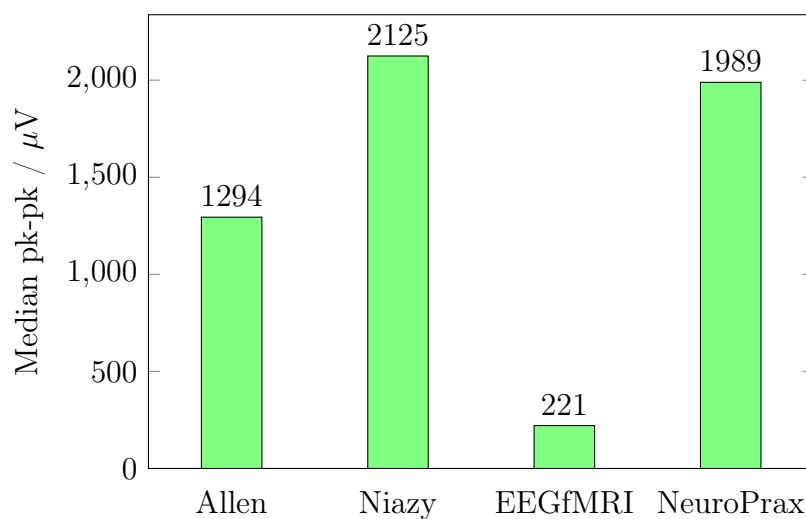


Figure 4.46: Comparison of the results of [Allen et al. \(2000\)](#), [Niazy et al. \(2005\)](#), EEGfMRI and NeuroPrax with post-processing by the median imaging artifact (lower is better).

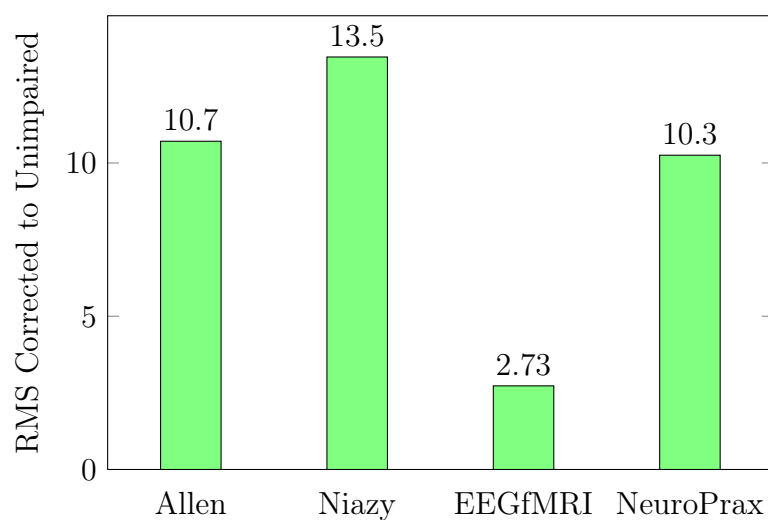


Figure 4.47: Comparison of the results of [Allen et al. \(2000\)](#), [Niazy et al. \(2005\)](#), EEGfMRI and NeuroPrax with post-processing by the RMS of the corrected to the unimpaired signal (nearer to 1.0 is better).

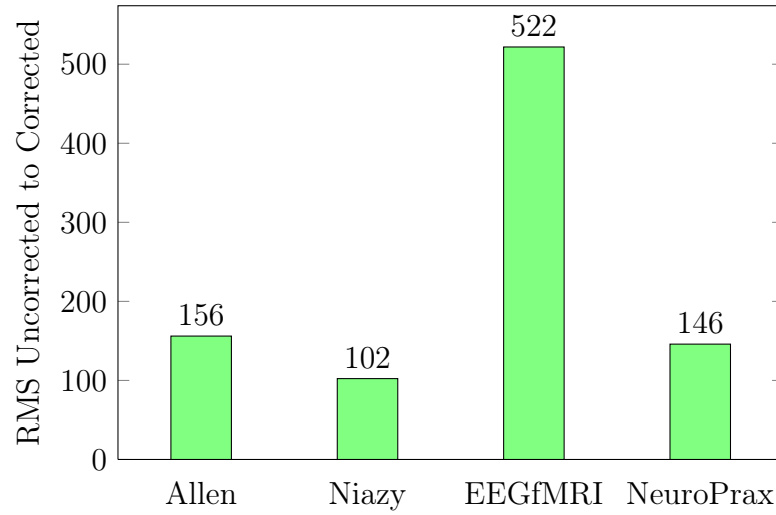


Figure 4.48: Comparison of the results of [Allen et al. \(2000\)](#), [Niazy et al. \(2005\)](#), EEGfMRI and NeuroPrax with post-processing by the RMS of the uncorrected to the corrected signal (larger is better).

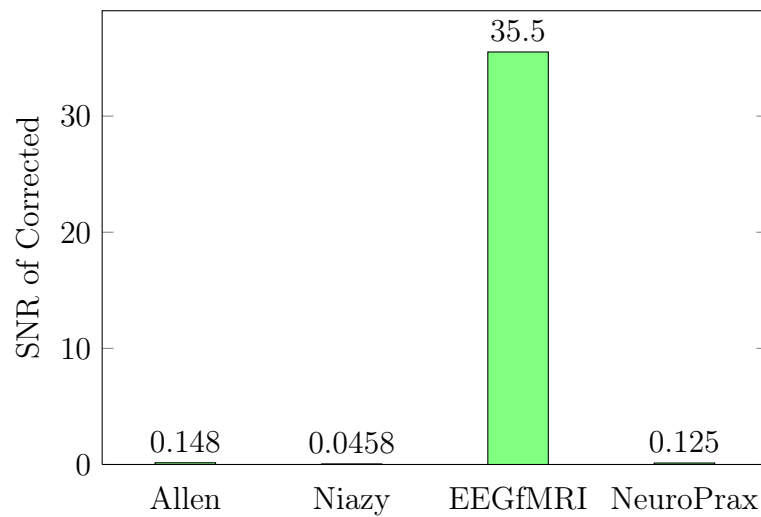


Figure 4.49: Comparison of the results of [Allen et al. \(2000\)](#), [Niazy et al. \(2005\)](#), EEGfMRI and NeuroPrax with post-processing by the SNR of the corrected signal (larger is better).

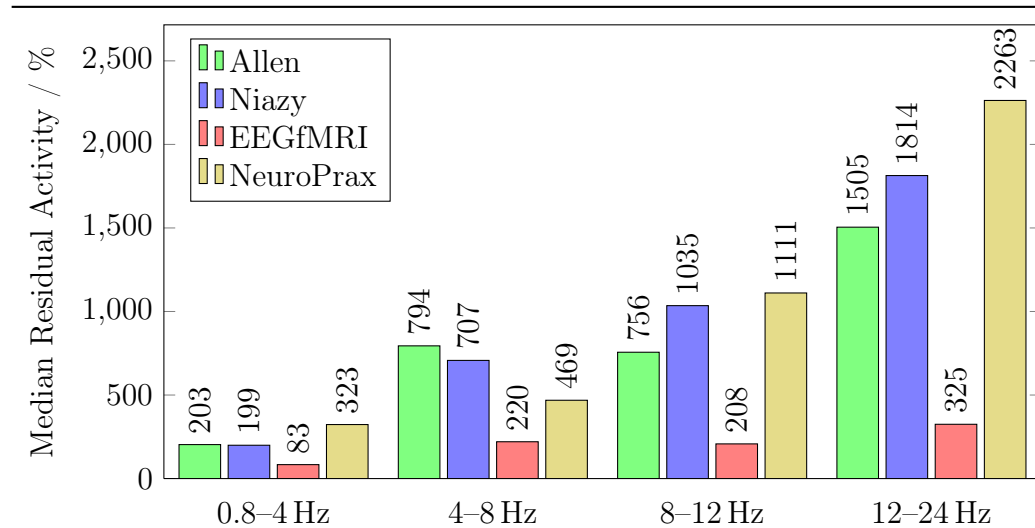


Figure 4.50: Comparison of the results of [Allen et al. \(2000\)](#), [Niazy et al. \(2005\)](#), EEGfMRI and NeuroPrax with post-processing by the median residual activity (lower is better).

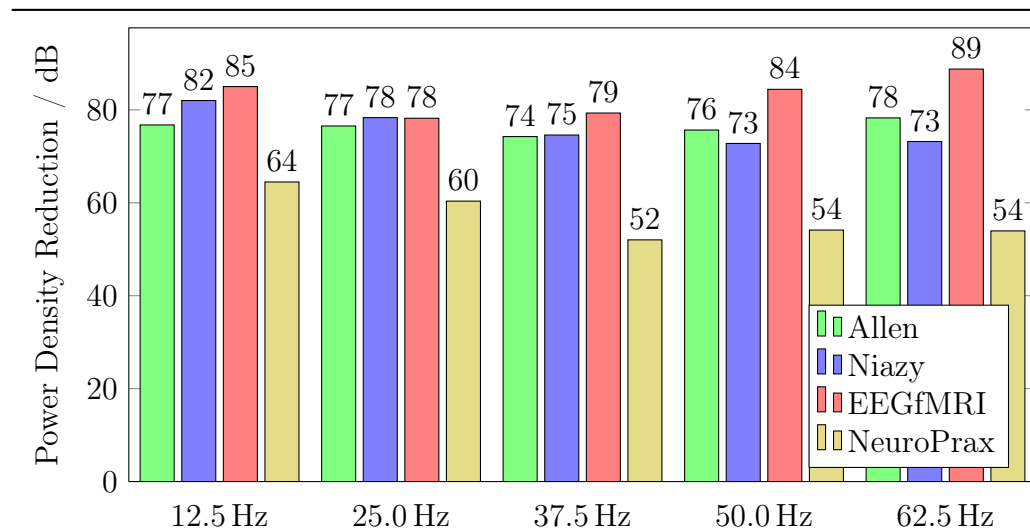


Figure 4.51: Comparison of the results of [Allen et al. \(2000\)](#), [Niazy et al. \(2005\)](#), EEGfMRI and NeuroPrax with post-processing by the power density reduction at slice frequency harmonics (larger is better).

4.7 Discussion

In the previous chapter 3 the flexible artifact correction and evaluation toolbox “FACET” was presented. It was used to implement an optimum correction algorithm called “EEGfMRI” for the demonstration of a best-practice on artifact correction. The details on the configuration and settings are summarized in Tab. 4.9 and also used in Lst. 3.2, Lst. 3.5, Fig. 3.5 and CleanEx1.m.

In this chapter, the artifact correction algorithm EEGfMRI was evaluated using two independent datasets. The results were compared to the algorithms by Allen et al. (2000), Niazy et al. (2005) and (partly) NeuroPrax. The algorithm by Niazy et al. (2005) was used as starting point to which six improvements in the pre-processing and template generation were introduced. These were investigated with deactivated post-processing to have a clear view on their effect.

The time-domain performance indicators show a strong reduction of the residual artifact amplitude and power for the FMRIB dataset. On the other hand, the frequency-domain performance indicators seem to point at a deterioration caused by the improvements. A closer look at the spectrum of the resulting EEG data shows that originally deep notches at slice frequency harmonics are removed. This means that a flat spectrum is achieved, i.e. the real EEG signal is conserved.

The main improvements are achieved by two facilities. Firstly, the alignment of slice periods with sub-sample resolution to a reference slice. And secondly, by the selection of slices with highest correlation to a reference slice before the calculation of the slice template (van der Meer et al., 2010).

In the post-processing, the low-pass with a 70 Hz cut-off frequency poses the largest impact on the signal amplitude with both datasets, because it removes the high-frequency components which largely contribute to the signal range. The PCA introduced by Niazy et al. (2005) shows small effect for the FMRIB dataset but better for the pilot dataset.

Comparing the results depending on the dataset reveals a 23 times larger amplitude range of the raw pilot dataset compared to the FMRIB dataset. This ratio is reduced to 4 after the correction with EEGfMRI. If all post-processing is deactivated, the Allen algorithm gives better results with the FMRIB dataset, while the pilot dataset is better corrected by Niazy. For the EEGfMRI algorithm, the strongest improvements are achieved by the alignment of slice periods with sub-sample resolution (“AlignSubSample”) and by the selection of best-fit slices for the template generation (“AvgArtWght-

Table 4.9: Summary of characteristics and settings of the evaluated algorithms.

	Allen	Niazy	EEGfMRI
Pre-Processing			
Pre-Filter			1 Hz Gaussian HP
Interpolation	20x ^a	10x	10x
Interpolation Error		✓ ^b	
Align Slices	✓ ^c	✓	✓
Align Sub-Sample			✓
Remove Volume Artifact			✓
Template Generation			
Epoch Selection for Averaging	blocks of 100, $r \geq 0.975$	sliding avg., 30 interleaved epochs	sliding avg., 30 out of 180 with highest r
Post-Processing			
PCA		✓	✓
Low-Pass	80 Hz ^d	70 Hz	70 Hz
ANC	✓	✓	✓

^aAllen et al. (2000) recorded the EEG data with a sampling rate of 5 kSps ($\hat{=}$ 200 μ s) and the triggers with a higher resolution of 10 μ s. The EEG data was interpolated to the resolution of the trigger information. In contrast, in this work the triggers have the same resolution as the EEG data, therefore it was interpolated by a factor of 10 as proposed by Niazy et al. (2005).

^bThe interpolation error leads to high-frequency oscillations in the interpolated data.

^caligned to the higher resolution trigger information, see footnote *a*

^dhere: 70 Hz, see also Sec. 4.5

FARM”) for both datasets. The pilot datasets still shows residual gradient artifacts after full correction, while the FMRIB dataset only shows BCG artifacts.

One major drawback of existing algorithms is the bad handling of subject movements, especially for EMG signals. The evaluation using the pilot dataset, which mainly contains EMG data, clearly shows these problems: The artifact removal of Allen, Niazy as well as NeuroPrax are not satisfactory. Although EEGfMRI still leaves residual gradient artifacts, the evaluation shows a considerable improvement over the other algorithms. Compared to the best of the other three, EEGfMRI has nearly six times less (residual) median imaging artifact than Allen, a nearly four times better ratio of the RMS of the corrected to the RMS of the unimpaired signal than NeuroPrax and more than three times higher ratio of the RMS of the uncorrected to the RMS of the corrected signal than Allen. The SNR is 240 times better than Allen, the median residual activity is in all four frequency bands 2.4 to 4.6 times less than that of Allen and the power reduction at slice frequency harmonics is up to 16 dB better than Niazy. This shows that EEGfMRI can cope much better with EMG signals and subject movement than the other algorithms.

In total, the presented algorithm EEGfMRI produces much better results with both datasets for the time-domain performance indicators. The frequency domain performance indicators show mixed results, although the signal spectrum reveals less notches and thus better preservation of the original EEG.

5

Summary

MULTI-modal imaging is an aspiring methodology in neuroscience. It enables research as well as clinical applications to observe brain activity with distinct approaches and allows to correlate results of both. The concurrent exertion of EEG and fMRI helps in source localization and provides deeper insight into brain functions. Currently this method is extended by the inclusion of EMG to record muscle activity.

The application of concurrent EEG, EMG and fMRI poses problems due to mutual interference. While the artifacts in fMRI data due to EEG/EMG electrodes is negligible, the fMRI gradient artifacts in the EEG/EMG data caused by electromagnetic induction (see Sec. 2.2) exceed the original EEG signal by several orders of magnitude (see Sec. 2.2.2).

To reduce the fMRI artifacts in the EEG/EMG signal, correction algorithms were published. These were summarized in Sec. 2.3. Most algorithms generate an average artifact template which is subtracted from the EEG signal.

The results of these algorithms are deteriorated due to a missing synchronization of the fMRI sequence and the EEG/EMG recording system. A second cause for deteriorated results is subject movement. However these are an inherent component of EMG recordings.

The goal of this work is to build a universal and powerful artifact correction toolbox which can cope with these problems. The toolbox should be programmed understandable, maintainable and extensible. It should include functions for the data analysis, preparation, filtering and correction and let the user combine them flexibly. The fMRI artifact should be removed to a higher degree than by the existing correction algorithms. Therefore, a dedicated evaluation framework should be provided.

5.1 Artifact Correction and Evaluation Toolbox

The artifact correction and evaluation toolbox “FACET” (see Ch. 3) is based on the algorithm by [Niazy et al. \(2005\)](#) and implemented in **Matlab**. The software re-engineering process was employed to reimplement the algorithm with the object oriented design paradigm.

Dedicated functions for the analysis of the input data and the correction of the triggers were added. The main improvements of the algorithm itself include an optional pre-filter (high-pass and low-pass) before any further processing, the correction of an interpolation error, the alignment of slice periods with sub-sample resolution before averaging, the correction of the volume artifact, a universal interface for the specification of the slices periods to average for the template generation and the interpolation of the volume gaps during template generation.

Extensibility of the toolbox is one of the design goals and is achieved with the object oriented design paradigm. The **FACET** class can be derived and extended by introducing new or overriding existing methods. The second mechanism for extensions is the configurable correction sequence which allows to execute arbitrary user functions at any point. The third point for extensions are the **Matlab** events generated at numerous points within **FACET** before, during and after the artifact correction sequence. These three mechanisms ensure that the toolbox can be augmented at any point.

Contrary to the graphical dialog by [Niazy et al. \(2005\)](#) as user interface, **FACET** is fully configured with a configuration file (precisely: with a **Mat-**

lab script). This ensures reproducible results and allows the user to add comments for explanations and rationale.

The artifact correction toolbox is complemented by a dedicated framework for the evaluation of EEG/EMG data after artifact correction. This data is characterized according to multiple performance indicators. Additionally it offers functions to automatically generate L^AT_EX code with tables and diagrams (using TikZ and PGFPlots) for direct inclusion in the user's documentation.

In total, the “FACET” toolbox provides facilities for all three: data analysis, artifact correction as well as evaluation of the results. These allow to perform the correction and iteratively optimize the settings specifically for the EEG/EMG data at hand.

The artifact correction toolkit was used to implement a best-practice algorithm called “EEGfMRI” which was employed for the correction of two different datasets. These results were evaluated with the presented evaluation framework (see Ch. 4). It shows a clear improvement over the existing algorithms.

The toolbox was presented at the OHBM 2012 as Glaser, Schöpf, Bauer, and Fischmeister (2012) with the name “FACET — a “Flexible Artefact Correction and Evaluation Toolbox” for EEG/fMRI data”. It will be available online at <http://scan.psy.univie.ac.at/> as open source software under the terms of the GNU General Public License. The archive includes documentation, examples and all scripts used for the evaluation in Ch. 4.

5.2 Future Work

The presented artifact correction toolbox and evaluation framework are extensible to ease the integration of improvements.

An interesting enhancement is the usage of the wavelet transform for the artifact correction (Doblinger, 2001). Contrary to wavelet shrinkage, which is used to remove the small signal components, here the large signal components should be removed. This can be achieved by an inverted thresholding function.

Since the EEG/EMG signals and fMRI gradient artifacts as well as the BCG are mutually statistically independent, an independent component analysis

ICA can be added to further improve the gradient template estimation before subtraction.

The post-processing features can be supplemented by non-linear filters. A median filter, which replaces every value by the median of its predecessor and successor, would thus implement a non-linear low-pass filter.

Above, the optimization of the settings specifically for the EEG/EMG data was indicated. This process can be automated by wrapping the artifact correction algorithm inside an optimization algorithm which automatically and iteratively tunes the settings towards a global optimum.

During the execution of the algorithm, an identical sequence is performed on the data of every EEG and/or EMG channel. This allows for easy parallelization using multi-core CPUs or computing clusters. Newer versions of **Matlab** also allow to transfer large computational tasks to the graphics processing unit (GPU), which are highly optimized engines for parallel processing.

The evaluation performed in Ch. 4 incrementally enabled options of the algorithm (see Sec. 4.3). These options are dichotomic, i.e. all combinations with enabled and disabled options are possible, resulting in $2^6 = 64$ result sets. The visualization with tables and diagrams would require large amounts of space and the comparison of the individual patterns of enabled options is obfuscated. Therefore a new technique for the visualization of high-dimensional dichotomic data is proposed. Squares with an edge length proportional to the values are arranged in a two-dimensional matrix as employed by the Karnaugh-Veitch diagram. This allows the clear visualization of all results of a certain performance indicator as well as easy comparison within all dimensions (i.e., options).

References

- Allen, P. J., Josephs, O., & Turner, R. (2000, August). A Method for Removing Imaging Artifact from Continuous EEG Recorded during Functional MRI. *NeuroImage*, 12(2), 230–239.
- Allen, P. J., Polizzi, G., Krakow, K., Fish, D. R., & Lemieux, L. (1998). Identification of EEG Events in the MR Scanner: The Problem of Pulse Artifact and a Method for Its Subtraction. *NeuroImage*, 8, 229–239.
- Babiloni, F., Mattia, D., Babiloni, C., Astolfi, L., Salinari, S., Basilisco, A., ... Cincotti, F. (2004, December). Multimodal integration of EEG, MEG and fMRI data for the solution of the neuroimage puzzle. *Magnetic Resonance Imaging*, 22, 1471–1476.
- Baillet, S., Riera, J. J., Marin, G., Mangin, J. F., Aubert, J., & Garnero, L. (2001, January). Evaluation of inverse methods and head models for EEG source localization using a human skull phantom. *Physics in Medicine and Biology*, 46, 77–96.
- Bauer, H. (1984). *Experimentelle Elektroenzephalographie: Registrierung und Analyse des Elektroenzephalogramms in der physiologischen Psychologie*. Bern: Huber.
- Bear, M. F., Connors, B. W., & Paradiso, M. A. (2007). *Neuroscience: Exploring the Brain* (3rd ed.). Baltimore, MD: Lippincott Williams & Wilkins.
- Berkes, S., Husar, P., Schellhorn, K., Goetze, A., Plagwith, K., & Henning, G. (2004, June). A new concept for DC-capable biosignal acquisition system. In *10th annual meeting of the organization for human brain mapping*. Budapest, Hungary.
- Berkes, S., Schellhorn, K., Schlegelmilch, F., Markert, S., & Husar, P. (2004, June). *A new System for Continuous Full Band EEG Recording during*

- fMRI* [Poster, 10th Annual Meeting of the Organization for Human Brain Mapping]. Budapest, Hungary.
- Blumenthal, T. D., Cuthbert, B. N., Filion, D. L., Hackley, S., Lipp, O. V., & Van Boxtel, A. (2005, January). Committee report: Guidelines for human startle eyeblink electromyographic studies. *Psychophysiology*, 42, 1–15.
- Borga, M. (2001). *Canonical Correlation - a Tutorial* [online Tutorial, retrieved 2010-07-26]. <http://www.imt.liu.se/~magnus/cca/tutorial/tutorial.pdf>, Department of Biomedical Engineering, Linköping University.
- Bregadze, N., & Lavric, A. (2006, October). ERP differences with vs. without concurrent fMRI. *International Journal of Psychophysiology*, 62, 54–59.
- Bénar, C., Aghakhani, Y., Wang, Y., Izenberg, A., Al-Asmi, A., Dubeau, F., & Gotman, J. (2003). Quality of EEG in simultaneous EEG-fMRI for epilepsy. *Clinical Neurophysiology*, 114(3), 569–580.
- Debener, S., Mullinger, K. J., Niazy, R. K., & Bowtell, R. W. (2008, March). Properties of the ballistocardiogram artefact as revealed by EEG recordings at 1.5, 3 and 7 T static magnetic field strength. *International Journal of Psychophysiology*, 67, 189–199.
- Delorme, A., & Makeig, S. (2004). EEGLAB: an open source toolbox for analysis of single-trial EEG dynamics including independent component analysis. *Journal of Neuroscience Methods*, 134, 9–21.
- Doblinger, G. (2001). *MATLAB-Programmierung in der digitalen Signalverarbeitung*. Weil der Stadt: J. Schlembach Fachverlag.
- Doblinger, G. (2004). *Signalprozessoren: Architekturen – Algorithmen – Anwendungen* (2., überarb. und aktualisierte Aufl. ed.). Wilburgstetten: J. Schlembach Fachverlag.
- Fridlund, A. J., & Cacioppo, J. T. (1986, September). Guidelines for Human Electromyographic Research. *Psychophysiology*, 23, 567–589.
- Glaser, J., Schöpf, V., Bauer, H., & Fischmeister, F. (2012). *FACET – a “Flexible artefact correction and evaluation toolbox” for EEG/fMRI data* [Poster at OHBM2012]. Beijing, China.
- Glover, I., & Grant, P. M. (2004). *Digital Communications* (2nd ed.). Harlow England New York: Pearson/Prentice Hall.
- Goldman, R. I., Stern, J. M., Engel, J., J., & Cohen, M. S. (2000, November). Acquiring simultaneous EEG and functional MRI. *Clinical Neurophysiology: Official Journal of the International Federation of Clinical Neurophysiology*, 111(11), 1974–1980.
- Hoffmann, A., Jäger, L., Werhahn, K. J., Jaschke, M., Noachtar, S., & Reiser, M. (2000, November). Electroencephalography during func-

- tional echo-planar imaging: detection of epileptic spikes using post-processing methods. *Magnetic Resonance in Medicine: Official Journal of the Society of Magnetic Resonance in Medicine / Society of Magnetic Resonance in Medicine*, 44(5), 791–798.
- Huettel, S. A., Song, A. W., & McCarthy, G. (2009). *Functional Magnetic Resonance Imaging* (2nd ed.). Houndmills: Palgrave Macmillan.
- Iannetti, G., Niazy, R., Wise, R., Jezzard, P., Brooks, J., Zambreau, L., . . . Tracey, I. (2005). Simultaneous recording of laser-evoked brain potentials and continuous, high-field functional magnetic resonance imaging in humans. *NeuroImage*, 28(3), 708 - 719.
- IEEE Task P754. (1985, August 12). ANSI/IEEE 754-1985, standard for binary floating-point arithmetic [Computer software manual].
- Kolin, A. (1952). Improved Apparatus and Technique for Electromagnetic Determination of Blood Flow. *Review of Scientific Instruments*, 23, 235.
- Lee, E. A., & Messerschmitt, D. G. (2000). *Digital Communication* (Second ed.). Boston: Kluwer Academic Publishers.
- Mandelkow, H., Brandeis, D., & Boesiger, P. (2010, February). Good practices in EEG-MRI: the utility of retrospective synchronization and PCA for the removal of MRI gradient artefacts. *NeuroImage*, 49(3), 2287–2303.
- Menon, V., & Crottaz-Herbette, S. (2005). Combined EEG and fMRI Studies of Human Brain Function. *International Review of Neurobiology*, 66, 291–321.
- Meriläinen, V. (2002, December). *Magnetic resonance imaging with simultaneous electroencephalography recoding: safety issues* [diploma thesis]. Helsinki University of Technology, Department of Electrical and Communications Engineering.
- Michel, C. M., Murray, M. M., Lantz, G., Gonzalez, S., Spinelli, L., & Grave de Peralta, R. (2004, October). EEG source imaging. *Clinical Neurophysiology*, 115, 2195–2222.
- Minati, L. (2006). Neuroimaging Techniques: a Conceptual Overview of Physical Principles, Contribution and History. In (Vol. 839, pp. 503–519). AIP.
- Moosmann, M., Schönfelder, V. H., Specht, K., Scheeringa, R., Nordby, H., & Hugdahl, K. (2009, May). Realignment parameter-informed artefact correction for simultaneous EEG-fMRI recordings. *NeuroImage*, 45(4), 1144–1150.
- Moser, E., Meyerspeer, M., Fischmeister, F. P. S., Grabner, G., Bauer, H., & Trattnig, S. (2010, June). Windows on the Human Body – in Vivo High-Field Magnetic Resonance Research and Applications in Medicine

- and Psychology. *Sensors*, 10, 5724–5757.
- Mulert, C., Jäger, L., Schmitt, R., Bussfeld, P., Pogarell, O., Möller, H., . . . Hegerl, U. (2004, May). Integration of fMRI and simultaneous EEG: towards a comprehensive understanding of localization and time-course of brain activity in target detection. *NeuroImage*, 22, 83–94.
- Mühlenweg, M., Schaefers, G., & Tratznig, S. (2007, December). Sicherheitsaspekte in der Hochfeld-Magnetresonanztomographie. *Der Radiologe*, 48, 258–267.
- neuroConn *NEURO PRAX MR* (Brochure). (2009, December). Grenzhammer 10, 98693 Ilmenau, Germany: neuroConn GmbH.
- Niazy, R. K., Beckmann, C., Iannetti, G., Brady, J., & Smith, S. (2005). Removal of FMRI environment artifacts from EEG data using optimal basis sets. *NeuroImage*, 28(3), 720 - 737.
- Nöth, U., Laufs, H., Stoermer, R., & Deichmann, R. (2011). Simultaneous electroencephalography-functional MRI at 3 T: An analysis of safety risks imposed by performing anatomical reference scans with the EEG equipment in place. *Journal of Magnetic Resonance Imaging*, n/a–n/a.
- Ogawa, S., Lee, T. M., Kay, A. R., & Tank, D. W. (1990, December). Brain magnetic resonance imaging with contrast dependent on blood oxygenation. *Proceedings of the National Academy of Sciences of the United States of America*, 87(24), 9868–9872.
- Ogawa, S., Menon, R. S., Tank, D. W., Kim, S., Merkle, H., Ellermann, J. M., & Ugurbil, K. (1993). Functional brain mapping by blood oxygenation level-dependent contrast magnetic resonance imaging. a comparison of signal characteristics with a biophysical model. *Biophysical Journal*, 64, 803–812.
- Oppenheim, A. V., Willsky, A. S., & Nawab, S. H. (1997). *Signals & Systems* (2nd ed.). Upper Saddle River New Jersey: Prentice-Hall International, Inc.
- Pascual-Marqui, R. D. (1999). Review of Methods for Solving the EEG Inverse Problem. *International Journal of Bioelectromagnetism*, 1(1), 75–86.
- Pascual-Marqui, R. D., Michel, C. M., & Lehmann, D. (1994, October). Low resolution electromagnetic tomography: a new method for localizing electrical activity in the brain. *International Journal of Psychophysiology: Official Journal of the International Organization of Psychophysiology*, 18(1), 49–65.
- Precht, A. (2006). *Vorlesungen über die Grundlagen der Elektrotechnik* (2nd ed., Vol. 1). Wien: Springer.
- Precht, A. (2008). *Vorlesungen über die Grundlagen der Elektrotechnik* (2nd ed., Vol. 2). Wien: Springer.

- Quiroga, R. Q., & Garcia, H. (2003). Single-trial event-related potentials with wavelet denoising. *Clinical Neurophysiology*(114), 376–390.
- Rappaport, T. S. (2001). *Wireless Communications: Principles and Practice*. Upper Saddle River, N.J.; London: Prentice Hall PTR.
- Ritter, P., Becker, R., Graefe, C., & Villringer, A. (2007, July). Evaluating gradient artifact correction of EEG data acquired simultaneously with fMRI. *Magnetic Resonance Imaging*, 25(6), 923–932.
- Ritter, P., & Villringer, A. (2006, January). Simultaneous EEG–fMRI. *Neuroscience & Biobehavioral Reviews*, 30(6), 823–838.
- Rosenkranz, K., & Lemieux, L. (2010, January). Present and future of simultaneous EEG–fMRI. *Magnetic Resonance Materials in Physics, Biology and Medicine*, 23(5-6), 309–316.
- Schlegelmilch, F., Schellhorn, K., & Markert, S. (2004, June). *A Model for On-line Correction of DC-EEG Measurements during fMRI* [Poster, 10th Annual Meeting of the Organization for Human Brain Mapping]. Budapest, Hungary.
- Sijbers, J., Michiels, I., Verhoye, M., Van Audekerke, J., Van der Linden, A., & Van Dyck, D. (1999). Restoration of MR induced artifacts in simultaneously recorded MR/EEG data. *Magnetic Resonance Imaging*, 17(9), 1383–1391.
- Sommerville, I. (2004). *Software Engineering* (7th ed.). Boston: Addison Wesley.
- van der Meer, J., Tijssen, M., Bour, L., van Rootselaar, A., & Nederveen, A. (2010, May). Robust EMG–fMRI artifact reduction for motion (FARM). *Clinical Neurophysiology*, 121(5), 766–776.
- Weinrichter, H., & Hlawatsch, F. (1991). *Stochastische Grundlagen Nachrichtentechnischer Signale*. Wien; New York: Springer-Verlag.
- Weishaupt, D., Köchli, V. D., & Marincek, B. (2003). *Wie funktioniert MRI? Eine Einführung in Physik und Funktionsweise der Magnetresonanzbildgebung* (4. Aufl. ed.). Berlin, Heidelberg, New York: Springer.
- Widrow, B., Glover, J. J., McCool, J., Kaunitz, J., Williams, C., Hearn, R., ... Goodlin, R. (1975, December). Adaptive noise cancelling: Principles and applications. *Proceedings of the IEEE*, 63(12), 1692–1716.
- Yan, W. X., Mullinger, K. J., Brookes, M. J., & Bowtell, R. (2009, June). Understanding gradient artefacts in simultaneous EEG/fMRI. *NeuroImage*, 46(2), 459–471.

Abstract

The concurrent acquisition of EEG and fMRI is in use since the late 1990ies. This method of multi-modal imaging allows to combine the high spatial resolution of fMRI and the high temporal resolution of EEG. The inverse problem for source localization of EEG signals is assisted by the data acquired with fMRI.

However, both methods generate mutual artifacts of which the fMRI gradient artifact in the EEG signal has the largest impact. The rapidly changing magnetic fields of the fMRI gradient system induce voltages in the EEG leads which are several orders of magnitude above the EEG signal itself.

To tackle the problem of artifacts in the EEG signal, several algorithms were published. Most of these correction algorithms utilize the high periodicity of the artifacts and calculate an averaged artifact template which is subtracted from the recorded signal. However, movement of the subject results in additionally induced voltages as well as a change in the artifact signal shape which cannot be handled satisfactorily by the existing algorithms. This problem is even more prevalent in EMG signals, which recently were added as a third modality, to cover movement and strain of facial and other muscles.

In this diploma thesis existing algorithms are compared and a new universal toolbox “FACET — A Flexible Artifact Correction and Evaluation Toolbox” is developed. It provides facilities for the analysis of the EEG/EMG data and fMRI gradient artifacts, for the correction of these artifacts and for the evaluation of the correction results. This unique combination of all three features allows to iteratively optimize the configuration of the algorithm specifically

to the data. The toolbox is extensible at any point and provides multiple improvements over existing algorithms.

The toolbox is used to implement a prototypical algorithm “EEGfMRI” as a best-practice example. Its correction results are evaluated with two datasets using the integrated evaluation framework. It could be shown that the proposed algorithm delivers superior correction results compared to the existing algorithms especially for EMG signals with inherent movement of the subject.

The toolbox was presented at the OHBM 2012 as [Glaser et al. \(2012\)](#) with the title “FACET – a “Flexible Artefact Correction and Evaluation Toolbox” for EEG/fMRI data”. It will be available online at <http://scan.psy.univie.ac.at/> as open source software under the terms of the GNU General Public License.

Zusammenfassung

Die gleichzeitige Aufzeichnung von EEG und fMRI wird seit den späten 1990ern angewendet. Dieses Verfahren des sog. “Multi-Modal Imaging” gestattet die Kombination der hohen räumlichen Auflösung von fMRI und der hohen zeitlichen Auflösung des EEG. Das inverse Problem bei der Quellenlokalisation von EEG-Signalen wird von den fMRI Daten unterstützt.

Allerdings verursachen beide Methoden gegenseitige Artefakte, von denen die fMRI Gradientenartefakte im EEG-Signal die größte Störung verursachen. Die schnell veränderlichen magnetischen Felder des fMRI Gradientensystems induzieren Spannungen in den EEG-Leitungen, die um mehrere Größenordnungen über dem eigentlichen EEG-Signal liegen.

Um diese Artefakte zu entfernen wurden mehrere Algorithmen publiziert. Die meisten dieser Korrekturalgorithmen nutzen die Periodizität des Artefaktsignals aus und berechnen eine gemittelte Vorlage, die vom aufgezeichneten Signal subtrahiert wird. Allerdings entstehen durch die Bewegungen des Probanden zusätzliche induzierte Spannungen und die Form des Artefaktsignals ändert sich. Diese Störungen können von den existierenden Korrekturalgorithmen nicht zufriedenstellend behandelt werden. Noch problematischer ist dieser Umstand bei der Aufzeichnung von EMG Signalen, die seit einiger Zeit als dritte Modalität zur Erfassung der Bewegungen und Anspannung von Muskeln im Gesicht und den Extremitäten verwendet wird.

In dieser Diplomarbeit werden existierende Korrekturalgorithmen verglichen und eine neue universelle Toolbox “FACET — A Flexible Artifact Correction and Evaluation Toolbox” entwickelt. Sie stellt Methoden zur Analyse der EEG Daten und der fMRI Gradientenartefakte, zur Korrektur dieser Ar-

tefakte sowie zur Evaluierung der Korrekturergebnisse zur Verfügung. Diese spezielle Kombination von allen drei Funktionen erlaubt die iterative Optimierung der Konfiguration des Algorithmus speziell für die vorhandenen Daten. Die Toolbox ist an allen Stellen erweiterbar und bietet mehrere Verbesserungen gegenüber existierenden Algorithmen.

Die Toolbox wird zur Implementierung des prototypischen “EEGfMRI”-Algorithmus als Best-Practice Beispiel verwendet. Die Korrekturergebnisse werden mit zwei Datensätzen unter dem Einsatz des integrierten Evaluations-Frameworks evaluiert. Es konnte gezeigt werden, dass der vorgeschlagene Algorithmus deutlich bessere Ergebnisse als existierende Algorithmen liefert, insbesondere für EMG Signale mit inhärenten Bewegungen des Probanden.

Die Toolbox wurde auf der Konferenz OHBM 2012 als [Glaser et al. \(2012\)](#) mit dem Titel “FACET – a “Flexible Artefact Correction and Evaluation Toolbox” for EEG/fMRI data” präsentiert. Sie wird auf <http://scan.psy.univie.ac.at/> online als Open-Source-Software unter den Bedingungen der GNU General Public License zur Verfügung gestellt.

Curriculum Vitae

Name: Johann Glaser

Date of birth: June 1, 1979

Nationality: Austria

Address: Hagenmüllergasse 27–33
1030 Wien

Education: 1998: School leaving graduation with distinction,
HTBLA Linz Paul-Hahn-Straße, Electrical En-
gineering

1998–2004: Electrical Engineering, masters degree with
distinction, Vienna University of Technology

2004–present: PhD in Electrical Engineering, Vienna Uni-
versity of Technology

2004–present: Psychology, University of Vienna

Employment: 2005–present: Project assistant at the Institute of Computer
Technology, Vienna University of Technology

Lebenslauf

Name: Johann Glaser

Geburtsdatum: 1. Juni 1979

Staatsbürgerschaft: Österreich

Adresse: Hagenmüllergasse 27–33
1030 Wien

Ausbildung:

- 1998: Matura mit Auszeichnung, HTBLA Linz
Paul-Hahn-Straße, Elektrotechnik
- 1998–2004: Studium Elektrotechnik, Technische Universität Wien, Abschluss mit Auszeichnung
- seit 2004: Doktoratsstudium Elektrotechnik
- seit 2004: Studium Psychologie, Universität Wien

Beschäftigung:

- seit 2005: Projektassistent am Institut für Computertechnik, TU Wien

